Aggregation- and Photophysics of Merocyanine Dyes for Photovoltaic Applications

Dissertation

zur Erlangung des akademischen Grades d*octor rerum naturalium*
(Dr. rer. Nat.)

Vorgelegt dem Rat der Chemisch-Geowissenschaftlichen Fakultät der Friedrich-Schiller-Universität Jena von

Diplom Ingenieur Felix Herrmann-Westendorf

Geboren am 27.07.1985 in Meiningen

Gutachter:

1. Prof. Dr. Benjamin Dietzek

2. Prof. Dr. Volker Deckert

3.

Tag der Verteidigung: 05.07.2019

List of Figures

List of Tables

1 Introduction

After the discovery of semiconducting organic materials[1, 2] and new classes of synthetic organic dyes these materials have made progress towards an extensive commercial use in opto-electronic devices like organic light emitting diodes[3], organic solar cells[4-8] and dye sensitized solar cells[9, 10]. The aim of using molecules rather than standard inorganic semiconductors arises from several market-driven advantages: The first one is the very low cost and low power consumption of producing organic materials.[11, 12] Furthermore, thin organic films have new possibilities in producing flexible products like OLED displays and organic solar cells.[12, 13] Also the possibility of upscaling to mass production using *e.g.* roll to roll techniques, having a huge throughput and giving low prices per unit, is given.[12]At the end, enabled by the enormous toolbox of organic synthesis,[14] a huge number of different organic molecules and especially dyes were synthesized for every possible use in organic opto-electronic devices.[15, 16]

Within the field of possible applications the focus of this work is set on materials used for organic photovoltaics and dye sensitized solar cells. Most of the sun's light is distributed over the red to near infrared (NIR) spectral region.[17] Hence, one main focus for the development of new materials is the expansion of the absorption to the red and NIR.[15, 18, 19] This is usually done by creating molecules with an intramolecular charge transfer state, which can be populated by absorbing low energy photons. This can either be achieved using noble-metal complexes[15] having a metal to ligand charge transfer state[20, 21] or by implementing electron donor and electron acceptor units in fully organic dyes. This leads to an intramolecular charge transfer state, which is usually red shifted in comparison to $\pi \rightarrow \pi^*$ transitions[22]. All organic dyes share the advantage that no rare material like ruthenium or iridium are needed and that the molecular design options of new dyes are nearly unlimited by using the framework of organic synthesis.[15] Most of the fully organic dyes follow the basic design principle of donor-π-bridge-acceptor or donor-(weak)acceptor-π-bridge-acceptor.[19]

The LUMO of most of the dyes or donor-molecules is localized on the acceptor or electron pulling part of the molecule. Hence there is a need to bring this part of the molecule close to the accepting metal oxide to optimize the charge separation process.[23] For DSSC dyes the electron pulling and anchoring group determines the efficiency of the charge extraction process. Most of the dyes are anchored using an carboxylic acid or thiocyanate moiety for the attachment to the electron accepting oxide.[15] The most common combination of the anchoring part of the molecule with a suitable electron pulling moiety in metal free organic sensitizers is the α cyano carboxylic acid or cyanoacrylic acid group.[15, 19] The electron pushing moiety might be made of coumarine, indoline or tri-phenylamin units.[15, 24] The tri-phenylamine group is one of the most commonly used ones yielding high power conversion efficiencies above 8% and good photo-chemical stability.[15, 19, 24] The π-bridge typically consist of different moieties like thiophene or phenylenerings in different combination. As weak acceptor *e.g.* thiazoles can be used.[19] The length of the π-bridge is one major factor determining the efficiency of charge separation and recombination.[25]

In most applications of organic dyes, like organic light emitting diodes (OLEDs)[3], and dye sensitized solar cells (DSSCs) [82], molecules in solid state thin films or densely packed on the TiO_2 surface, are used. Hence, the local morphology, aggregation, or, in other words, the different intermolecular arrangements formed in the solid state are one of the main factors determining efficiency of the device.[19, 26, 27] In the example case of dye sensitized solar cells, aggregation can be very beneficial for a few dyes,[28, 29] but for many dyes the formation of aggregates can strongly reduce the power conversion efficiency.[30, 31]

In most of the studies the structure of the given aggregates or dimers is not under investigation. The try and error method using different dyes and additives to optimize efficiency is, from an application point of view, where the given efficiency and stability are the most important parameters, a feasible option. But from a scientific point of view and to enable systematic improvement of device performance, the knowledge of aggregate structure-function relation is a more interesting and constructive way to achieve improvements. However, because determination of the supramolecular structure within working devices is challenging, only few reports on supramolecular control of optoelectronic device function exists. In the field of DSSCs dyes some theory papers exist, which aim to predict the aggregate structure on a TiO_2 surface and their influence on the electronic structure and photophysics. Here Pastore *et al.*[32] used a dimer of two different indoline dyes. These where placed on a TiO_2 surface and optimized in their geometry. Afterwards the absorption spectra and charge differences density were calculated for the dimer, while the TiO_2 surface was removed. With this model they claimed for the given molecules that the aggregation leads to a situation, where the intermolecular charge transfer is competing with the charge injection to the TiO_2 electrode. The aggregation of DSSC dyes validated with experimental data is very much underrepresented in the literature. One example is the work on merocyanines from Nüesch *et al.* where they found H-aggregation for a merocyanine dyes in solution and on colloids made of TiO_2 and Al_2O_3.[33] Using the same material also J-aggregation could be observed on Al_2O_3.[34] Within the found literature, where aggregation in DSSCs is discussed, the main focus was set on the prevention of aggregation with co-adsorbents[35-38] or sterically demanding side groups[19, 39-43]. For non-DSSC dyes the published work about aggregation and their effect on opto-electronical properties is much more evolved. Here Frank Würthner *et al.*[44] has published a nice review about J-aggregates made of different dyes, *e.g.* amphiphilic cyanine dyes, porphyrins, giving a nice overview about structure and optical properties. Therefore in this work the focus is set to the less investigated understanding of how aggregates of especially DSSC dyes may be arranged and how this influences their optical and electronical properties.

The already established models to explain the effects of aggregation on the electro-optical properties of the aggregated dipolar molecules were first observed independently by Scheibe *et al.*[45] and Jelley *et al.*[46] Here new absorption bands and later emission bands in the visible spectral range could be observed. The Jelly or simply J-aggregate shows a narrow red-shifted absorption band, while the hypsochromic or H-aggregate shows a blue-shifted broad absorption peak with a complicated vibrational structure.[47]

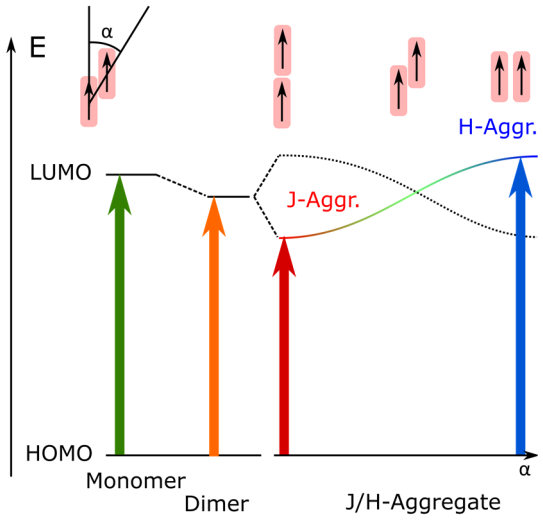

Figure 1 Simplified overview of the Energy levels in monomers, dimers and H- and J-aggregates drawn like in Würthner *et al.*[44] The LUMO of the H and J aggregates is plotted over the angle of the transition dipole moments (α) between two adjacent single molecules. The definition of α is illustrated in the top left corner. The straight line resembles final state of the allowed optical transition, while the dotted line resembles the final state of the forbidden one. Here the range of α were the J-aggregate is the allowed transition is colored in red, while the range of α for H-aggregates is colored in blue.

The origin of both bands is the splitting of the lowest unoccupied molecular orbital (LUMO) into a lower and higher lying LUMO at the transition between monomer and dimer[48] (See Figure 1). These split molecular orbitals corresponds to the new S_1 and S_2 states. This is caused by the overlap of the LUMOs of the respective single molecule. Whether H- or J-aggregates can be observed depends on the intermolecular arrangement. If the transition dipole moments of the monomers forming the aggregate are aligned parallel, the transition from the ground state to the energetically lower lying S_1 is forbidden. Hence, the first bright transition happens from the S_0 to the S_2 and is thus blue-shifted for an H-aggregate, as compared to the monomer. If the transition dipole moments are in-line, the transition from the S_0 to the S_1 becomes bright and hence a red shifted absorption is observed, which is the J-aggregate feature.[44] Despite the arising of new absorption bands the photo-physics in the aggregates are drastically changing. A first hint towards this can be found for the emission of the respective aggregates. While J-aggregates usually show a very narrow and bright emission with a very small Stokes shift,[44, 49] H-aggregates are typically non-emissive[44]. Only in very few cases broad red shifted emission could be observed.[44, 50] The driving forces for the creation of dimeric structures are mainly dipole-dipole interactions[51], van der Waals forces,[52] hydrogen bonds[53] or hydrophilic and hydrophobic interactions.[53] The formation of different aggregates is always determined by the structure of the given molecule. This means that *e.g.* different very flat molecules usually tend to build aggregates in solution due to ππ-stacking or dipol-dipol interaction. As example the molecule class of cyanine dyes, squarines, porphyrines or perylenes can efficiently form aggregates, depending on the functionalization, that was applied to facilitate the formation of aggregates. [44] A more detailed overview on the driving forces of aggregation and dimers formation can be found in the Appendix.

Despite the changes in absorption and emission, aggregation can have a huge impact on the electronic properties of a solid film.[54] The electronic coupling between adjacent molecules can be enhanced, facilitating charge separation between adjacent molecules over charge transfer to the electron accepting TiO_2. [32] Also more states within the band gap between S_0 and S_1 can be created. This might be caused due to fluctuations in the molecular orbital energies due to disorder, as known for amorphous semiconductors, leading to tail states.[55] Also localized states within the gap can be created, which are usually effective recombination sites, as it is well known for amorphous semiconductors.[56, 57]

Hence, the effect of aggregation on the electro optical parameters of thin films made of organic dyes has to be understood in detail, to further improve devices made of this kind of thin film. Furthermore, photoactive molecules like DSSC dyes can show photo aggregation[58] or photo dimerization[59], when they are placed in close proximity and illuminated with light. The dimerization might be a photo-driven non-covalent aggregation or the formation of photo-dimers by means of the formation of new covalent bonds. The published knowledge about photo-aggregation and -dimerization, especially for dyes used in dye sensitized solar cells, has to be improved, since I could not find any relevant publication addressing these topics *via* numerous literature searches using *e.g.* the web of knowledge and the cited papers within several papers addressing aggregation of dyes. Also the aggregation of DSSC relevant dyes already in solution was not found to be investigated in detail. Hence, these topics will be addressed in the present work. Also the effect of different morphology on the recombination kinetics after photo-excitation will be investigated. This will be done to understand, how different supra molecular structures create recombination sites or stable intermolecular excited states. For all these questions firstly thin films with a tunable morphology have to be created to differentiate between single molecule processes and processes in different aggregated thin films.

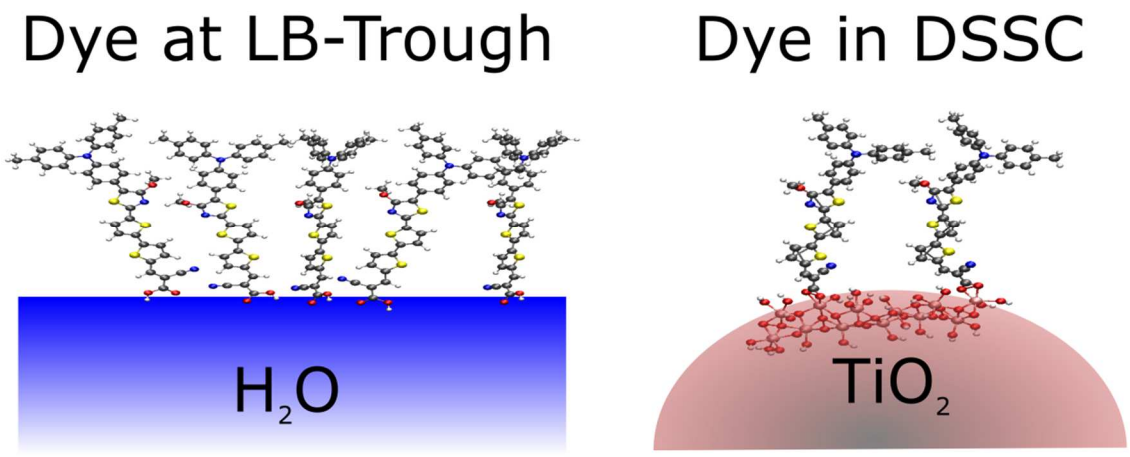

Figure 2 Alignment of DSSC dyes on the water surface of an LB trough in comparison with a possible alignment on the TiO_2 surface of a DSSC. Here one of the molecules investigated in this thesis was used as model dye.

This can be done using the Langmuir-Blodgett-technique.[60] This technique uses the amphiphilicity of molecules to align them at the air water interface, as shown in the left part of

Figure 2.[61, 62] After the molecules have aligned themselves on the water surface, a compression is started to force the molecules into different aggregate orientations. In general the more pressure is put on the molecules, the more crystalline the obtained films will get.[63] To determine crystallinity or surface coverage on the water surface the surface pressure is used as a measure. The surface pressure at the transfer process from the water surface to the solid state sample is kept constant and determines the thin film morphology. Using the Langmuir-Blodgett-technique enables us to control aggregation within every single monolayer, also the layer stack thickness and the layered sequence.[60, 63] Within this method the aim is to build samples with a tunable morphology to further investigate the effects of morphology on the electronic structure and optical features on thin solid films. Previous works using the Langmuir-Blodgett–technique to produce thin solid films have shown the capabilities of the LB-technique to produce samples with a defined and tunable aggregate structure and their impact on the optical and electronical properties.[64-66] Different dyes like the amphiphilic coumarines were used to create thin films with a tunable degree of J-aggregation.[67] As shown by Hamanaka *et al.*[68] J-aggregates made of merocyanine dyes in arachidic acid matrices could be prepared by spin coating and the Langmuir-Blodgett-technique. Within this study it was found that the use of the Langmuir-Blodgett-technique was successful in preparing large J-aggregates, especially in comparison with the much smaller aggregates found for spin coated samples. Also the formation of J-aggregates by using UV-light as post processing was demonstrated using merocyanine dyes.[69, 70]

In the present work dipolar merocyanines, which vary in the length and chemical nature of their π-bridge between donor and acceptor moieties, to tune the balance between charge transfer and π-π* characters of the S_0 to S_1 electronic transition, are used. Thus, supramolecular structure formation will be varied by both, the weight of dipole-dipole interaction on the total intermolecular interactions as well as the molecular shape, which changes with increasing π-bridge length. These merocyanine dyes consist of tri-penylamine moiety as electron pushing unit. As electron pulling group the common cyanoacrylic acid is used.[15] The π-bridge consists of thiophene units and 4-hydroxy thiazole units.[71] Despite the change in internal charge transfer a prolonged π-bridge can also promote aggregation or dimerization via π- π stacking. Furthermore the amphiphilisity, which is inherent for almost every organic dye sensitized solar cell dye,[23] is suggesting the use of water air interfaces to align the molecules properly.

With the possibility to produce defined and amorphous morphologies we could derive the effects of different aggregation on the optical parameters. To get a deeper understanding on the effects of aggregation, also the kinetics after photoexcitation have to be investigated. In this manner the first step is the measurement of emission spectra and fluorescence quantum yields. To understand the processes right after photoexcitation transient absorption measurements in the femto to nanosecond time regime are applied. This was fairly often demonstrated for solutions and relatively thick solid state films.[72] But also for the much more challenging thin Langmuir-Blodgett-films some experimental results are reported in the literature.[73] Hence, the transient absorption measurements can be applied to optically thin solid films, but not in a straight forward manner. Additionally, aggregation will be controlled due to incorporation of the dyes into solid matrices. We investigate the supramolecular structures formed by means of UV-vis absorption and fluorescence spectroscopy, dynamic light scattering techniques, atomic force microscopy and quantum chemical calculations. As photoreactions and photo-aggregation might

appear, this has to be investigated in detail. This will be done using illumination dependent UV-vis absorption and dynamic light scattering measurements.

2 Materials and Experimental Methods

2.1 Materials

Dyes

The dyes used in this work contain a α-cyano carboxylic acid groups as electron acceptors (A) and tri-arylamine groups as donors (D)[74] as shown in Figure 3. If we consider one of these aryl groups as first part of the π-bridge between D and A substance **D2A** might be viewed as containing a bridge consisting of two thiophene rings. The π-bridges of **D3A** and **D4A** are successively extended by one more aromatic ring. However, **D3A** is distinctly different from **D2A** since the thiophene of the triaryl moiety is replaced by a 4-methoxy-5-phenylene-thiazole moiety.[71] Finally, **D4A** combines both motives, the 4-methoxy-5-phenylene-thiazole and the bithiophene moieties, in its bridge.[71] The used molecules **D3A** and **D4A** where obtained from the Beckert group and synthesized according to literature.[71] **D2A** was synthesized by the group of Professor Würthner from the University of Würzburg.

Additives, matrix materials and solvents

Desoxicholic acid (DOA), poly(methyl methacrylate) (PMMA), toluene sulfonic acid (TSA) and Tetramethylguanidine (TMG) were obtained from Sigma Aldrich and used as received. All solvents are of HPLC or spectroscopic grade, which is highly recommended for fluorescence measurements[75] and Langmuir-Blodgett film formation.[63]

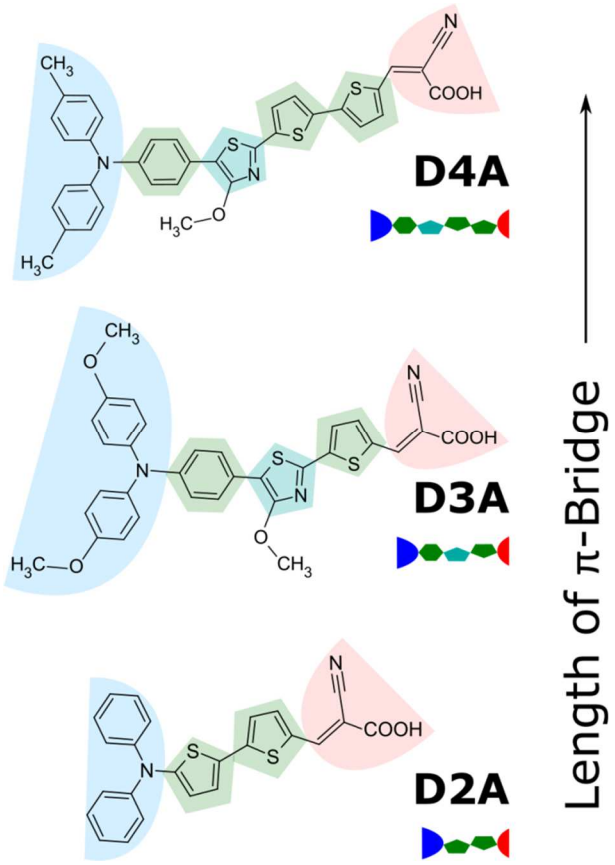

Figure 3: Lewis structures of the merocyanines **D2A**, **D3A**, **D4A**. The red shaded area represents the electron acceptin moiety, the green parts are the electron bridge and the blue shaded areas are the electron donating moieties.

2.2 Thin film preparation

Drop casting and spin coating

Thin films were prepared using three different methods to obtain films with quite different morphologies. The simplest way to create thin films is drop casting (DC) were solutions of the molecule were simply dropped on the cleaned substrate. As the solvent slowly evaporates a thin inhomogeneous film will be formed on the substrate. More homogeneous films could be produced using spin coating (SC). Here a solution is dropped on the substrate and afterwards the substrate is rotated at high rotation frequencies. The rotation speeds usually vary between 600 and 6000 rounds per minute (rpm).[76] To get smooth films with a homogeneous film thickness, it is necessary to spread the solution all over the substrate before starting the rotation. Furthermore, one should take care to have a solution with high concentration and without any particles. As solvent one should choose one that dissolves the molecule in high concentrations. Usually the concentration should reach approximately 10 to 20 mg/ml.[76] Furthermore, to the solvent shall evaporate relatively slow and should wet the whole surface of the substrate. The later can be achieved by using a proper surface treatment and cleaning. For obtaining a hydrophilic surface, we usually clean the samples 3x15 minutes within an ultrasonic bath in acetone and subsequently 3x15 minutes in isopropylic alcohol. After this treatment the substrates has to be stored in isopropylic alcohol for at least 12 hours. As solvent, usually

toluene or chlorobenzene are used to produce good SC films. M-xylene is another alternative known from the use in casting organic solar cells[77]. Those two preparation methods will usually give relatively disordered films with a low crystallinity.[27] The crystallinity of the thin films prepared by SC can be adjusted using additives[78] or post-processing like annealing. [27]

Langmuir-Blodgett technique

To get control over the aggregation and hence morphology of thin films the Langmuir-Blodgett (LB) technique can be used. The basic concept is the self-assembly of monomolecular layers of amphiphilic molecules on a water surface. This basic concept was developed in the early 20th century by Irvine Langmuir,[61] who was able to transfer one single monolayer to a solid substrate. The transfer of several monolayers to solid substrates was then developed by Katharina Blodgett[79, 80] in the 1930s. When the impact of molecular structure ordering for optoelectronics[81-83] and molecular electronics was recognized, the LB-technique gained increased interest in the field of academic research beginning in the middle of 1980s.[63] Especially, materials for non-linear optics were in the focus of research.[84-86] Despite some drawbacks regarding reproducibility and scalability, the Langmuir-Blodgett technique is still an elegant and useful method to design well defined layered structures with monolayer precission.[60, 63] But some of these drawbacks can be overcome using *e.g.* roll to roll LB-devices[65, 87] and sufficient experimental experience. By using the LB-technique we gain a distinct control over morphology/crystallinity of each monolayer.

The basic principle of the LB-technique can be described in the following way. The LB-trough itself is usually a Teflon trough, which is filled with ultraclean water. The surface area of the water can be adjusted and reduced using one or two sliding barriers, which are usually also made of Teflon. Teflon is used to improve the clean-ability of the LB-trough.[63] The molecules or particles used are spread on the water surface by using a low concentrated solution in a solvent, which is not miscible in water. In our case, we used chloroform or toluene. The used molecules should be amphiphilic, meaning that they possess a hydrophilic part, which anchors the molecule in the water sub-phase and a hydrophobic part, which avoids the dissolution in water. The hydrophobic part is needed to prevent the molecules from dissolving in the water. Hence the hydrophobic part is mandatory for the use of a material on the LB-trough, while the hydrophilic part gives advances in the anchoring. This anchoring can facilitate a more controllable and reproducible orientation of the molecules at the air water interface. Polymeric materials used for the LB-technique usually have no anchoring groups, therefore polymeric Langmuir-films tend to build clusters on the water surface rather than flat monolayers.[88-90]

After the solution was spread and the solvent has evaporated, which usually takes only some seconds to some minutes, the molecules are very dilute on the water surface, as shown in the left part of Figure 5. This state is in analogy to the phase of matter called a two-dimensional gas phase. Here the molecules are separated from each other and do not interact notably. The interaction or packing of the molecules on the water surface is determined measuring the surface pressure. The surface pressure Π is defined as the difference between the surface tension of a clean water surface σ_0 and the measured surface tension of the Langmuir film on the water surface (σ).

$$\Pi = \sigma_0 - \sigma \tag{1.1}$$

The surface tension of a clean water surface σ_0 was determined to be 72mN/m at 25°C.[63]

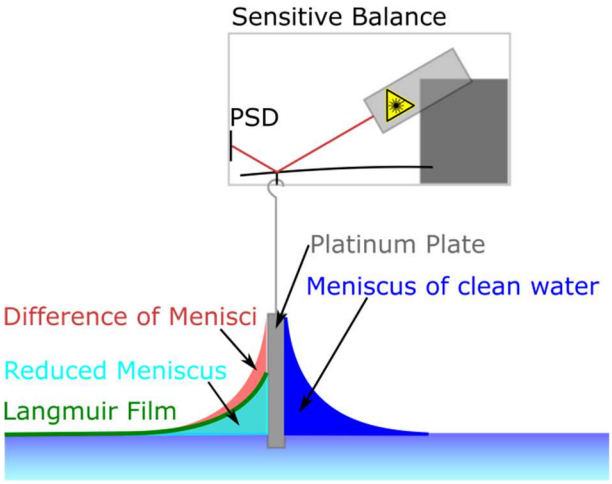

Figure 4 Schematic picture of a Wilhelmy balance. The sensitive balance consists of a long spring, where the platinum plate is attached to and a laser deflection measurement unit (Laser + PSD). The meniscus of a pristine water surface is drawn in dark blue, while the meniscus reduced by the Langmuir film (green) is drawn in light blue. The difference in the menisci is drawn in red.

The surface pressure is measured using a Wilhelmy balance.[91, 92] The working principle of the balance is shown in Figure 4. These devices consist of a highly sensitive balance and a platinum plate. The highly sensitive balance is made of a long linear spring, where the platinum plate is attached to. This spring bends by the weight of the platinum plate and the water meniscus. The bending is than measured using a laser deflection measurement unit. The deflection measurement is done by focusing a laser onto the spring and detecting the position of the reflected beam by a position sensitive device (PSD). With this balance the weight difference of the meniscus on the platinum plate, which is placed at the air water surface, is determined. Since the contact angle of the water at the meniscus is reduced by the molecules on the water surface, also the weight measured by the Wilhelmy balance is reduced.

The behavior of a Langmuir film on the water surface is usually shown in an isothermal curve, where the surface pressure is plotted on the y-axis and the available area per molecule is plotted on the x-axis. The basic processes are shown in Figure 5. By starting the compression cycle the available area for the molecules is successively reduced by the sliding barriers. At a certain point the surface pressure starts to rise. This point is denoted as the phase transition to the two-dimensional liquid phase. This means that the molecules are still separated, but start to interact with each other due to the higher surface density at the water air interface.

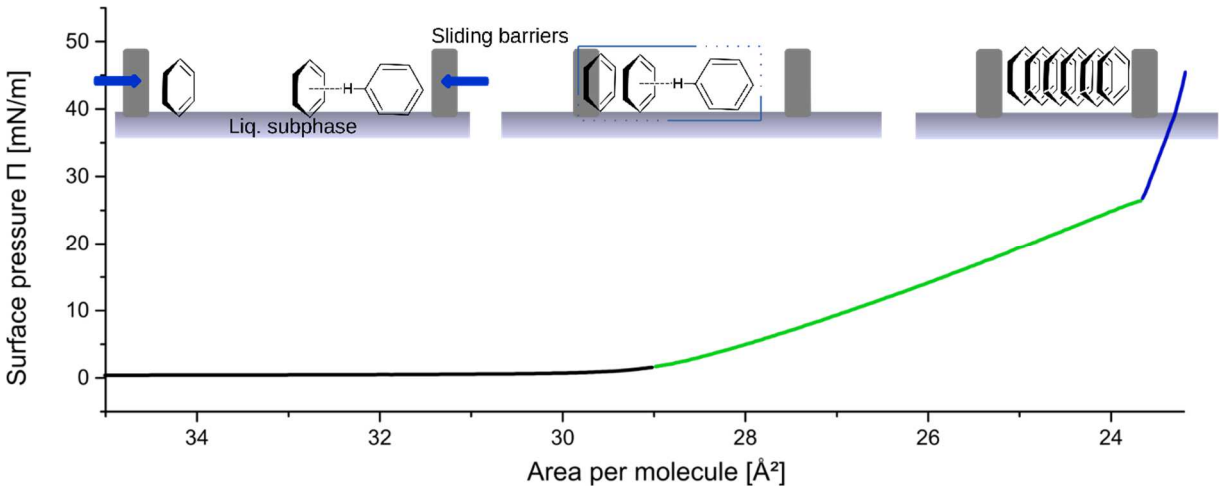

Figure 5 Langmuir film formation on a water surface. The isothermal curve is plotted exemplary to illustrate the basic processes determined. The black part of the isotherm represents the gas phase, the green one the liquid phase and the blue one the solid phase.

By further compression the surface pressure will steeply rise. Here the molecules reach the first solid state phase. In this phase the molecules build crystalline structures to minimize the needed area per molecule. Hence, crystalline structures are forced to be built. With a further compression, the molecules tend either to align in a bilayer system or create a different solid phase with lower requirement of area per molecule. To transfer thin films on solid substrates the molecules are compressed on the trough to a defined surface pressure, which is then hold constant by a control circle between the Wilhelmy balance and the sliding barriers. The transfer of the films is then done by dipping the substrate through the water surface. By using the KSV-Nima alternate LB-trough with three separated compartments, where one is a blank water surface and the other two are independently controllable Langmuir troughs, it is possible to do the dipping in different ways. As shown in Figure 6 different molecules have different transfer modes of the Langmuir-film to the substrate. Depending on the surface of the substrate being hydrophilic or hydrophobic and the adhesion of the used molecule one could get either X-, Y- or Z-type transfer as illustrated in Figure 6.

Using our KSV-Nima Alternate LB-trough with two different compartments, it is also possible to produce samples with layer stacks of different materials or with different crystallinity in a single dipping run. To get significant optical absorption from the prepared samples, the transfer was done ten times for each sample. This means that we have five up and five down strokes to transfer the Langmuir film onto the substrate. Since in case of the molecules used in this thesis only the upstroke gives reasonable good transfer ratios, the samples should have a thickness of approx. five monolayers.

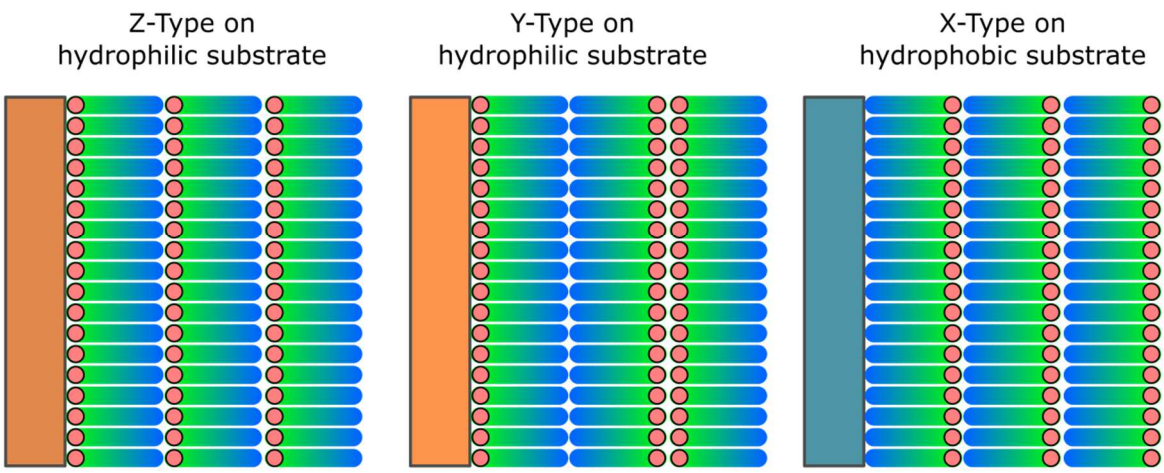

Figure 6 Transfer modes of Langmuir-Blodgett films. The orange squares represent the hydrophilic substrates, while the green one represents the hydrophobic one. The schematically drawn molecules have a red hydrophilic group and a green to blue hydrophobic chromophore. The colors have been chosen to maintain a constant colorcode for the here used molecules.

2.3 Spectroscopy

UV-vis Transmission

Transmission spectroscopy is used to determine the optical properties of molecules in solution and in thin films. In most cases the extinction or absorbance is determined in solution. From this value one can calculate the extinction coefficient using the Lambert-Beers law

$$E = c \cdot d \cdot \varepsilon \tag{1.2}$$

with the extinction E, the concentration c in mol/L, the path length of the cuvette d in cm and the extinction coefficient ε in L/(mol cm). The extinction itself is measured using the reduction of transmitted intensity of the sample in comparison with the transmitted intensity of a cuvette with pristine solvent. One has to keep in mind that the absorption, *e.g.* the ratio of absorbed photons of a sample versus a blank sample, is usually not the same as the extinction or absorbance. Based on the Lambert Beer's law the absorption can be calculated using:

$$A = 1 - 10^{-E} \tag{1.3}$$

Applying a first order Taylor-expansion one could get that the standard approximation that absorption is approx. the same as the absorbance for small absorbances. From the experimental point of view most standard UV-vis spectrometers determine the transmission, which is the intensity of the probe beam divided by the intensity of the reference beam.

Within this thesis UV-vis spectra where recorded with a Varian CARY 5000 spectrometer using quartz glass cuvettes with a beam path of 1, 4, or 10 mm. Illumination experiments where measured on a JASCO 530 UV-vis spectrometer with an additional LED port for illumination of the samples. The illumination was performed with a 455 nm high power LED obtained from Thorlabs. The LED was controlled using a Thorlabs DC4100 LED driver. The JASCO spectrometer and the LED driver were controlled using a self-written Labview program for an automatic measurement with constant illumination times and intensities. Since Labview VIs were only

available for the LED-driver, the spectrometer had to be controlled using the RS-232 protocol, which was kindly provided by the support of JASCO. The single commands were send using National Instruments Virtual Instrument Software Architecture (VISA). Here the commands can directly be transferred to the spectrometer and also the answer of the spectrometer can be read from the RS-232 buffer. It has to be noted that the RS-232 communication parameters have to be set manually to the correct values needed by the spectrometer. For example the baud rate had to be set to 4800 and the Flow control to Xon/Xoff.[93]

Data analysis for illumination dependent UV-vis measurements

The derived 2D-datasets were plotted as spectral or kinetic traces. The kinetic traces could be fitted using different models explained in Chapter 3. Additionally a singular-value decomposition (SVD) analysis was performed, which is a common method for the data analysis of hyperspectral images.[94] This method splits the 2D matrix of absorbance values (A-matrix) into a spectral component (U-matrix) and a specific kinetic trace for every component (V-matrix). This is coupled by the diagonal S matrix, which gives a weighting of the single component. The diagonal values are usually merged into a vector S in descending order.

$$A = U \cdot S \cdot V^T \tag{1.4}$$

To determine the significant components only those components are chosen, which have a reasonable high value in the corresponding element of the S vector. The SVD analysis was performed using the respective tool in the Labview math package. For a better data handling the program was written in a way that it is able to directly import the output files from the automatic illumination experiments performed on the JASCO 530 UV-vis spectrometer. Only data for wavelengths above 270nm were used for the SVD analysis, due to the absorbance of the solvents in the near UV spectral region. The here gained kinetics were afterwards fitted using different models.[95]

For a better comparison of the kinetic traces all kinetics were multiplied by the corresponding value of the S-vector. This is needed to compare the impact of a given spectral component to the overall kinetics. This normalization was chosen because the spectra found in the U-matrix were more or less normalized with respect to each other. One example of the determined spectra and kinetics for **D2A** in CF is shown in Figure A 6.

Fluorescence Spectroscopy

Emission spectra were recorded on a home built setup. This setup was designed and optimized to measure even smallest emission intensities of solutions and thin films. The basic emission setup is shown in Figure 7. The overall measured fluorescence intensity F_x with a fluorescence spectrometer is determined by

$$F_x = I_0 \cdot A_x \cdot \Phi_x \cdot M_{Spec} \tag{1.5}$$

Were I_0 is the intensity of the excitation light, Φ_X is the fluorescence quantum yield and M_{Spec} is the sensitivity curve of the emission spectrometer at all measured emission wavelength. A_x is the absorption calculated by

$$A_{x,s} = 1 - 10^{c_{x,s} \cdot d \cdot \varepsilon_{x,s}} \tag{1.6}$$

The quantum yield for fluorescence depends on the difference of rates of depopulation of the excited state of the molecule. Here we discriminate between a fluorescent Γ and a dark k_{NF} recombination rate, while the latter one is usually a combination of different processes and rates. The overall quantum yield can be calculated by

$$\Phi = \frac{\Gamma}{\Gamma + k_{NF}} \quad . \tag{1.7}$$

As seen from the first equation it is essential to maximize $M_{spec}(\lambda)$, which basically gives the quantum efficiency of the complete emission setup for the desired emission wavelength range to measure even smallest emission intensities. The M_{spec} sensitivity basically describes how many photons from the sample at a given wavelength actually lead to an electronical measurable signal. In the case of the usually used CCD cameras or photomultiplier tube detectors the signal efficiency measure is the number of counts detected for a given number of incident photons.

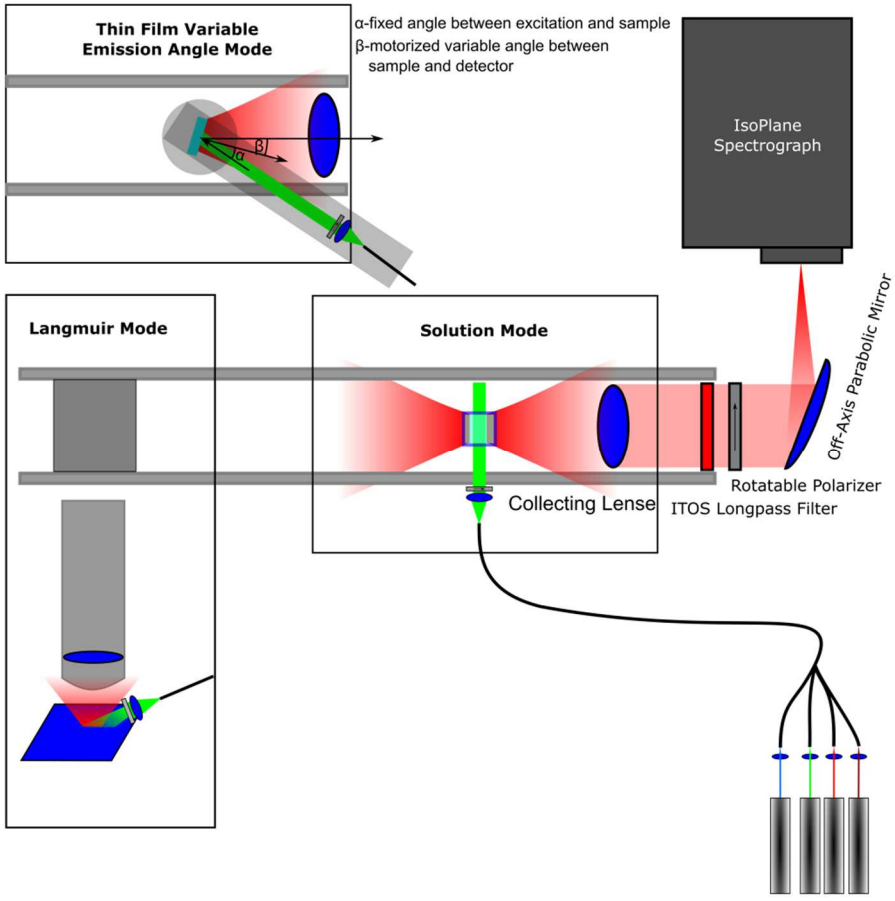

Figure 7 Experimental setup for emission spectroscopy. As excitation source 4 fiber coupled laserdiodes with 5mW power and wavelengths of 405, 450, 532 and 635nm are used.

The emission spectrometer built for this thesis is shown in Figure 7 consists of an Isoplane SCT 320 spectrograph from Princeton Instruments and a Pixis 400 eXcelon CCD camera also from Princeton Instruments. The spectrograph is equipped with silver mirrors to reduce reflection losses in comparison to the normally used aluminum mirrors. This is very favorable by means of a higher overall sensitivity, but has the drawback of completely losing the possibility of measuring emission below approximately 400 nm. To further enhance sensitivity in the NIR

region a second grating was added to normally used UV-vis grating with 1200 lines per millimeter and a blaze wavelength of 500 nm. This NIR-grating is blazed at 1000 nm with only 600 lines per millimeter. The blazing at 1000 nm enhances the overall sensitivity in a region were the quantum efficiency of the silicon CCD camera drops, with the drawback of a reduced wavelength range to be measured. The range is reduced from 400-1050 nm to 600-1050 nm, for the vis and the NIR grating, respectively. For measuring space-resolved emission an additional silver mirror was placed on the grating tower. The coupling of the emitted light to the spectrometer is done by collimating the light by an achromatic lens couple with a focal length of 50 mm. The collimated light is guided through a magnetic mounted long pass optical filter with low inherent fluorescence obtained from ITOS. This is needed to reduce the intensity of scattered excitation light. Furthermore, it is possible to mount a broad band polarizer right after the long pass filter. The light is then focused with an off-axis parabolic mirror with a matched aperture ratio of four to the entrance slit of the spectrograph. The excitation can be done in two different ways. The common source consists of four different laser diodes with a power output of approximately 5mW. The light is then coupled into a special fiber package with four single ports to input the laser light. On the other end, all fibers are fused to get one output. The light is then collimated with an achromatic fiber port obtained from Thorlabs. As second excitation light source a broadband source obtained from LOT-Quantum design was used. This source consists of a 260 mm monochromator which is directly coupled to a 450 W Xe lamp. The monochromatic light is then coupled into a glass fiber bundle made of 68 single fibers with a fitted numerical aperture of 0.22. The light is finally collimated at the end of the fiber to illuminate the sample.

To accommodate a wide range of samples to be measured two sample chambers were constructed. The first one is made to hold standard cuvettes with 12x12 mm^2 external dimensions (See Solution Mode in Figure 7) and thin films on substrates with a width of five to ten mm and a thickness of up to 1 mm. The angle between excitation and emission is set to 90°. The angle between excitation and the sample normal of the solid substrate can be adjusted in a range of 30° to 60°. This holder is installed by easily replacing the cuvette holder in the Solution Mode shown in Figure 7. The second measuring chamber (See Thin Film Variable Emission Angle Mode in Figure 7) was designed to measure solid state samples and solutions angle dependent emission. This is done by holding the angle and distance between excitation and sample constant, but changing the angle between sample and emission spectrometer. Changing the angle between sample normal and spectrometer entrance can be done automatically using a software controllable step motor obtained from Thorlabs. Furthermore, polarizers can be added to the excitation and the emission pathway. At last it is also possible to measure fluorescence directly on the water surface of our Langmuir-Blodgett trough, as shown in the Langmuir Mode in Figure 7.

After all optimization steps the exclusion of any stray light had to be done. This was achieved using a black metal housing, which was further improved by using black out foil wherever stray light came into the housing. Furthermore, scattered light with a wavelength of 940 nm from the laser diodes, included in the Wilhelmy balances of the Langmuir-Blodgett trough, had to be blocked.

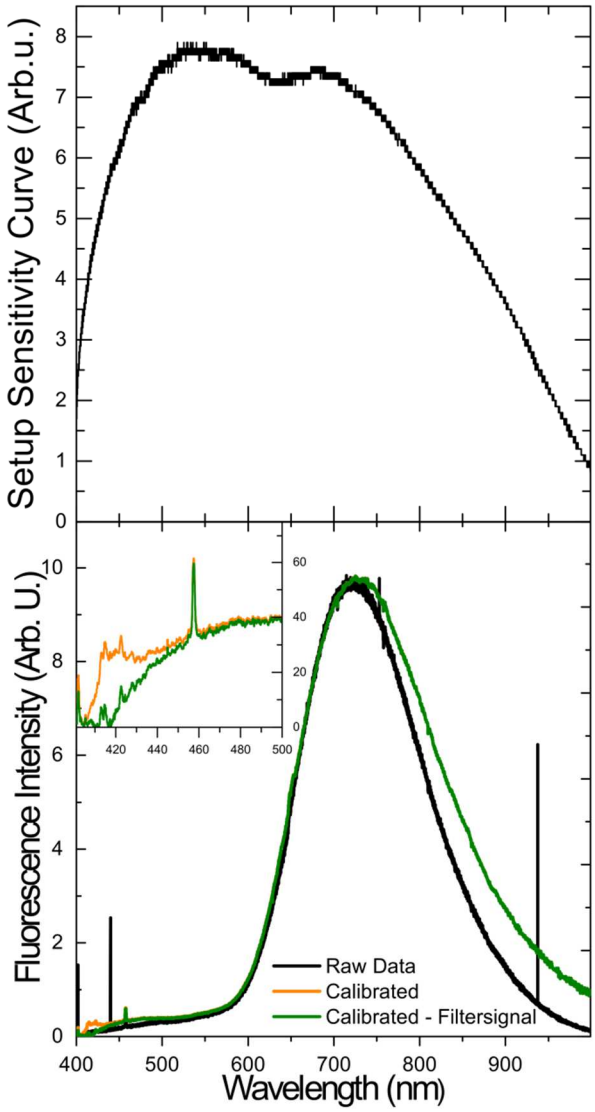

Figure 8 Setup sensitivity curve for our fluorescence setup (top) and a comparison of the raw data with either the calibrated data (removed cosmic rays and sensitivity corrected) or the calibrated date were the residual fluorescence from the laser filter is also subtracted. The parameters used here are: grating: 1200 l/mm, 500 nm blaze; slit width 500 µm; step and glue mode with 4 nm minimal overlap.

The collected emission spectra had to be corrected for the overall setup sensitivity curve and cosmic rays had to be removed. One example of the raw and corrected data is shown in the lower panel of Figure 8. Here the black curve is the raw emission spectrum obtained from the setup, the orange curve represents the data with removed cosmic rays and corrected for the setup sensitivity curve shown in the upper panel of Figure 8. The final green curve is obtained by also subtracting the residual filter fluorescence of the long pass filter used to block scattered excitation light. Furthermore, for very low emission intensities, the residual fluorescence from the long pass filters had to be removed. All these tasks were done using a self-written Labview program. To obtain the setup sensitivity curve a 100 W halogen lamp was used as reference[75]. The intensity of this kind of lamps is very well described by a black-body radiation with a temperature of 3100 K using the following formula:

$$I(\lambda,T)dAd\lambda = \frac{2\pi hc^2}{\pi^5}\cdot\frac{1}{e^{\frac{hc}{\lambda kT}}-1}dAd\lambda \tag{1.8}$$

with *h*, *c*, *k* being the Planck constant, speed of light and Boltzmann constant, respectively. The determination of absolute fluorescence intensities depends on numerous factors beginning with the intensity of the excitation source and ending with geometrical uncertainties, *e.g.* sample positioning or slightly fluctuations in the setup geometries. Hence, it is common to correct the measured spectra with the spectral sensitivity curve obtained by getting the quotient of the measured spectra of the halogen lamp and the known spectral shape of the black body radiation. This gives us the correct spectral shape with an unknown constant pre-factor. This pre-factor is afterwards determined by normalizing the integrated fluorescence to the integrated fluorescence of a standard with known quantum yield measured under the same experimental conditions[96]. To address the possibly high differences in the quantum yield of standard and molecule under investigation, the integration time should be the only parameter that has to be adjusted. This is done to prevent any deviations due to possible changes in the sensitivity curve of the whole setup, like *e.g.* an altered optical resolution having different slit width. The overall spectral sensitivity curve of the used setup is given in the upper panel of Figure 8.

Using fluorescence standards suited for every excitation wavelength also omits the need to exactly determining the excitation intensity. The quantum yield is calculated using the formula[97]

$$\Phi_X = \frac{A_X}{A_S}\cdot\frac{F_X}{F_S}\cdot\frac{n_x^2}{n_S^2}\cdot\Phi_S \tag{1.9}$$

With the unknown quantum yield Φ_X, the quantum yield of the standard Φ_S and the absorption of standard and sample, A_s and A_x, respectively. The indices of refraction of the sample and standard are n_x and n_s. For our setup, mainly two standards are used. Perylene for the excitation wavelength of 405nm and Rhodamin B for 532 nm, each dissolved in ethanol. The literature known fluorescence quantum yields are 0.92 and 0.5 for Perylene and Rhodamine B dissolved in ethanol, respectively[96]. The spectra of the filters were measured using a blank glass slide to reflect a small portion of the excitation light through the longpass filter in front of the spectrometer.

Femtosecond Transient Absorption Spectroscopy

To get a deeper insight into the processes right after photoexcitation transient absorption spectroscopy (TA) is used. With this pump-probe technique processes on the time scale of several hundreds of femtoseconds to several nanoseconds can be observed.[98] Time dependent transient absorption spectroscopy is typically done in two time regimes with different experimental techniques. For slower processes systems with nanosecond time resolution are used. These systems measure the transmission directly after a pump pulse was send to the sample. The pump pulses have a typical temporal resolution of a few nanoseconds. A continuous wave probe light is used and a detector with a high readout speed. As detectors photomultiplier

tubes or avalanche detectors with a typical read out frequency of approx. one GHz are applied. Hence the minimal time resolution available is approx. one ns for a GHz detector read out. [98]

Processes like energy or charge transfer in organic dyes for optoelectronic devices usually occur in the time regime of several hundred femtoseconds to a few nanoseconds.[99-101] Hence, a different technique has to be applied. Here the femtosecond transient absorption spectroscopy is the tool of choice. This technique is based on a controlled time delay between an ultrashort pump and probe pulse hitting the sample of interest. The time delay is set by varying the path length of either pump or probe pulse by a mechanical delay line. A typical delay line has the length of 30 cm giving a maximum difference in path length of 60 cm. This gives an upper limit of the observable delay time window of approx. two ns. The lower limit is usually given by the temporal width of the pump and probe pulse. For the here used setup this is approx. 100 fs.

The basic setup is shown in Figure 9. The control box, shutter, diodes, data collection, and evaluation software were built by Pascher Instruments AB.

The setup consists of a pump laser (Legend-Elite or Libra from Coherent Inc.), which delivers IR pulses with a wavelength of approx. 800 nm and a pulse length of approx. 100 fs. The pulses are generated with a frequency of 1 kHz. The output beam of this laser is first split into a pump pathway (95% intensity) and a probe pathway (5% intensity). The pump pathway consists either of a TOPAS Optical Parametric Amplifier (OPA) from Light Conversion or a BBO crystal to create the second harmonic at round about 400 nm. The pump beam is then modulated by a chopper, which is set to 500 Hz to remove every second pulse. For this work the pump beam is then guided to the delay line from PI to set the time delay between the pump and probe pulses. At the end the pump beam is focused and guided through a hole in the probe focusing concave mirror to the sample. Afterwards the pump beam is guided through the hole in the second concave mirror to a beam dump.

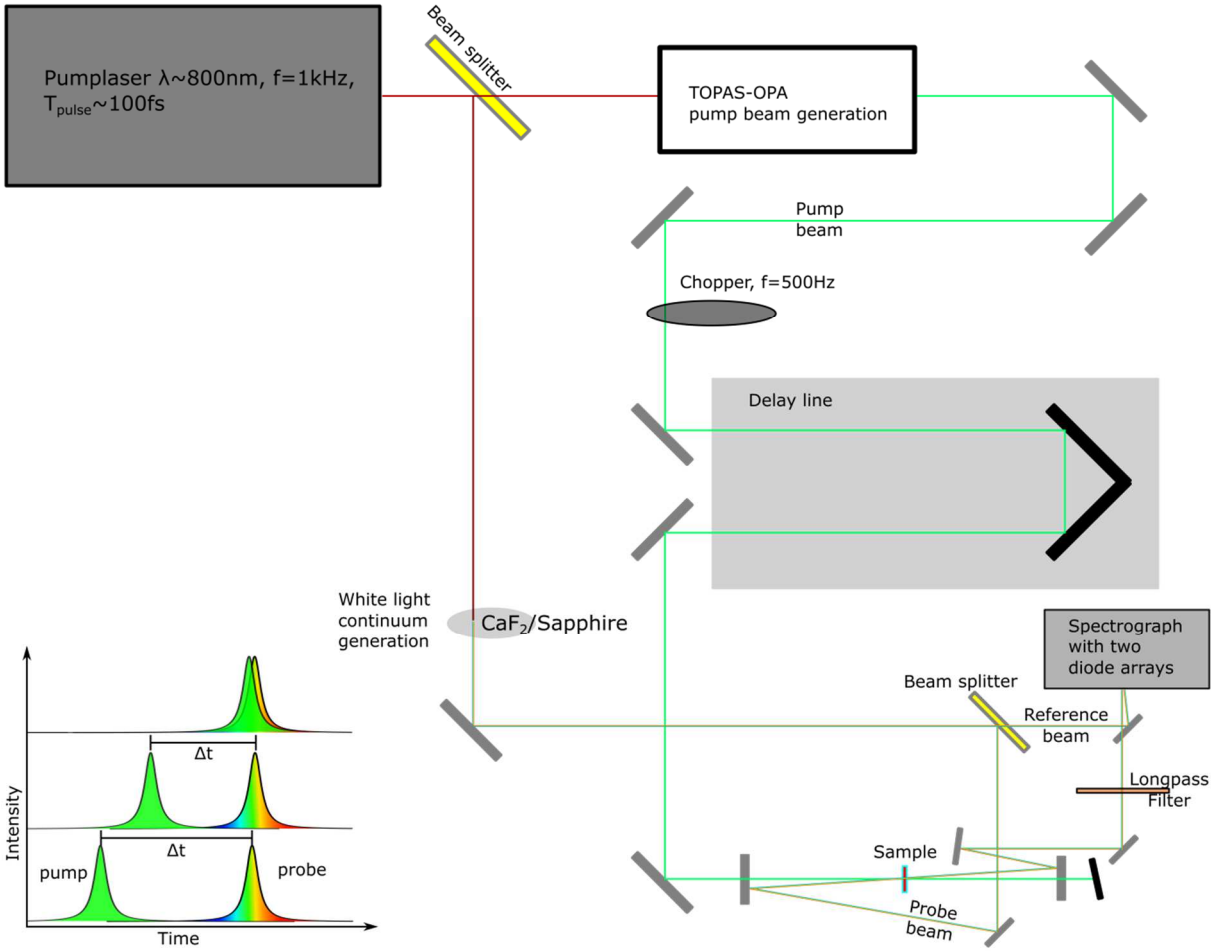

Figure 9 Used fs-TA setup. The setup consists of a pump laser, which delivers IR pulses with a wavelength of approx. 800 nm. These fundamental pulses split to create a pump pulse in an OPA and a white light continuum probe pulse in either CaF_2 or sapphire. The delay between pump and probe is set using a delay line giving a defined temporal delay in the range of 2 ns with approx. ten femtoseconds resolution.

The probe pathway consists of a sapphire or CaF_2 plate[102] in which the 800 nm beam is focused to create a white light continuum. The white light continuum is collimated and split by a 50/50 beam splitter into a reference and a probe beam. The reference beam is then directly guided to the spectrograph with a beam height that matches the lower diode array attached to the spectrograph. The probe beam is guided to the sample by a concave mirror, which focuses the beam on the sample. After passing the sample, the sample beam is collimated by the second concave mirror and guided to the spectrograph. The beam height is set to match the upper diode array attached to the spectrograph. Additionally, two filters are put into the probe pathway. The first longpass filter is set to the sample pathway in front of the spectrograph to remove scattered pump light. Furthermore, a filter to remove excess intensity of the 800 nm laser is set directly in front of the spectrograph into sample and reference pathway. This is needed since a big part of the 800 nm fundamental is not converted into white light continuum. This intensity usually oversaturates the diode array in the spectral range of 700-800 nm. By using this filter the available spectral range is limited to approx. 780 nm.

The TA signal is determined by calculating the differences of the absorbance for a pulse were the pump is blocked by the chopper with one where the pump is not blocked.

$$\Delta Abs = Abs_{pump} - Abs_{blocked} = \lg(I_{ref} / I_{probe})_{pump} - \lg(I_{ref} / I_{probe})_{blocked} \quad (1.10)$$

Usually 400 probe pulse pairs are used to determine one data point, which means one TA spectrum at a given delay time. To reduce the effect of pump intensity fluctuations five to ten complete delay time scans are averaged for one measurement. Using white light as probe light has the advantage of getting a complete TA spectrum with one shot, but has the drawback of a relative high noise level of approx. 0.5 mOD for 400 pulse pairs. This limit can be crucial for thin films with low optical density, like e.g. Langmuir-Blodgett films used in this work.

The data analysis for fs-TA data is usually done by using a fitting software from Pascher Instruments. Within this software the measured data are first corrected for the chirp, which is caused by the dispersion of the index of refraction of all optical elements within the pathway of the white probe light. This chirp can be identified by fitting the temporal position coherent artifact[103] for each measured wavelength. After this artifact is fitted the data array is corrected by shifting the signals of a given delay time and wavelength in a way that the delay time is given as a difference to the measured coherent artifact. Furthermore the artifact region is removed for the later data fitting. The fitting is done by using a multi-exponential decay function with a pre-factor which is a function of the wavelength.[104, 105]

$$\Delta Abs(\lambda, t) = \sum_{N} A(\lambda)_N \cdot e^{-k_N t} \quad (1.11)$$

With ΔAbs being the measured transient absorption data, N being the number of used exponential decay functions, k being the decay rates, A being the decay associated spectra and t the decay time. For a better fit it is also possible to implement an infinity component to describe decay components which have time constants above the maximum delay time measurable.

Since this model is hardly able to account for shifts in observed excited state absorption (ESA) features an alternative fitting program was developed. This Labview program imports the chirp corrected fs-TA data and changes first the wavelength axis to a photon energy axis. This is needed since the broadening of peaks should be symmetric in energy and is hence strongly asymmetric on a wavelength scale. With these data ΔAbs spectra for every single decay time are fitted with up to three Gaussian peaks with a Levenberg–Marquardt algorithm. The starting parameters are set and fitted separately for the very first delay time. Afterwards these parameters are used as first guess for the spectrum of the next delay time. With the gained parameters one could follow the peak shifts, which will give the cooling kinetics separately from the decay.

2.4 Aggregate characterization in solution

Aggregates in solution were investigated using a commercially available dynamic light scattering setup (DLS) from ELV (ALV Laser CGS3 Goniometer). This method is a standard technique to determine micelle or aggregate size distributions in solution or dispersions[106]. The used setup uses a HeNe-Laser with a wavelength of 633 nm as light source. Dynamic light scattering is based

on the observation of speckle patterns[107] formed by the interaction of coherent light with mater. In this case the speckle patterns are created by the random scattering of laser light by particles within dispersions. In the case of DLS the speckle patterns are not measured in a special domain, but rather in the time domain using a single detector. The measured signal is the intensity fluctuations of the scattered light due to the Brownian motion of the particles. The measured intensities are analyzed using an auto correlator to determine the autocorrelation function. With given temperature and viscosity of the dispersion media the autocorrelation function can be fitted to get information about the particle size distribution[108].

On the date recording the scattered light intensity measured by the detector can have different signal strengths, meaning that the number of detected counts varies. Hence as more scattering particles are present in the dispersion, the attenuation of the system has to be reduced. It has to be noted that the signal strength in DLS gives only a rough estimate on the particle density and strongly depends on the experimental parameters. Hence only large differences can be used as a hind to approximate the relative particle concentration.

2.5 Morphological Characterization

Large scale thin film homogeneities were assessed by means of standard optical microscopy. AFM measurements were performed on the atomic force microscope (AFM) DI dimension 3100 in tapping mode. Silicon cantilevers with silicon oxide tip surfaces where used. These can be assumed to be OH-terminated and, hence, have a hydrophilic surface due to their being stored at ambient conditions. The tip radius is approximately 10 nm. The collected data were afterwards processed by using the open source program Gwyddion[109]. A mean plain correction and the removal of scars was performed to obtain significantly better AFM pictures. Beside the surface height profiles also phase images were recorded. These phase images usually give information about the local environment and the interaction between surface and tip.

3 Aggregation and Photoaggregation of Merocyanines in Solution

For dyes which are finally applied as thin solid films, such as in optical layers[60, 86, 110], active layers in organic[4-8], dyes sensitized[43, 111, 112], or hybrid solar cells[113-115], sensors[116, 117] as well as organic light emitting diodes[60, 118-120] their supramolecular structure essentially determines the thin film's[121-125] and device' properties[126]. While the molecular interactions between many dyes with extended π-systems are governed by dispersion interactions[127, 128], dipol-dipol interactions[129] are essential for highly dipolar merocyanine dyes.[130, 131] However, the dipole-moment of push-pull dyes can typically be further enhanced upon charge transfer (CT) excitations[19, 43, 132, 133], thus possibly causing the formation of different supramolecular structures as compared to the dark. Consequently, it appears to be essential to determine the influence of light on supramolecular structure formation, which was recently reported for cyanine dyes[58], and to discriminate it from photodegradation[134] for the development of photoactive materials.

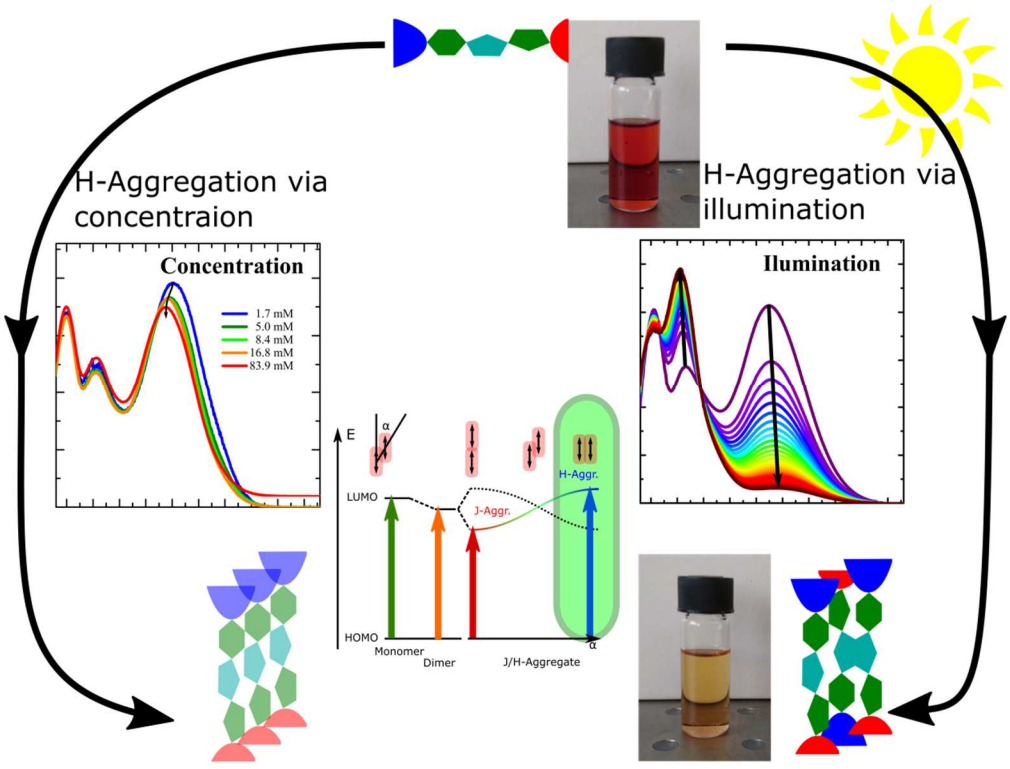

Figure 10 Overview of the two ways of (H-) aggregate formation in solution described in this chapter. On the left hand side the aggregate formation *via* higher concentrations is shown, which is caused by the ground state characteristics and geometry of the molecules. On the right hand side the faster photo-aggregation is shown, which is facilitated by the characteristics in the excited state of the molecules.

In this chapter we use dipolar merocyanines shown in Figure 3, which vary in the length and chemical nature of their π-bridge between donor (D) and acceptor (A) moieties, to tune the

balance between CT and π-π* characters of the $S_0 \rightarrow S_1$ electronic transition. Thus, supramolecular structure formation will be varied by both, the weight of dipole-dipole interaction on the total intermolecular interactions as well as the molecular shape, which changes with increasing π-bridge length. We investigate the supramolecular structures formed by means of UV-vis absorption, fluorescence spectroscopy and dynamic light scattering techniques (DLS). The obtained data were afterwards correlated with already established kinetic models. The origin of the aggregate formation processes was investigated using quantum chemical calculations. With these results, we could show that this kind of DSSCs tends to build aggregates in solution by increasing the concentration. Furthermore, these molecules can create aggregates upon using illumination to act like a catalyzer in a photo-annealing process.

3.1 Electronic Structure of Individual Merocyanines

The three derivatives **D2A**, **D3A** and **D4A** feature an intense absorption band at ~520 nm; with increasing the π-system the maximum of the absorption shifts slightly to shorter wavelengths (**D2A**, **D3A**, **D4A**: 530, 520, 493 nm), *cf*. the results of Menzel *et al*.[71] for **D3A** and **D4A**. In each case the electronic transition features a rather weak CT, but a considerable π-π* character according our time dependent functional theory (TD-DFT) calculations performed by Torsten Sachse. This character of the electronic transitions is visualized by means of charge difference density[135-138] plots in Figure 11, which show the change in total electron density upon photoexcitation into the S_1-states. The centers of charge depletion are mainly localized at the triphenylamines, while charge accumulation predominantly happens at the α-cyano carboxylic acid groups, and pronounced π-π* excitations are observed at all hetero-cycles. However, with increasing the length of the π-bridge the CT character of the $S_0 \rightarrow S_1$ transitions increases as reflected in the charge difference density plots in Figure 11 and also depicted by the S_1 excited state dipole moments μ (μ_{S1}(**D2A**, **D3A**, **D4A**)=21.8, 29.8, 26.3 D) as compared to the S_0 electronic ground states (μ_{S0}(**D2A**, **D3A**, **D4A**)=9.1, 9.1, 10.5 D) derived by TD-DFT.

The experimentally observed adjacent energetically higher absorption peaks are located at 348, 370, and 410 nm for **D2A**, **D3A**, and **D4A**, respectively, as shown in Figure 11. The corresponding TD-DFT stick-spectra shown in Figure 11 resemble the low-energy absorption peaks of **D3A** quite well, while in case of **D4A** the assignment of the $S_0 \rightarrow S_2$ transition to an experimental peak is challenging. The above mentioned experimental **D4A**-peak at 410 nm might be due to this $S_0 \rightarrow S_2$ transition or due to H-aggregate formation (see below), which might appear even at low dye concentrations[139]. In the case of **D2A** the uniformly applied energetic shift (280 meV) of the TD-DFT-derived energies is too small to match the experimentally determined energies, presumably due to the different CT/π-π* ratio of the energetically lowest transitions of **D2A** as compared to **D3A** and **D4A**. Taking possible further shifts of the TD-DFT-derived transition energies into account, the experimentally observed **D2A**-peak at 348 nm can be assigned to the $S_0 \rightarrow S_2$ transition.

All dyes show spectrally broad fluorescence ranging far to the IR, *i.e.* displaying a significant Stokes shift. The Stokes shift gets larger upon increasing the π-bridges and is determined to 420,

640 and 790 meV, for **D2A**, **D3A** and **D4A**, respectively. This Stokes shift increase indicates a stronger geometric change in the S_1-states with increasing π-bridge length.

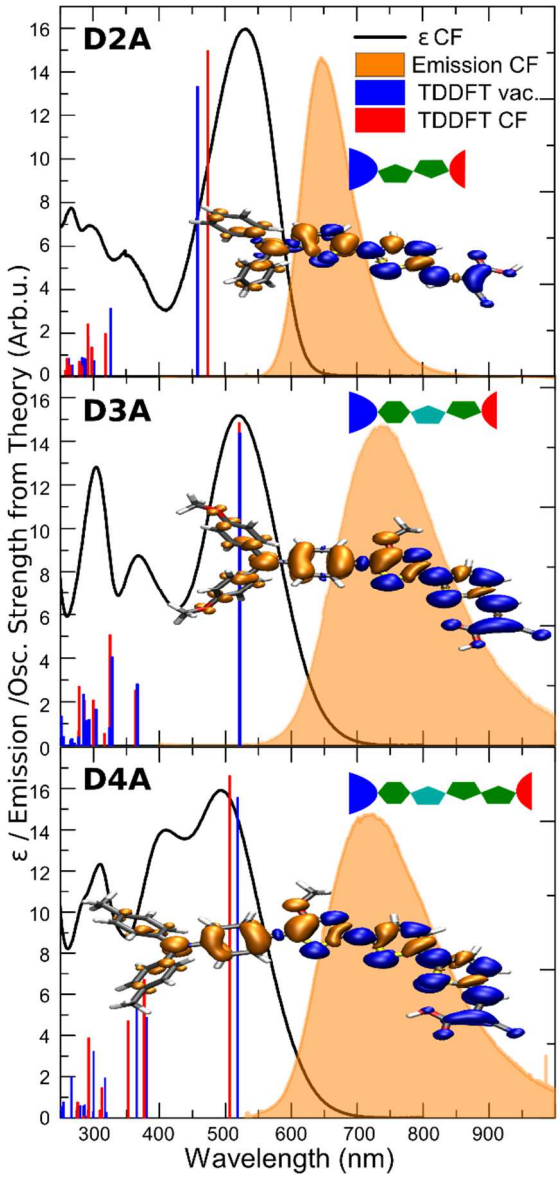

Figure 11: Experimental molar extinction and fluorescence spectra of all molecules in chloroform solution in comparison to the stick spectra derived from theory. All theoretically derived absorption energies where shifted by 280 meV to lower values to facilitate comparison to the experimental results. The volumetric data plotted on the molecular structures represent photo-induced changes in the electron density distribution at the Franck-Condon point of the $S_0 \rightarrow S_1$ transition (orange: electron depletion, blue: electron accumulation; accounted for chloroform solvation by means of COSMO).

3.2 Aggregate Formation

After having characterized the basic absorption features of the merocyanines in solution, changes in the absorption spectra due to aggregate formation are discussed in the present section. The aggregate formation is induced in two different ways: Either by increasing the dye concentration while keeping the sample in the dark, *i.e*. ground state aggregation, or by

irradiating a given solution, *i.e*. excited state- or photo-aggregation. These two different procedures give rise to markedly different changes in the absorption spectra as shown in Figure 12. Therefore, we assume that concentration-increase and irradiation lead to different supramolecular structures with distinct absorption spectroscopic properties as discussed in more detail in the following.

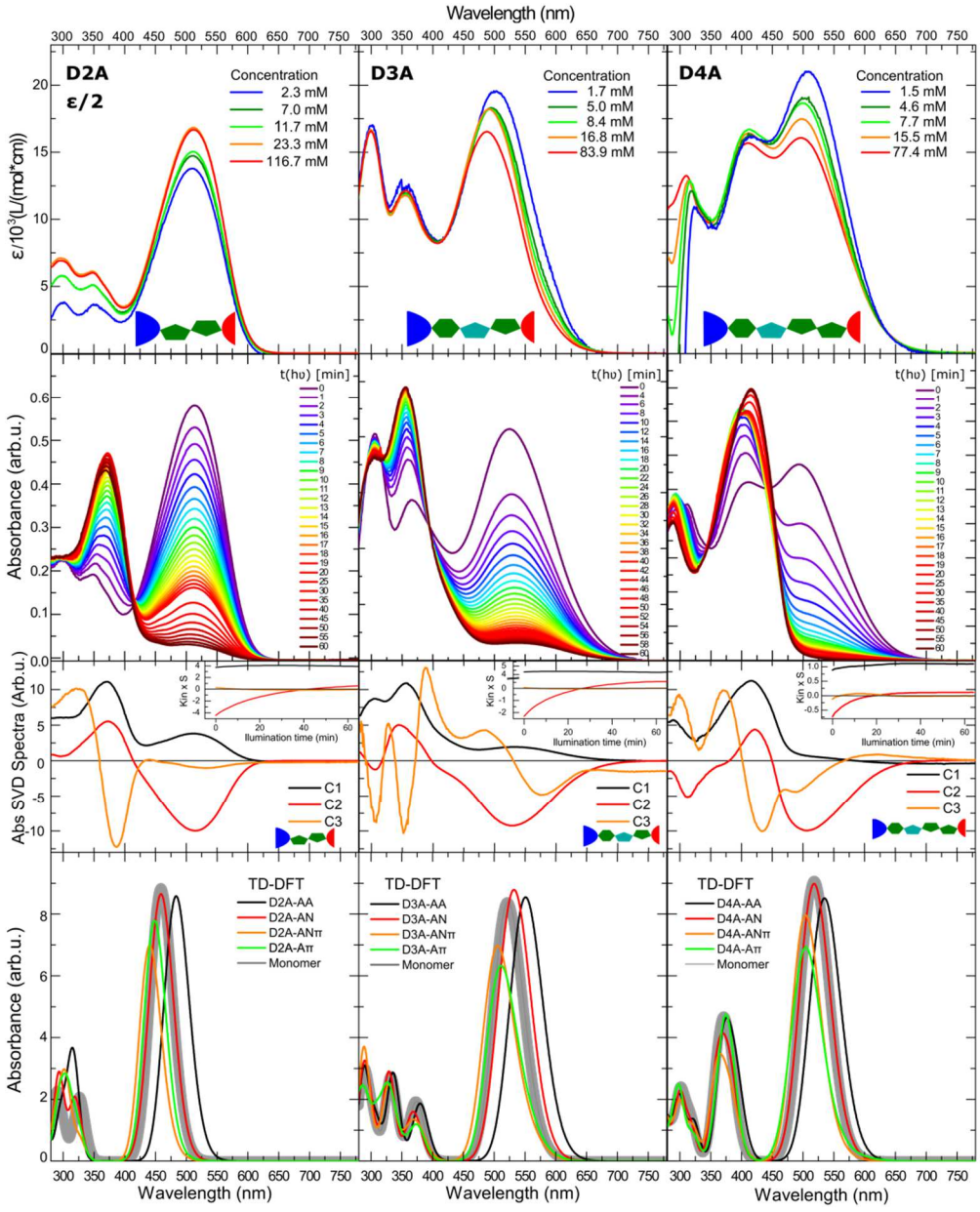

Figure 12: Experimental extinction coefficient and absorption spectra of **D2A**, **D4A** in chloroform and **D3A** in THF at systematically varied concentrations (top), irradiation times (middle: absorbance and significant components C1, C2, C3 together with their kinetics (see inset) as revealed by a singular-value decomposition - SVD) and derived from time-dependent density functional theory calculations for different dimers (bottom). The extinction coefficient of D2A was divided by a factor of two to facilitate comparison.

Ground State Aggregation

Increasing the concentrations of **D2A**, **D3A** and **D4A** causes small absorption decreases accompanied by minute blue-shifts of the $S_0 \rightarrow S_1$ absorption peaks while the ones assigned to the $S_0 \rightarrow S_2$ transitions are rather unaffected by concentration changes as shown in Figure 12.

These absorption changes are slightly weaker, but in the range of the values reported for merocyanines that form H-aggregates to compensate their molecular dipole moments.[129, 130, 139] In our case the extinction coefficient and hence the monomer concentration, decreases by approx. 30% by increasing the concentration by almost two orders of magnitude in the case of **D3A** and **D4A**, while the extinction coefficient is decreasing by up to approx. 70% for merocyanines described by Würthner *et al.*[129] In the latter case typical spectral series of aggregate formation show the rise of a blue shifted dimer peak at the cost of a low-energy monomer peak, involving an isosbestic point. In contrast, the concentration-induced aggregation observed in this work appears to follow a different aggregation-mechanism than the typical dipole-dipole compensation mechanism. Consequently, the total intermolecular interactions need to be considered to understand the mechanism of formation of **D2A**, **D3A** and **D4A** aggregates.

As mentioned above, London dispersion interactions are expected to significantly contribute to the intermolecular interactions.[127] Their weight is expected to grow with increasing length of the π-bridge from **D2A**, **D3A**, to **D4A**. Additionally, the heteroatoms in the π-bridges of **D3A** and **D4A** induce polarity to the π-bridges as shown by the electrostatic potentials at the van der Waals surfaces in Figure 13. Furthermore, the α-cyano-carboxylic acid moiety might be involved in hydrogen bonding by means of the acid[140, 141] and the cyano group.[142, 143] Moreover, both, hydrogen bonds[144] as well as π-stacks[145-148], can give rise to step-growth to larger aggregates.

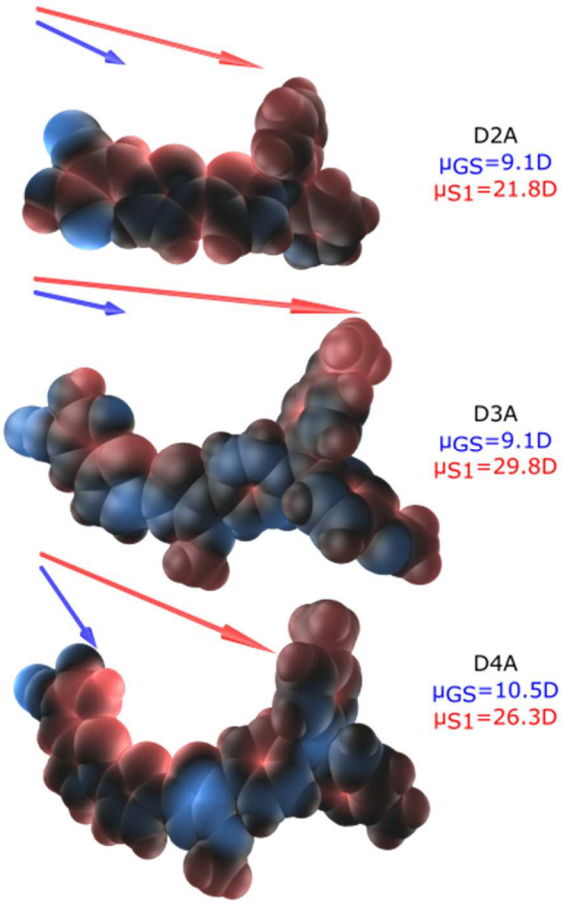

Figure 13: Electrostatic potential at the van der Waals surface of the investigated merocyanines in the S_0 state together with the S_0 and S_1 dipole moments μ_{S0} and μ_{S1}, respectively (in vacuum relaxed geometries). The blue and red arrow represents the dipole vector of the S_0 and S_1 state, respectively.

Because of interplay between the before mentioned different intermolecular interactions the aggregate formation is highly complex. Therefore, energetically favorable dimer structures were identified by systematic grid-based scanning of dimer geometries, using the recently introduced molecular modelling tool *EnergyScan*[149], rather than by chemical intuition-guided manual dimer creation. With *EnergyScan* all dimer geometries with a binding or dimerization energy up to 25 meV above the global minimum energy were identified and the 20 most distinct geometries were automatically detected. Out of the twenty dimers identified this way the ones with the most distinct absorption spectra are shown in Figure 12 and can be assigned to either of the following archetype binding motifs (see Figure 14 for the dimer geometries, Figure A 1 of the appendix for electrostatic potentials at the van der Waals surface of the dimers; selected geometric parameters of the dimers can be found in Table 5 of the appendix):

AA: Double hydrogen bond between the two carboxylic acids (abbrev. AA); limited to dimerization, allows no further aggregate growth

AN: Double hydrogen bond between a carboxylic acid and the nitrile together with its neighboring β-hydrogen (abbrev. AN); not limited to dimerization, allows for further aggregate growth

ANπ: AN-binding motif, but rotation around the C(OOH)C(CN)-bond enables ππ-interactions (abbrev. ANπ); not limited to dimerization, allows for further aggregate growth

Aπ: Interaction between the α-cyano carboxylic acid and the π-bridge (abbrev. Aπ); presumably not limited to dimerization, allows for further aggregate growth

Table 1: Dimerization energies E_{dim}, dipole moments of the ground and S_1 excited states ($\mu_{dim\text{-}GS}$, $\mu_{dim\text{-}S1}$, respectively) of merocyanine dimers and angles between the individual molecular groundstate dipole moments within the identified archetype dimers

		Dimer Type	**AA**	**AN**	**ANπ**	**Aπ**
$\mathbf{E_{dim}^{min}}$	[kJ/mol]	D2A	108.1	56.9	63.7	39.6
		D3A	94.6	54.6	74.3	39.6
		D4A	109.0	73.3	101.4	42.5
$\mu_{dim\text{-}GS}$	[D]	D2A	0.42	2.99	13.05	1.62
		D3A	0.53	6.12	15.38	5.49
		D4A	0.35	11.69	1.44	6.36
$\mu_{dim\text{-}S1}$	[D]	D2A	0.44	9.35	26.99	0.85
		D3A	1.39	17.63	36.93	14.84
		D4A	1.80	30.22	14.70	15.19
$\alpha(\mu_1,\mu_2)$	[°]	D2A	175	8	25	164
		D3A	177	155	21	134
		D4A	170	105	11	161
Step-Growth			no	yes	yes	pos-sibly

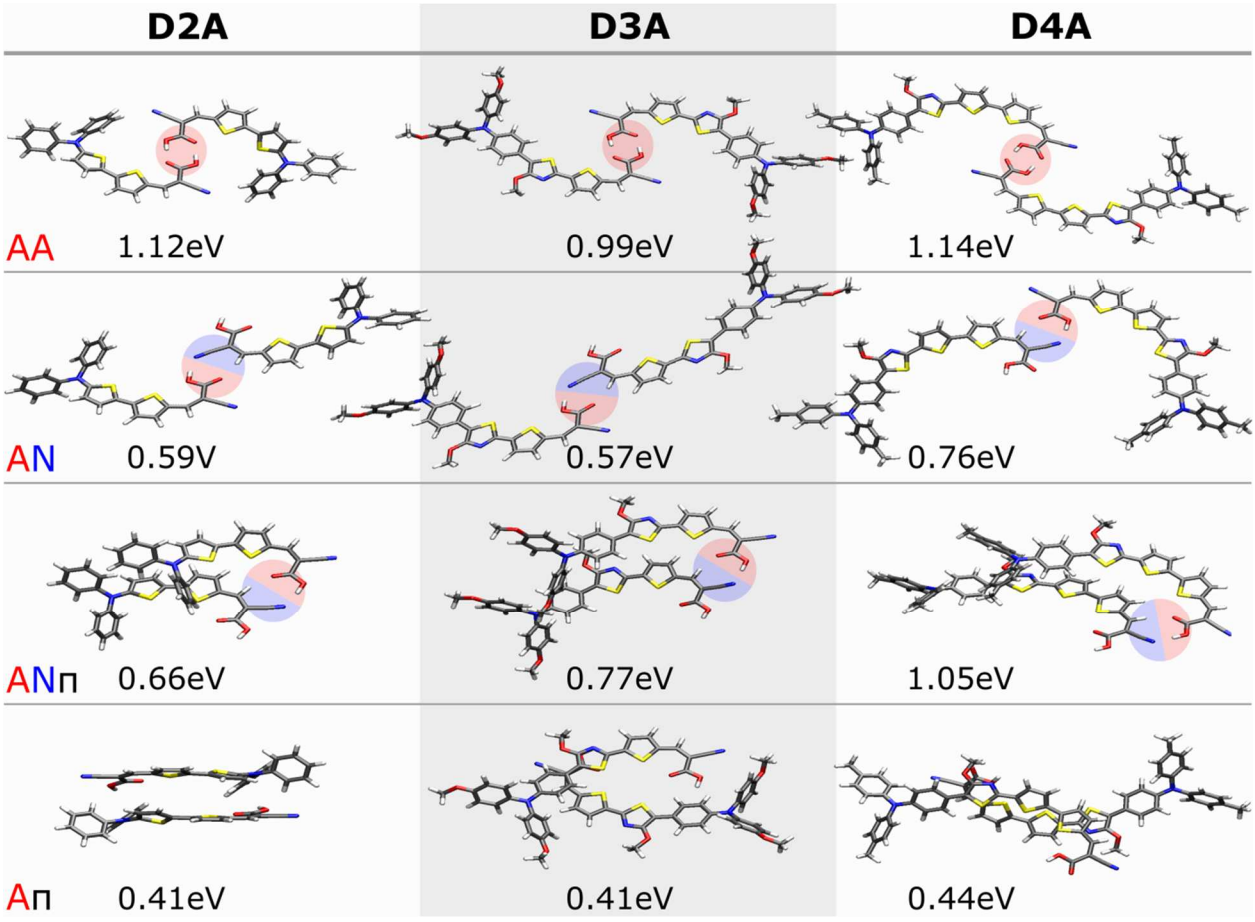

Figure 14: Structures of all dimers discussed.

According the DFT-derived dimerization energies (Table 1 and Figure 14) AA-type interactions are energetically favorable in vacuum and presumably in very non-polar media as compared to the other investigated interactions mentioned above. In the rather polar solvents used in this study we expect a considerable screening of the surface charges at the acid groups[150]. Thus, we presume decreased binding energies, particularly for the AA and AN binding motifs. Furthermore, for all binding motifs except AA polymerization is possible, *i.e.* the product of aggregation is still a reactive species, thus increasing the probability of finding these other binding motifs rather than AA. Note that, irrespective of the binding energies, the dimers shown in Table 1 and Figure 14 just indicate binding motifs that can be expected to be present in solution to some extent. However, to determine the prevalent species in the experiment, we compare the TD-DFT and the experimentally derived absorption peak shifts upon aggregate formation, see Figure 12, as detailed in the following.

In case of **D2A** virtually no aggregation-induced shift of the $S_0 \rightarrow S_1$ absorption energy can be observed experimentally, but slight-blue shifts are present in case of **D3A** (505 → 480 nm) and **D4A** (510 → 490 nm), respectively (see Figure 12, top). In contrast, the TD-DFT calculations yield red-shifted $S_0 \rightarrow S_1$ absorptions for AA-dimerization for all of the merocyanines (see Figure 12, bottom). Thus, the AA-binding motif appears not to be dominating in ground-state aggregate formation. In case of **D3A**, AN-binding involves a slight red-shift, too, what is again not in

accordance with the experimental blue shift. For the other two merocyanines AN-binding causes no spectral change, what fits the experimental observation exactly just in case of **D2A**.

Finally, the experimentally observed slight blue-shift of the $S_0 \rightarrow S_1$ absorption peak in case of **D3A** and **D4A** can just be reproduced when the π-bridge is involved in dimerization, *i.e.* in ANπ- and Aπ-type dimers. This $S_0 \rightarrow S_1$ absorption peak of the dimer does not shift further to the blue upon successive aggregate growth in case of ANπ-type binding, as shown by the comparison of the TD-DFT-derived absorption spectra of a **D3A**-hexamer with the dimer in Figure A 2 and Figure A 3 in the appendix. After the AA-binding motif, the ANπ-binding motif is energetically most favorable for all investigated merocyanines and the binding energy scales with the π-bridge lengths (**D2A**: 0.66 eV, **D3A**: 0.77 eV, **D4A**: 1.05 eV). However, the number of geometrical realizations of this binding motif is rather limited due to distinct interactions between the polar heads, while a larger number of realizations can be expected for the energetically little less favorable Aπ-dimers.

Since the position of the absorption peak is not affected by concentration changes of **D2A**, the blue-shifted ANπ- and Aπ-type dimers are not expected to dominate in case of **D2A** since the spectral changes due to their formation would need to be balanced by formation of AA-dimers. However, in case of **D2A** the rather concentration-independent $S_0 \rightarrow S_1$ absorption energy can be reproduced by various linear combinations of all the above discussed binding motifs.

Since all but the AA-type dimers allow for successive growth of aggregates, analysis of the aggregate size might further support the above deduced importance of ANπ- and Aπ-binding in case of **D3A** and **D4A**. Such analysis of partical sizes, as investigated by means of dynamic light scattering (DLS) studies, reveal that **D4A** forms large aggregates in chloroform (1.5 mM) with a mean diameter of 70 nm as shown in Figure A 4 in the appendix. Also in case of **D3A** the particle size systematically increases from 1.5 nm (monomers) to 1.9 nm (dimers) to 2.0 nm (dimers and higher aggregates) at raising concentrations (0.2, 1, 2 mM, respectively) as revealed by the DLS-results shown in Figure 15. Additionally, the DLS-results indicate the presence of aggregate sizes between 6 and 8 nm, which we assign to a different principal axis of the before-mentioned aggregates rather than to an independent distribution. These aggregates grow further with time and finally formed a gel within few days from THF- and chlorobenzene-solutions of **D3A**, as shown by the photograph in Figure 15. To ensure the van der Waals nature of the formed aggregates their dissolution was investigate by means of DLS as well. The DLS-data in Figure 5 of the SI show dissolution of aggregates (solid state powder) by a polar and protic solvent, such as methanole. Polar and protic solvents are generally expected to efficiently suppress aggregate formation upon interaction with the polar sites of the merocyanines.

Finally, the analysis of our quantum chemical results, the experimental absorption spectra and DLS data reveal that the molecular shape determines the ground-state aggregation in the dark. While for **D3A** and **D4A** the ANπ and Aπ binding motifs, which allow for successive aggregation, prevail, a dominant binding motif could not be unambiguously determined for **D2A**, where either AN dominates or many differently bound dimers are formed, which do not cause a net spectral absorption shift.

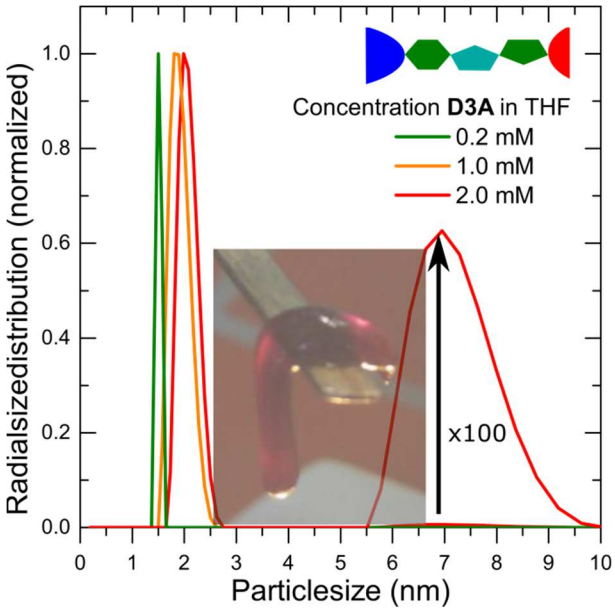

Figure 15: Particle size distributions at different concentrations of **D3A** in tetrahydrofuran as determined by means of dynamic light scattering measurements. Since spherical particles are usually assumed the particle size is the diameter of the single particles. In the inset a jelly worm made from D3A in THF-d_6 is shown.

Excited State Aggregation

In stark contrast to the changes in absorption spectra upon increasing the dye concentration, irradiating the solutions of all investigated merocyanines causes strong changes in the absorption spectra: The $S_0 \rightarrow S_1$ absorption peaks vanish, while peaks close to those assigned above to $S_0 \rightarrow S_2$ transitions evolve and give rise to isosbestic points in each case, as shown in Figure 12. This type of absorption change is known for the formation of H-aggregates in non-polar media, where aggregation is driven by the energetically favorable compensation of dipole moments[130, 139]. However, such ground-state aggregation might be hampered due to the bulky substituents[129, 130] that are present in the here investigated merocyanines.

To understand why the typical H-aggregation absorption changes are observed when irradiating the solutions but not when increasing the merocyanine's concentration, we consider the (TD)-DFT-derived molecular dipole moments of ground and excited states in the following. According to these (TD)-DFT calculations, the S_1 exited states have significantly larger dipole moments μ (μ_{S1}(**D2A**, **D3A**, **D4A**)=21.8, 29.8, 26.3 D) as compared to the S_0 electronic ground states (μ_{S0}(**D2A**, **D3A**, **D4A**)=9.1, 9.1, 10.5 D). Thus, the driving force for compensation of the dipole moments due to dimerization if significantly enhanced upon photoexcitation for a given solvent and presumably causes geometry adaptions to overcome steric hindrances of the triaryl-amines.

Naturally, most of the energetically favorable dimers feature S_0 dipole moments smaller than the ones of the individual monomers, as shown in Table 1. The latter are on average best compensated in AA, followed by Aπ, AN, ANπ binding motifs, if all three merocyanine derivatives are considered. This trend in dipole moment compensation is reflected in the angles between the dipole moments of the dimer-composing monomers (see Table 1). These angles are deduced from the molecular orientations presuming the dipole-moments fixed to the molecular coordinates.

Importantly, the dimer dipole moment is small at photo-excitation ($\mu_{dim\text{-}S1}$) just for the AA-binding motif, while large dipole moments (up to 37 D as shown in Table 1) are obtained for the other binding motives, particularly the ones allowing for step-growth of aggregates. Consequently, in case aggregates other than AA-bound types, including those having step-grown to larger sizes, molecular reorientation or aggregate dissociation might occur upon photoexcitation to compensate the large dipole moments in the excited states. This assumption is supported by the DLS-data shown in Figure A 4 of the appendix, which show a decrease in aggregate size upon irradiation.

Furthermore, the presences of the isosbestic points in the absorption spectra series detected with bias illumination, *cf.* Figure 12, indicates formation of distinct dimers. These dimers do not grow to large aggregates upon further irradiation because of compensating dipole moments. Consequently, this dimer formation mechanism and the resulting structures are entirely different from the above ground-state aggregation for all investigated merocyanines.

Kinetics of Excited State Aggregation

Changes in absorption spectra of dyes due to illumination might generally be caused by photo-degradation. To discriminate between photo-aggregation and -degradation we analyzed the kinetics of the absorption changes. While in case of photo-degradation basically a 1st-order kinetics would be expected, a 2nd order kinetics shall be found for dimerization. Plotting our data according to these orders (1st-order function $f_1=ln(E(t_0)/E(t))=kt$, 2nd-order function $f_2=1/E(t) - 1/E(t_0)=kt$; see Figure A 7in the appendix) reveals that the photo-induced changes in absorption spectra do clearly not follow a 1st order kinetics, *i.e*. degradation can be excluded as reason for the observed absorption changes as already indicated by the presence of isosbestic points in Figure 12, but a 2nd order kinetics also does not describe our data accurately in case of **D2A**, **D3A**, **D4A**. Here E(t) is the extinction after an illumination time of t, $E(t_0)$ is the extinction before starting the illumination experiment and k is a constant. For the example of **D4A** we tested for the order of the reaction by comparing reaction rates *r* for different starting concentrations and evaluated the extinctions *E* according $r = (E(t) - E(t_0))/t$ (see Appendix Figure A 8). When increasing the concentration from 7.7 mM to 30.8 mM corresponding to a factor of 4, the reaction rate increases by a factor of 12 for short illumination times and decrease to approx. 6 for long times, thus, again neither fitting to 1st or 2nd order kinetics.

Instead of simple 1st or 2nd order models, a stretched exponential model with the free monomer concentration decreasing exponentially as a power of time, *cf*. the work of Pasternack *et al*.[151] and Petrenko *et al*.[58], fits our data sufficiently for all investigated merocyanines as shown in Figure 16. In the applied stretched exponential function

$$E(t) = E(t_0) + \left(E(t_\infty) - E(t_0)\right) \cdot \left[1 - e^{-(kt)^n}\right] \tag{1.12}$$

$E(t)$, $E(t_0)$, $E(t_\infty)$ are the extinctions at a given wavelength at the variable time *t*, at the start t_0 and the end t_∞ of the experiment, respectively. *k* is the reaction rate constant, and *n* accounts for possible further growth of merocyanine assemblies as a power function of time. The fit was applied to the extinction spectra and to the significant component C2, which was determined by singular-value decomposition (SVD, see supporting information for details) and describes the

temporal spectral change. The kinetic parameter resulting from fitting the stretched exponential model to the C2-data derived from the SVD are in qualitative agreement to those obtain from fitting the model directly to the temporal evolution of the extinction coefficient spectra and are not discussed separately in the following.

In the stretched exponential model shown above, the exponent *n* describes if the aggregation occurs upon formation of aggregates from single molecules or small cluster (n<1) or if the aggregation happens by fusing bigger aggregates (n>1)[152]; *cf*. the initial work of Leyvraz[153] and the more recent papers of Pasternack *et al*.[151] and Petrenko and Dimitriev[58]. The rather small *n*-values reported in Table 1, indicate aggregation prevailingly proceeds through combination of monomers rather than larger aggregates. This is in line with the above discussed model of photo-induced dimerization without further aggregate growth.

While the rate constants *k* are similar for **D2A** and **D3A**, see Table 2, the rate constant for **D4A** is significantly greater. The larger rate constant of **D4A** as compared to **D2A** and **D3A** is attributed to the long π-bridge of **D4A** that enables ππ-binding for many different mutual molecular orientations and positions. Since additionally the sterically demanding aryl-amine moiety has a smaller geometric intra-molecular weight, the probability for low-energy barrier aggregation shall be higher in case of **D4A** as compared to **D2A** and **D3A**. The value of the parameter *n* is smaller than unity for all datasets, what indicates aggregation starting from single molecules[152], thus supporting the above proposed photo-induced dimerization mechanism.

Table 2: Paramaters obtained by fitting the stretched exponential model to the decay of monomer extinctions *E* (low-energy maximum as detailed in Figure 16) and to the C2-component, which describes the temporal spectral change and was derived from a singular-value decomposition (SVD). Additionally, the significance, as represented by the values in the S-vector of the SVD, of the three significant components (C1, C2, C3) determined for all merocyanine derivatives are given.

Molecule	c (mg/ml)	c (mM)	*S (C1,C2,C3)*	S^{norm} *(C1,C2,C3)*	*k(C2), k(E)* (min^{-1})	*n(C2), n(E)*
D2A	10	23.4	31.6, 11.0, 1.0	1.00, 0.35, 0.03	0.082, 0.073	0.89, 0.87
D3A	10	16.8	27.6, 4.8, 0.2	1.00, 0.17, 0.01	0.059, 0.062	0.95, 0.78
D4A	20	30.8	63.8, 7.5, 2.8	1.00, 0.12, 0.04	0.278, 0.332	0.68, 0.84
D4A	5	7.7	8.7, 1.6, 0.3	1.00, 0.18, 0.03	0.114, 0.139	0.91, 0.92

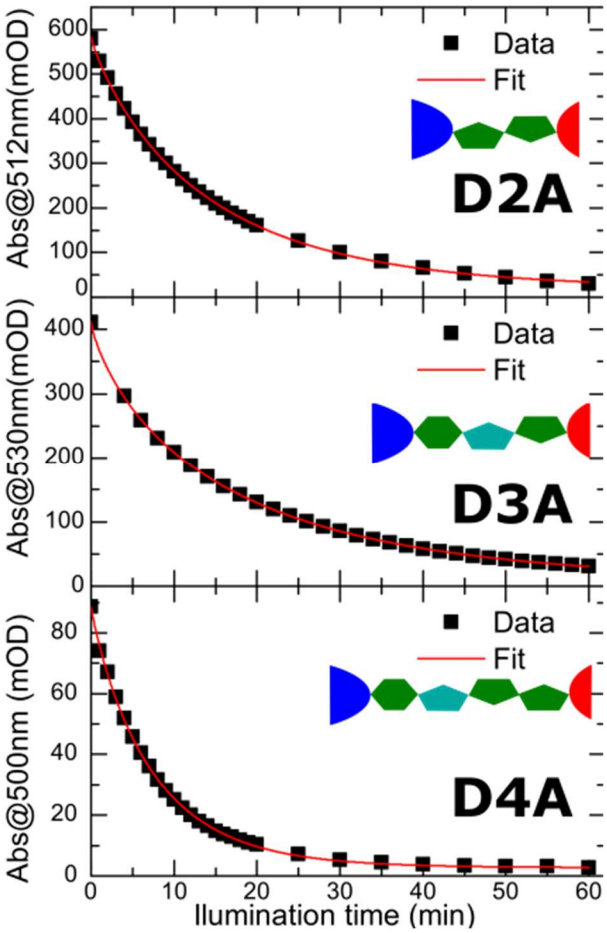

Figure 16: Changes of the extinction *E* with illumination time for the three merocyanines **D2A**, **D3A**, **D4A** (top to bottom) in chloroform (c=20 µg/ml) and line fits according the stretched exponential model.

3.3 Discussion on Reversibility and possible Degradation

However, when discussing photo-induced changes of absorption spectra or organic dyes, the possibility of photodegradation needs to be considered. Even if the presence of the isosbestic points in (virtually perfect for **D3A**, approximate for **D2A** and **D4A**) indicate single reaction products, *i.e.* the dimers, we tested for the reversibility of dimerization as well as checked for photo-induced absorption changes when aggregation is hampered.

The used solutions also show a change in absorption by storing the solutions in the dark, but on this can only be observed on timescales of several weeks to month. However, it turned out that the spectra change is much faster by treating them with high intensity irradiation. Since the final spectra of an illumination experiment shows a very similar spectral shape as found for solid state films further discussed in Chapter 4. Hence, we suspect to see a photo-dimerization or –aggregation. Furthermore, the extinction coefficient from the freshly prepared solutions changes with increasing concentration in a similar way as it does after illuminating the solution. A simple degradation or disassembly of the used dye molecules is also a possible explanation for the change in spectral shape. To distinguish between those two possible processes, we analyzed the

effect of concentration on the rates of the changes in the absorption spectra. We assume that a simple disassembly of the dye molecules should not depend on the concentration, if the number of absorbed photons is considered in the data analysis. The missing reversibility can also be a hind towards hydrogen bonded aggregates having a rather large binding energy as found from the DFT calculation (see Table 1).

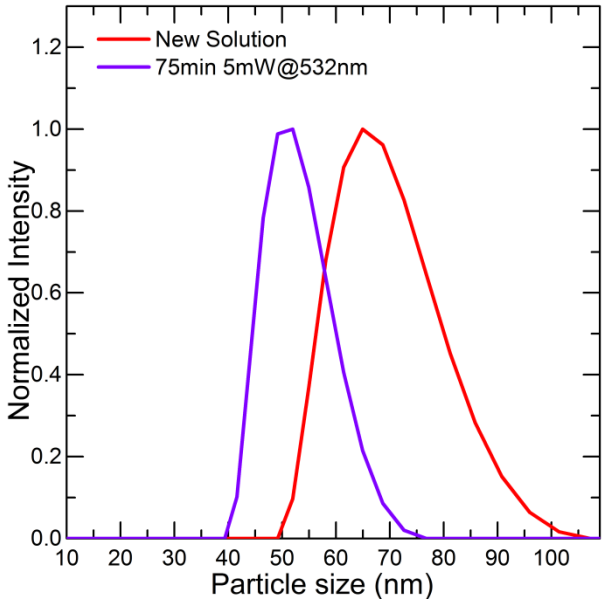

Figure 17: Particle size distributions at different concentrations of **D3A** in THF as determined by means of dynamic light scattering measurements. Particle size distribution of D4A in chloroform determined with DLS using a concentration of 0.5 mg/ml before and after illuminating the solution with a 532 nm laser.

Effects of environment on the photo aggregation

To further investigate the process of photo aggregation we altered the environment of the molecules. Our first idea was to change the acidity or basicity of the solution. Since we could not use water as solvent, we had to use acids and bases which are soluble in organic solvents. In this case, we used tetramethylguanidin(TMG) as a strong organic base and toluenesulfonic acid (TSA) to increase acidity. Furthermore we had to change the solvent from CF to dichloromethane to prevent the unwanted Reimer–Tiemann[14] reaction of CF with TMG, which could lead to the creation of the highly reactive dichlorocarbene.

By changing the acidity two distinct features changed in the observed absorption spectra. Beginning with the freshly prepared solutions, we found that the addition of TSA gives a red shift of the lowest energy transition. Furthermore, it raises the extinction coefficient of this transition in comparison to the pristine solution. By deprotonating of **D4A** with TMG we found a slight blue shift of the lowest energy transition and also the extinction coefficient of this transition is raised. The lowest energy transition alters its peak position from basic over neutral to acidic condition from 481 nm, 488 nm to 525 nm, respectively. From the absorbance of the pristine solution we also saw that in DCM and also slightly in CF that the first absorption peak is asymmetric. This implies that in pristine DCM not only one species is present. Rather a mixture of different monomers, dimers or different protonation states could be found which have slightly different

absorption wavelength. Since DCM is not a very good solvent for the used merocyanine dyes, most probably monomers and different dimers are found, which indeed fits very well to the differences in the calculated dimer absorptions in Figure 12. By illuminating the samples for 30 minutes we found that the deprotonated molecule monomer signal was completely gone, while the monomer signal in pristine DCM was not completely quenched. The protonated form was found to be the most stable monomer. This could be understood by means of the blocking of sights for hydrogen bonded dimers.

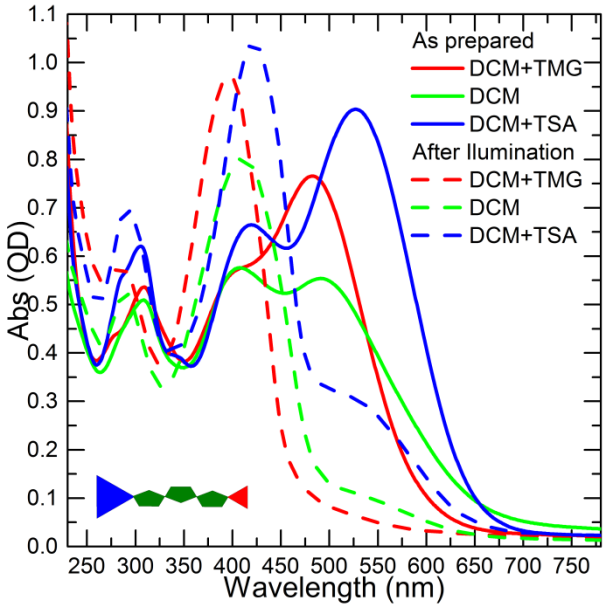

Figure 18 Effect of protonation and deprotonation on the aggregation of **D4A** in DCM. By protonating the molecule prior illumination we found that the photo-kinetics to be reduced.

Since aggregation is a very common issue for DSSCs[31, 32, 39, 42] limiting the performance of the solar cells, aggregation inhibitors[57, 71, 154] could be used to prevent aggregation. Desoxycholic acid is one of this aggregation inhibitors and its structure is shown in the left panel of Figure 19.

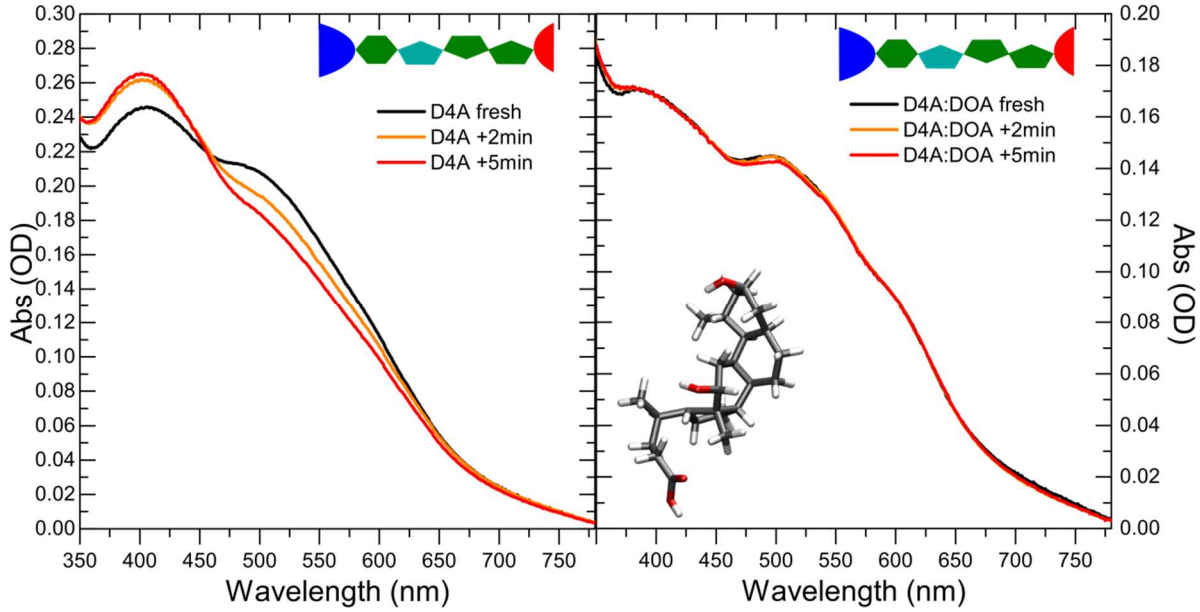

Figure 19 Effect of deoxycholic acid (DOA, shown in the right panel) on the Photoreaction of **D4A** drop casted on glass. DOA was implemented 1:1 by weight and shows a very good stabilization of the drop casted film of **D4A**. As DOA is commonly used as an aggregation inhibitor, we conclude that the reaction we see in solution and in thin films is due to aggregation rather than a degradation of the molecules.

Thin films produced by drop casting using **D4A** blended with DOA in a 1:1 mass ratio shows a significant stabilization upon illumination as shown in Figure 19. Here the absorbance spectra of the DOA blended **D4A** drop casted film is stable upon illumination, while the DC film of pristine **D4A** shows a significant reduction of the monomeric peak. What is also visible is the general decrease in absorption of the low energy peak by going from solution to solid state films. This is a further hind towards the formation of aggregates rather than simple disassembly of molecules upon photoexcitation.

To conclude this, there seem to be a ground state aggregation in solution and furthermore a much faster aggregation by illuminating the samples. The ground state aggregation leads to a decrease in the extinction of the $S_0 \rightarrow S_1$ transition of the respective molecules of approx. 20 % and less, while the photo-aggregation leads to a decrease of the respective extinction by more than 80 %. The photo dimerization seems to be non-reversible. Hence the photo generated dimers have a very high binding energy. This can be due to strong hydrogen bonding also found by theory. These dimers have binding energies exceeding 50 kJ/mol (0.6 eV) and are once build hard to break. Another possibility, which could not completely be excluded, is the building of new covalent bonds between two molecules. Also a disassembly of single molecules on an unknown route, which most probably needs two adjacent molecules, is possible.

3.4 Conclusion of Aggregation and Photoaggregation of Merocyanines in Solution

We have investigated the aggregation of three different merocyanines **D2A**, **D3A**, **D4A** that vary in the nature and length of their π-bridge. While the photonic properties and the aggregates of these derivatives are rather similar, the aggregation mechanism drastically changes when illuminating the merocyanine solutions.

In the dark, dimer structures are governed by interactions between the α-cyano carboxylic acid moieties and between the π-bridges. However, with increasing length of the π-bridge from **D2A** to **D4A** π-stacked aggregates become energetically more relevant. In contrast to dimers linked *via* the α-cyano carboxylic acid moieties, the π-stacked aggregates can continuously grow and finally prevail in the dark, as revealed by comparing experimental with TD-DFT-derived absorption spectra of specific dimer geometries.

While the absorption spectra of the considered dimers differ little, drastic changes in the absorption spectra, as known from H-aggregation, are observed when illuminating the merocyanine solutions. Because this systematic absorption changes feature isosbestic points we deduce that basically two distinct species are involved in photo-induced aggregation, which we assigned to monomer and dimer species. Since further growth of the dimers seems to be hampered, photo-aggregation apparently yields dimer structures that are distinctly different from those formed in the dark. The calculation of dipole moments of electronic ground and excited states reveal that the driving force for formation of dimers with compensating molecular dipole moments is drastically enhanced upon photo-excitation, thus presumably overcoming steric restrictions present in the ground state. Since the net-dipole moment of these dimers is close to zero, further growth according this photo-induced mechanism is not possible.

For sterically less hindered merocyanines concentration-induced dimer-formation due to compensation of dipole moments involving strong absorption changes with isosbestic points, very similar to the here reported photo-induced absorption changes, is well-known even for dark conditions. Consequently, the substitution pattern of the here investigated merocyanines are sufficient to avoid anti-parallel arrangement in the dark, what still can be provoked upon irradiation. In summary, our results show, that at processing of merocyanines with the here shown pattern or related chromophores the illumination needs to be carefully controlled to target supramolecular structures.

4 Aggregation of Merocyanine dyes in thin films

For the functionality of OPV and OLEDs, the intermolecular arrangement and morphology are one of the characteristics, which have a significant impact on all electronical and optical parameters of a device.[155, 156] The morphology mainly determines the position of energy levels[157], charge generation and recombination kinetics[158, 159] and therefore also the charge conductivity. The aim of this thesis is an in-depth investigation of model structures with controllable morphology, which were made by using the LB-technique. Those were obtained by using the Langmuir Blodgett technique[60]. To compare the results of the model structures with the commonly used films with isotropic or amorphous morphologies, drop(DC) and spin (SC) casting were used. These SC and DC-films were also post-treated by annealing to investigate whether similar structures as found by the LB-technique can be obtained. Using the findings of Chapter 3, it is possible to investigate the optical properties of the here-used merocyanines starting with single molecule over small aggregates in solution to highly ordered Langmuir-Blodgett thin films. To visualize the morphology, atomic force microscopy (AFM) was used and the absorption was measured using UV-vis transmission spectroscopy.

4.1 Langmuir Monolayer Characteristics at the Air-Water Interface

The here-used molecules shown in Figure 3 all have a hydrophobic chromophore and a hydrophilic carboxylate anchor group. Since the anchor group is relatively small in comparison to the hydrophobic chromophore, the molecules should not dissolve in water and should also assemble at the water-air interface of an LB-trough.

The LB-isotherms for **D4A** and **D3A** were measured on purified water with a pH value of approximately 5.5. In the case of **D2A**, a citric acid buffer was used to prevent deprotonation. Preliminary experiments revealed that the deprotonation causes an increased solubility of the molecule in water. The curves, shown in Figure 20, clearly show that both, **D4A** and **D3A** build up very stable monolayers while compressing them at the water surface. This can be concluded from the high surface presure that can be reached and the lack of a collapse point of the first monolayer. A surface pressure as high as 50 mN/m can be reached with only a slight change in curvature being visible at high surface pressures. Such a change in curvature can usually be considered to be an indication for a change in morphology[160]. A collapse of the first monolayer could only be observed in the case of **D2A** around a surface pressure of 20 mN/m. The space occupied by one molecule is smallest for **D4A** (A_0= 38 Å²), followed by **D2A** (A_0= 48 Å²) and **D3A**(approx. 50 Å²). This was determined by extrapolating the linear region of the isothermal curve to a surface pressure of 0 mN/m. The fact that **D4A** has a significantly lower A_0 was somehow not expected. It seems that for this molecule some aggregation occurs right in solution.

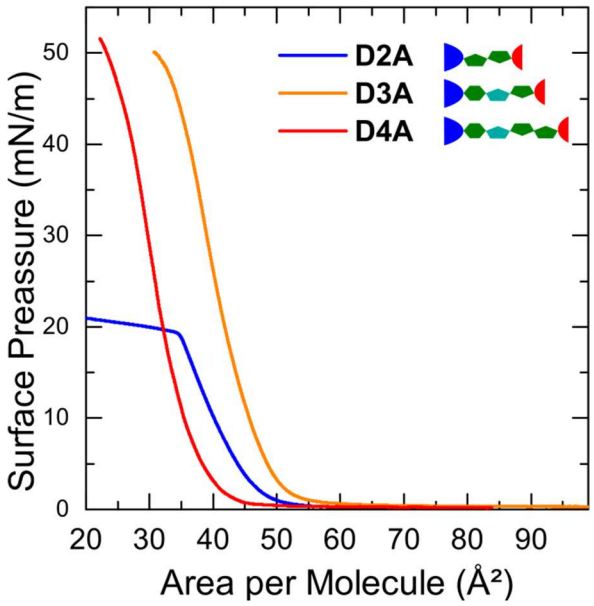

Figure 20 Isothermal curves on purified water of different pH values (see text) for the three dyes used in this study.

4.2 Morphologies of Thin Films

As proposed for the LB-technique[60, 63], smooth monolayer films can be obtained at low deposition surface pressures. In the case of layers made of **D4A**, these smooth layers were only found for low surface presures like 10 mN/m, but not for surface presures of 20 mN/m and above, as shown in Figure 3. In the upper pannel, the sample made with a surface presure of 10 mN/m is shown and there the phase image reveals large areas with a positive phase and roundish parts with a lower phase. Taking this into account, we see in the heigth image that the roundish parts are holes within the large flat area of the LB-film. These holes have a depth of approx. 2 nm, which is in the range of the length of the respective molecule. For higher surface pressures, a build-up of fibre-like structures could be observed. These fibres grow larger in size, length and diameter, and appear in a higher quantity, if the surface pressure is increased at the transfer process. All structures show a phase angle which is positive, indicating that the molecules are similarly aligned having the same part of the molecule on the surface. The relativeley long π bridge seems to promote centrosymetric round 2D structures, which tend to stack linearily in the third dimension. This fits to the ANπ type of aggregates described in Chapter 3. Hence, the round structure is caused by either the amphiphilisity of the molecule or the stable hydrogen bonds of adjacent molecules. The growth in the third dimension could also be caused by π-π stacking of different molecular dimers. The phase image reveals that only one moiety, most probably the lipophilic one, is on the surface of all structures. These assumptiones are based on the tendency of polar carboxylic hydrophobic head groups to bind to either other carboxylic groups *via* hydrogen bonding or to bind other polar moieties to reduce the repuslive lipophilic-hydrophilic interaction [161]

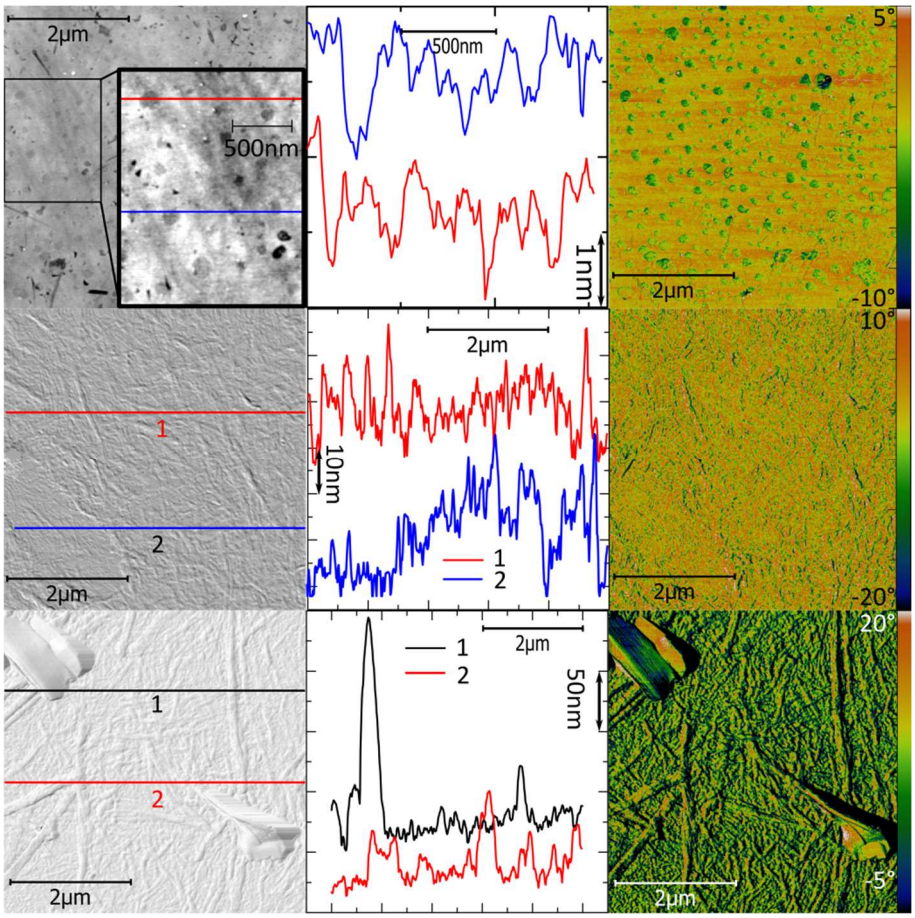

Figure 21 AFM height profiles (left) and phase images (right) of LB-films made of substance **D4A** at rising surface pressures (lowest to highest: top to bottom) and, hence assuming, rising crystallinity. The used surface pressures were 10, 20 and 40 mN/m, top to bottom, respectively. The scalling of the X-axisis is from 0 to 5µm for all pictures and graphs.

Since the effect of different morphologies is investigated in this thesis, fairly different morphologies were addressed in contrast to the ordered structures created by using the LB-technique. Therefore, thin films made by spin coating were prepared and investigated. Using this very common method to create thin solid films, we expect to see disordered amorphous structures and eventually small aggregates.[162] Furthermore, the samples could be post-treated by annealing to alter the morphology, which is a very common procedure in the production of organic solar cells. [27, 76, 163] By annealing, the thin film is heated to introduce vibrational energy into the system, which will give the possibility to escape local energetical minima in the given morphology. The needed temperature can either be the melting temperature or lower temperatures like the glass temperature, which enables polymers to reorganize their morphology. The film can then rearrange in a different, maybe more crystalline, way. By cooling the sample the new morphology is frozen.

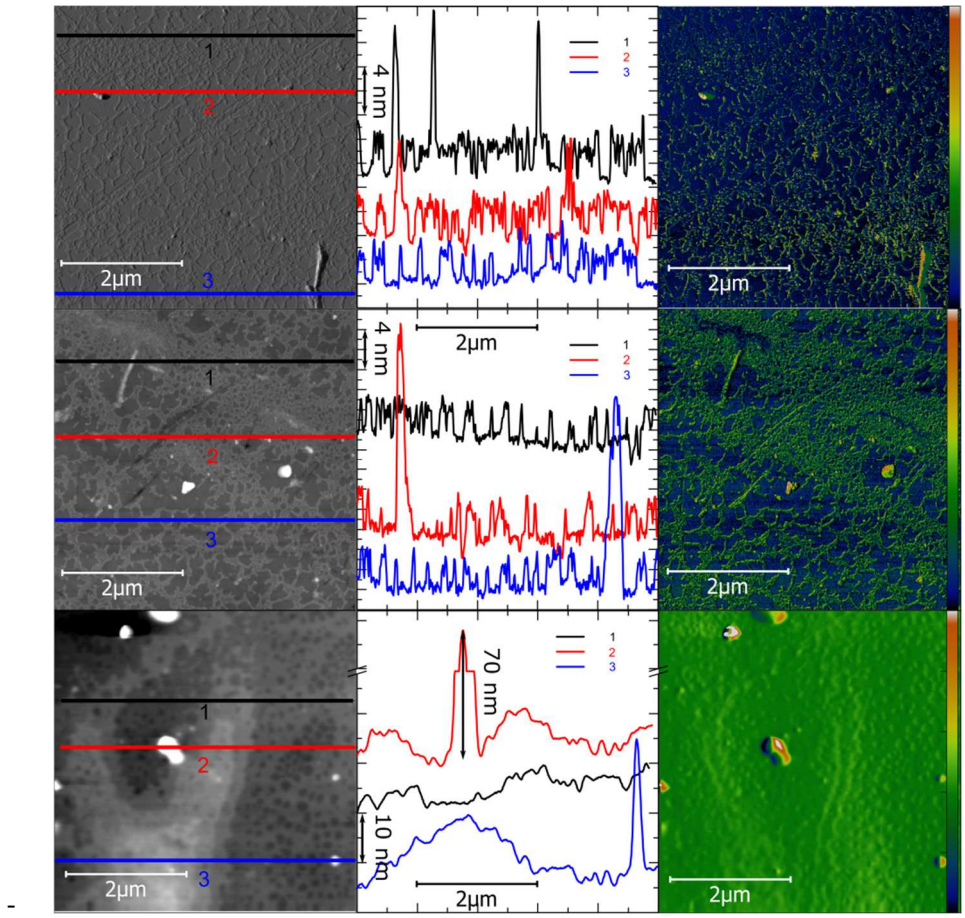

Figure 22 AFM height profiles (left) and phase images (right) of thin films made of substance **D4A** made by means of spin coating annealed at different temperatures. The temperatures are RT, 125°C and 245°C from top to bottom, respectively.

The surface morphologies of films made by spin coating using **D4A** on quarz glass show different morphologies, in comparrison to the films made by the LB-technique, as shown in Figure 22. A fine web-like structure can be seen for the as-cast film and the film that was annealed at a relativley low temperature of 125°C. Furthermore, few fibres can be seen which are also present in the LB films shown in Figure 21. For the highest used annealing temperature, *i.e.*, 245°C, a change in the morphology towards a flat smeared structure was observed. This can be attributed to a melting of the film.

From these morphology studies, we could assume that the local aggregate structure and hence the electronic properties should show more clearly pronounced features in the LB films rather than in spin-cast (SC) films. While there are more defined and similar structures found on one LB-film, the structures of the SC-films look more diverse and amorphous. But despite these differences, it turned out that the formation of fibre-like structures is found both for LB and SC films. Hence these structures are promoted by the structure of the molecule itself.

The morphologies of LB-films made of **D3A** is very different from the aforementioned **D4A**, while the molecule is very similar. This can be seen in Figure 23. In contrast to **D4A** this molecule tends to build flat structures for all surface pressures used. At the edges of these flat structures, we found terraces which have the height of approximately 4 nm. This height is approximately twice the length of a single molecule or the length of a hydrogen bonded head-to-head dimer like the AA one predicted in Chapter 3. Hence, the bilayer formation seems to be favorable, which might

be due to the high binding energy of the hydrogen bonded dimers. Also the energetical gain of π-π stacking should be reduced**,** due to a shorter π bridge in comparison to **D4A**.

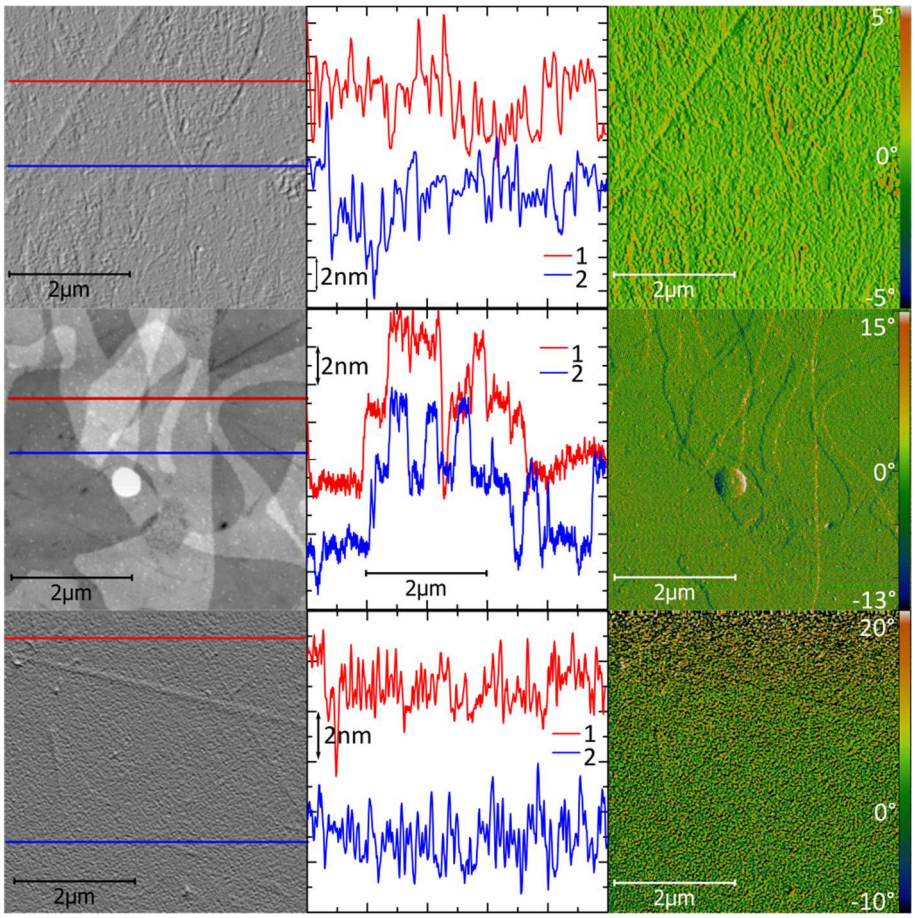

Figure 23 AFM height profiles (left) and phase images (right) of **D3A** deposited at different surface pressures. The used surface pressures were 10, 20 and 25 mN/m, top to bottom, respectively.

Especially in the sample dipped at a surface pressure of 20 mN/m the bilayer flake structure can be observed. Here every step of the multiple flakes on the substrate has a height of 4 nm. Using an even higher surface pressure like 25 mN/m the overall structure has no more flakes, but a flat surface built from round particles. These findings clearly illustrate that only minor changes to the molecule or the processing conditions drastically change the aggregation pattern of the molecule and hence the morphology of thin films. The phase image shows only small differences, hence just one side of the molecules is present on the surface, in the case of **D3A** and **D4A** this should be the lipophilic part. This attribution is based on the assumption that the silicon dioxide covered silicon AFM tip is usually OH-terminated and hence hydrophilic. The OH-termination is caused by the humidity of the air in which the tips are stored.

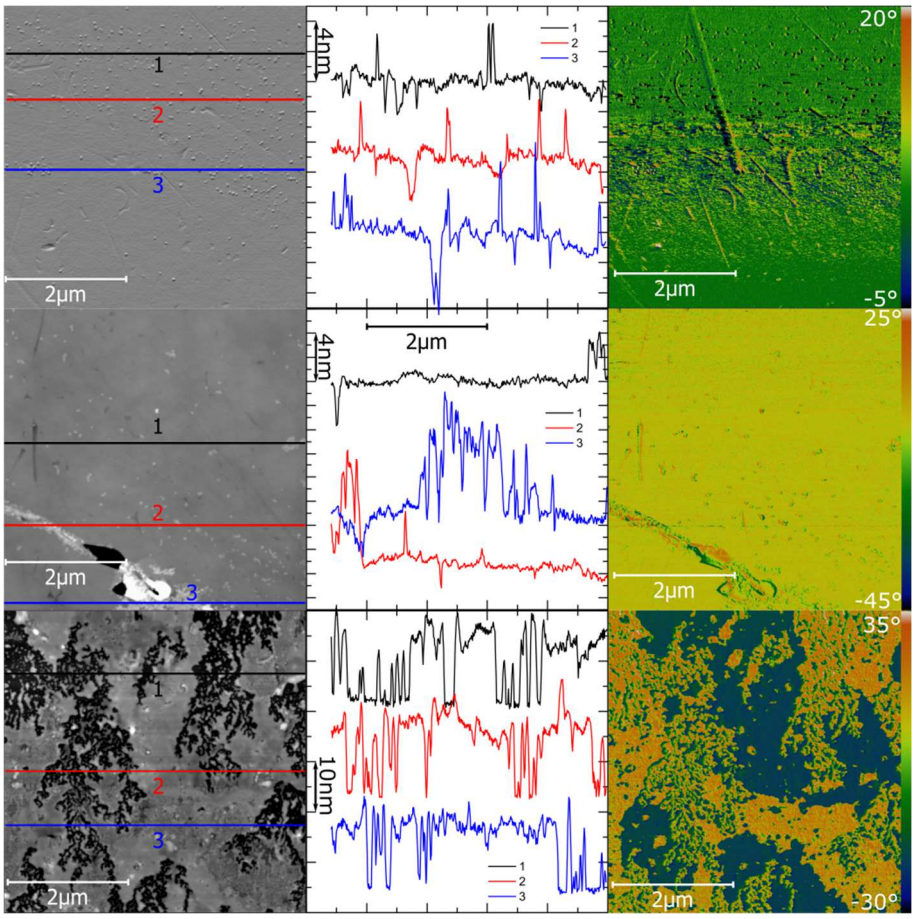

Figure 24 AFM images of **D2A** Langmuir-Blodgett films transferred at different surface pressures. The used surface pressures are 10, 15 and 20 mN/m, from top to bottom, respectively.

Height and phase images of **D2A** for different surface pressures are shown in Figure 24. For low surface pressures, *i.e.*, such pressures, which are below the collapse point of the first monolayer of approximately 20 mN/m, we obtained flat films with small clusters (30 nm in diameter and 4 or 8 nm in height). For surface pressures above the collapse point, **D2A** tends to form films with holes, which are approx. 12 nm deep. This corresponds to the height of six monolayers (ML), while from the transfer ratios only five would be expected for five up and five down strokes. Moreover, the high contrast in the phase image indicates that different moieties of **D2A** point upwards, resulting in two distinctly different tip sample interactions strengths. This is indeed surprising since we have expected a transfer of structures having either the hydrophilic or hydrophobic moiety on the surface, like it was found for **D3A** and **D4A**.

Hence, **D2A** seems to have a much-too-short hydrophobic chromophore to be stabilized at the water air interface. This can be concluded from the low collapse pressure of the isothermal curve shown in Figure 20, where a distinct kink can be seen at round about 20 mN/m. Using surface pressures close to the collapse point of the isothermal curve for the transfer to the solid substrate, several local morphologies can be obtained on the water surface. Hence, it is expected that the optical features obtained for LB-films of **D2A** made with a high surface pressure should be more similar to disordered amorphous films.

With these very similar molecules we could obtain fairly different morphologies in thin LB- and SC-films. It could also be shown that the morphology can be tuned by using different surface pressures during the LB transfer. With the LB-technique, it was possible to obtain distinctly different morphologies using the same molecule, but different surface pressures during the thin film transfer. Hence, the tuning of morphology by altering the transfer parameters of the LB-technique could be demonstrated for the here-used molecules. The range of available morphologies extends from needle-like structures of **D4A** to roundish flat structures of **D3A** and partially amorphous disordered structures for **D2A**. Since the obtained morphologies are very diverse, it is also expected that the absorption features should be different for samples produced with the LB-technique at different surface pressures. To investigate the absorption features, UV-vis absorption was measured on the thin film samples.

4.3 UV-vis Absorption of Thin Films

To get an insight into effects of different morphologies on the electro-optical properties of the molecules, first the optical absorption was measured with a standard UV-vis setup. The change in morphology or local crystallinity is often accompanied by changes in the absorption[6, 164, 165] or emission spectrum[123, 166, 167]. The most-discussed models are the J- and H-aggregates, which lead to either sharp bathochromically shifted (J-)[45, 168] or a relatively broad hypsochromically (H-) shifted peaks. A general overview about J- and H-aggregates with several examples can be found in the reviews of Würthner *et al.* [44, 169].

Using the cyanine dyes **D2A**, **D3A** and **D4A**, the picture of simple H- or J-Aggregation might not be applicable, since even the aggregation in solution does not show simple H- and J-aggregation features, like already shown in Chapter 3. From the solution experiments and dimer search by theory, it seems that especially hydrogen bonds play a major role for the intermolecular interaction. Thin films of organic dyes and polymers usually show a much more diverse inter-molecular arrangement within one sample. This is usually summarized in the term morphology[170]. In the following section the influence of the different morphologies on the UV-vis absorption of thin films is shown.

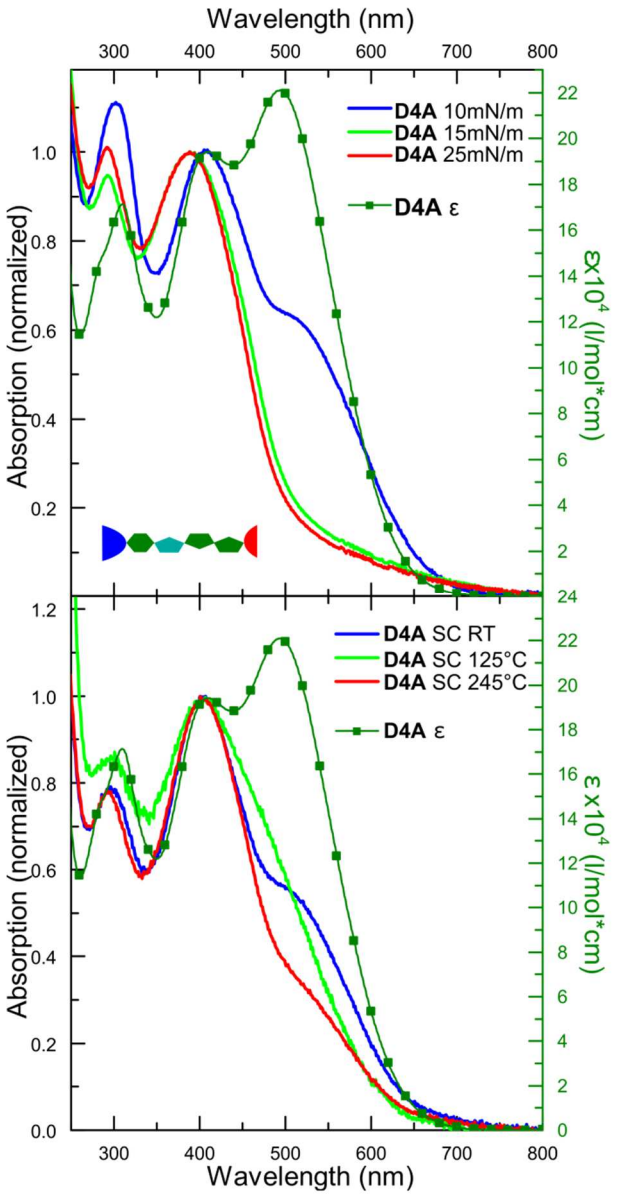

Figure 25 Comparison of the normalized absorption of LB-films and annealed spin-cast films for **D4A**. This material shows a significant effect of the compression on the absorption curve. The 500 nm peak almost completely vanishes for surface pressures above 10 mN/m. A similar behavior is found for spin-cast (SC) films. However, even after annealing, the 500 nm peak did not vanish completely and the spectral features are much broader.

The absorption spectra of the LB-films transferred at different surface pressures are shown in the upper panel of Figure 25. With increased surface pressure, the 500 nm monomer peak is firstly reduced to a shoulder at 10 mN/m and nearly vanishes above 15 mN/m. The second peak at around 400nm slightly shifts to the blue by around 150 meV. In the absorption spectra of CF solution of **D4A**, we find three prominent peaks at 500, 400 and 300 nm and a shoulder at around 290 nm. Since small peak shifts can be caused by *e.g.* protonation or deprotonation it was evaluated if that might be the reason in this case. Menzel *et al.*[71] reported a blue-shift due to deprotonation that amounts to approximately 300 meV and only affects the peak centered at around 500 nm, which is in contrast to our finding for the peak shift of 150 meV. In THF solutions, we see enhanced absorption at 400 nm and decreased absorption at 500 nm as compared to the measurements performed by Menzel *et al.*[71] We assign the low-energy peak at

500 nm to monomers and the 400nm peak to aggregated molecules, as already discussed in Chapter 3.

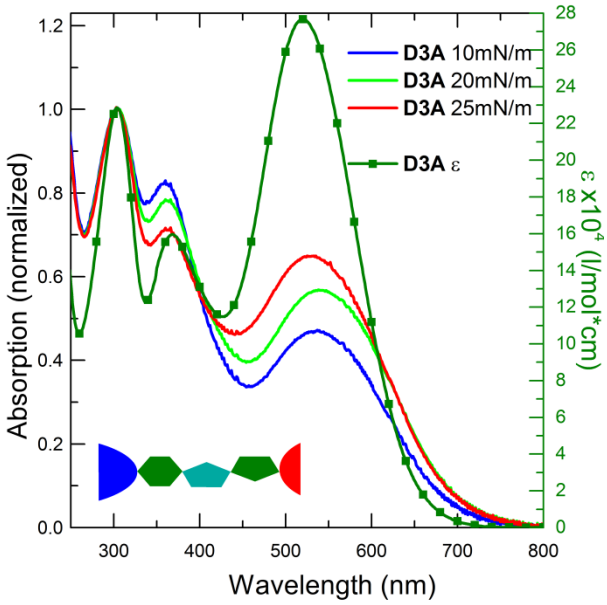

Figure 26 Comparison of normalized LB-thin film absorption and absorbance measured for a solution with CF of **D3A**. The thin films show a shift of the relative peak intensities from the lower energy transitions to the transitions with higher photon energy. Furthermore, there are slight shifts in the peak positions.

For molecule **D3A**, the lowest energy transition decreases in intensity by changing from solution to the solid state. For **D3A** the oscillator strength is transferred from the second absorption peak around 360 nm to the lowest energy peak at 520 nm. In contrast to the behavior of **D4A** the intensity transfer is not rising with rising surface pressure. Comparing with the local morphology of **D3A** obtained by AFM, we could conclude that some bilayer and flat structures seem to correspond to local intramolecular structures that have a lower intensity of the monomeric transition at 520 nm. By increasing the surface pressure at the deposition of our samples, the local structure seems to be similar, but more amorphous regions were created. These amorphous local structures show absorption features, which are more like the transitions observed in monomers in solution.

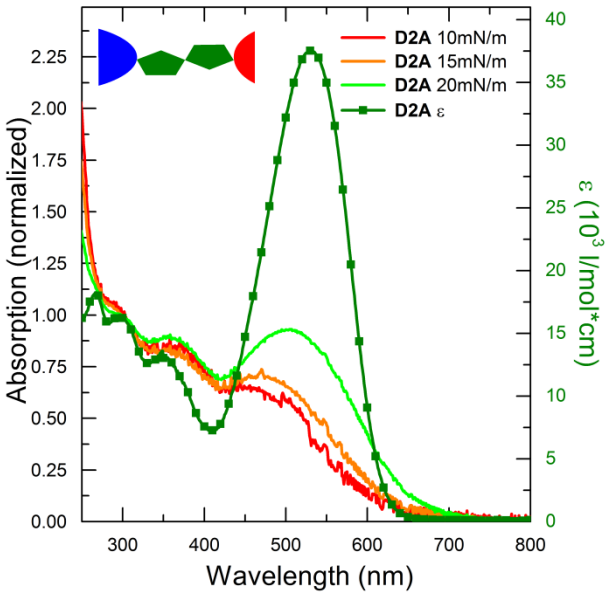

Figure 27 Comparison of LB-thin film absorption and absorbance measured for a solution of **D2A** in CF. All thin films show the same absorption features with a monotonous increment of the absorption peak around 520 nm with higher compressions.

For the short molecule **D2A**, only one significant difference of the absorption spectrum between solution and highly ordered LB-films could be observed. The spectral feature, which is mainly influenced by the morphology, is the low energy absorption peak at round about 520 nm. In comparison to the solution case this peak shows a much lower absorption in comparison to the peaks at 300 nm and 350 nm, respectively. Furthermore, this peak slightly shifts to the blue for films transferred at low surface pressures. . In contrast to the behavior found for **D4A**, but similar to **D3A,** the lowest energy transition gains oscillator strength with higher surface pressures. This correlates to the microscopic picture obtained using AFM as seen in Figure 24. For the samples transferred at low surface pressure, we saw flat films and small round particles, which should all have some kind of crystalline structure. Deposition of **D2A** at 20mN/m results in films with different local morphologies and also disordered amorphous regions. This was expected due to the breakdown of the first monolayer on the water surface at this surface pressure (*vide supra*). Hence, the molecules have less electronical interaction for samples transferred at very high surface pressures as compared to the low surface pressure samples mentioned above. This assumption is supported by an optical absorption, which is more similar to the monomeric or solution case, than that of the more ordered LB-films transferred at medium surface pressures.

For all investigated molecules, the lowest energy transition is strongly affected by the transition from the solution case to the solid state. Furthermore, the different forced morphologies give very different changes in the optical absorption. In general, the loss in absorption at the low energy transition is a major drawback for the use of these molecules in organic solar cells as well as for DSSCs, since this obviously strongly limits the maximum photocurrent generated in the device.

Despite the loss of absorption in the green to red spectral region, aggregation also heavily influences the photo-physical processes[33, 171] and charge conductivity[172]. In particular an increased number and density of different recombination channels can further decrease the

efficiency of DSSCs and organic solar cells. On the other hand a higher electronic coupling between adjacent molecules can increase the conductivity and hence the overall organic solar cell efficiency[173]. To get a deeper insight into these processes, we performed fluorescence and femtosecond transient absorption spectroscopy. This will be discussed in the following chapter.

5 Photoinduced Dynamics in Solution and thin films

As shown in the previous chapter we see a distinct variation of the optical absorption by changing the local morphology from single molecules in solution to aggregates in solution, and finally ending with highly ordered LB-films. To get deeper insight into the processes right after photo-excitation of the molecules and how these processes change in dependence of the aggregation, we performed fluorescence and femtosecond transient absorption measurements. To get a basic idea about the part of excited molecules that undergo fast recombination, fluorescence spectroscopy and the calculation of fluorescence quantum yields (Φ) are used. The latter will allow estimation on how fast deactivations processes are in comparison to the emission. Since fluorescence usually has time constants in the range of approx. 1 ns to a few nanoseconds, the ultrafast recombination can only be measured in the femtosecond to few nanoseconds time regime. Consequently fs-TA spectroscopy was applied to further investigate the ultrafast kinetics right after photoexcitation.

In this chapter the shortest molecule will not be considered in depth, due to the very much limited amount of substance available for this work. The fluorescence is already shown in Figure 11, while the transient absorption data and their description can be found in the appendix.

5.1 Fluorescence and Fluorescence Quantum Yields

As has previously been reported in the literature, both **D4A** and **D3A** show very weak fluorescence in chloroform (CF), which, in fact, could not be measured using the standard fluorescence spectrometer in the organic chemistry group, where the dyes were sysnthesized.[71] Fluorescence in CF shows a huge Stokes shift as illustrated in Figure 11. The Stokes shift is increasing with an increasing length of the π-bridge and amounts to 420 meV (3388 cm^{-1}), 640 meV (5162 cm^{-1}) and 790 meV (6372 cm^{-1}) for **D2A**, **D3A** and **D4A**, respectively. This indicates a strong geometrical relaxation after photoexcitation. Since a change in the molar extinction coefficient upon increasing the concentration was already observed, the changes in fluorescence spectra and fluorescence quantum yield (Φ) of **D3A** and **D4A** in CF solution were also investigated in dependence on the concentration. The fluorescence intensity normalized to the absorbed photon flux is shown in Figure 29. Here it can be seen that the spectra only slightly change upon increasing the concentration. While the overall intensity drops, there is a minor shift in the emission maximum to the red. This concentration dependent shift is less pronounced for **D4A** for both excitation wavelengths. For **D3A** the shift is weak, if the molecule is excited to the S_1 state at 532 nm, but it is rather strong if the molecule is excited at 405 nm. By using these spectra the fluorescence quantum yield Φ was calculated by integrating the corrected and normalized fluorescence spectra from 550 to 1000 nm. These corrected spectra were than used to calculate Φ applying formula 2.9 from Chapter 2.3.[97]

From the determined Φ values, shown in Figure 28, we were able to extract two facts. Firstly the Φ drops drastically by increasing the concentration. To calculate if the reabsorption has a significant effect on the Φ one could simply use the following formula:

$$\frac{\Delta\Phi}{\Phi} = \frac{\int_{\lambda_0}^{\lambda_E} I_F(\lambda)d\lambda - \int_{\lambda_0}^{\lambda_E} I_F(\lambda)\cdot 10^{-E(\lambda)}d\lambda}{\int_{\lambda_0}^{\lambda_E} I_F(\lambda)d\lambda} \tag{2.1}$$

Where I_F is the measured fluorescence intensity, E is the extinction and 10^{-E} is the transmission from the excitation spot to the end of the cuvette. Φ is the relative fluorescence quantum yield with ΔΦ being the difference in quantum yield due to reabsorption. The case were the reabsorption has the highest impact is the highest concentration of the molecule with the lowest stokes shift, *e.g.* **D3A** with 10 mg/ml. Using this formula for this case, it was found that the relative change in the determined fluorescent quantum yield ($\frac{\Delta\Phi}{\Phi}$) is approx. 0.39%, which is clearly negligible.

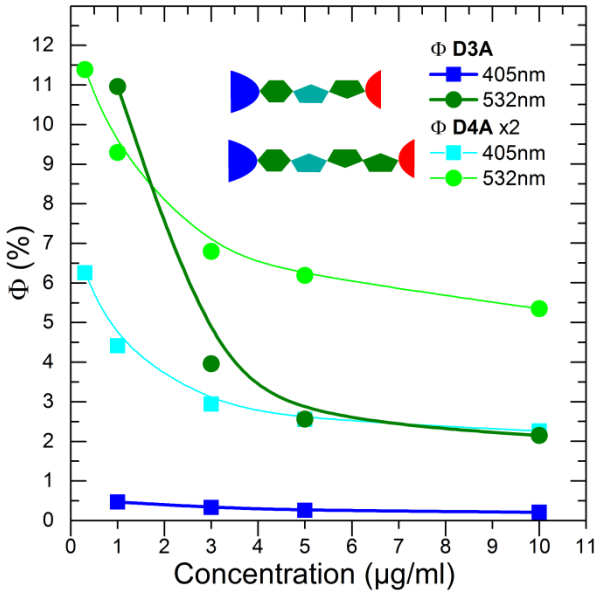

Figure 28 Fluorescence quantum efficiencies (Φ) of **D3A** and **D4A** in CF determined at different excitation wavelengths and concentrations

Secondly Φ differs by a factor of two by changing the excitation from 532 nm to 405 nm in the case of **D4A** and further by a factor of ten in the case of **D3A** as shown in Figure 28. This means that a big part of excited molecules relaxes to the ground state *via* efficient dark recombination channels. These might be introduced by concentration due to self-quenching[75] or much lower fluorescence yield in dimers or aggregates[174, 175]. If we address higher excited state or dimeric state by choosing 405 nm as excitation wavelength, we also observe a drastic drop in quantum yield. This means that there is an ultrafast deactivation channel between the S_2/D_1 state and the fluorescing S_1 state. Here S_1 and S_2 are the first and second excited singlet state, while D_1 is the first excited dimeric or aggregate state. This channel somehow is able to compete with, or is even more probable in the case of **D3A**, the internal conversion from S_2/D_1 to S_1. The energetic difference between S_1 and S_2/D_1 is fairly different between **D3A** and **D4A**. For **D4A** this energetically difference is approx. 0.7 eV, on contrast to approx. 1.15 eV in the case of **D3A**.

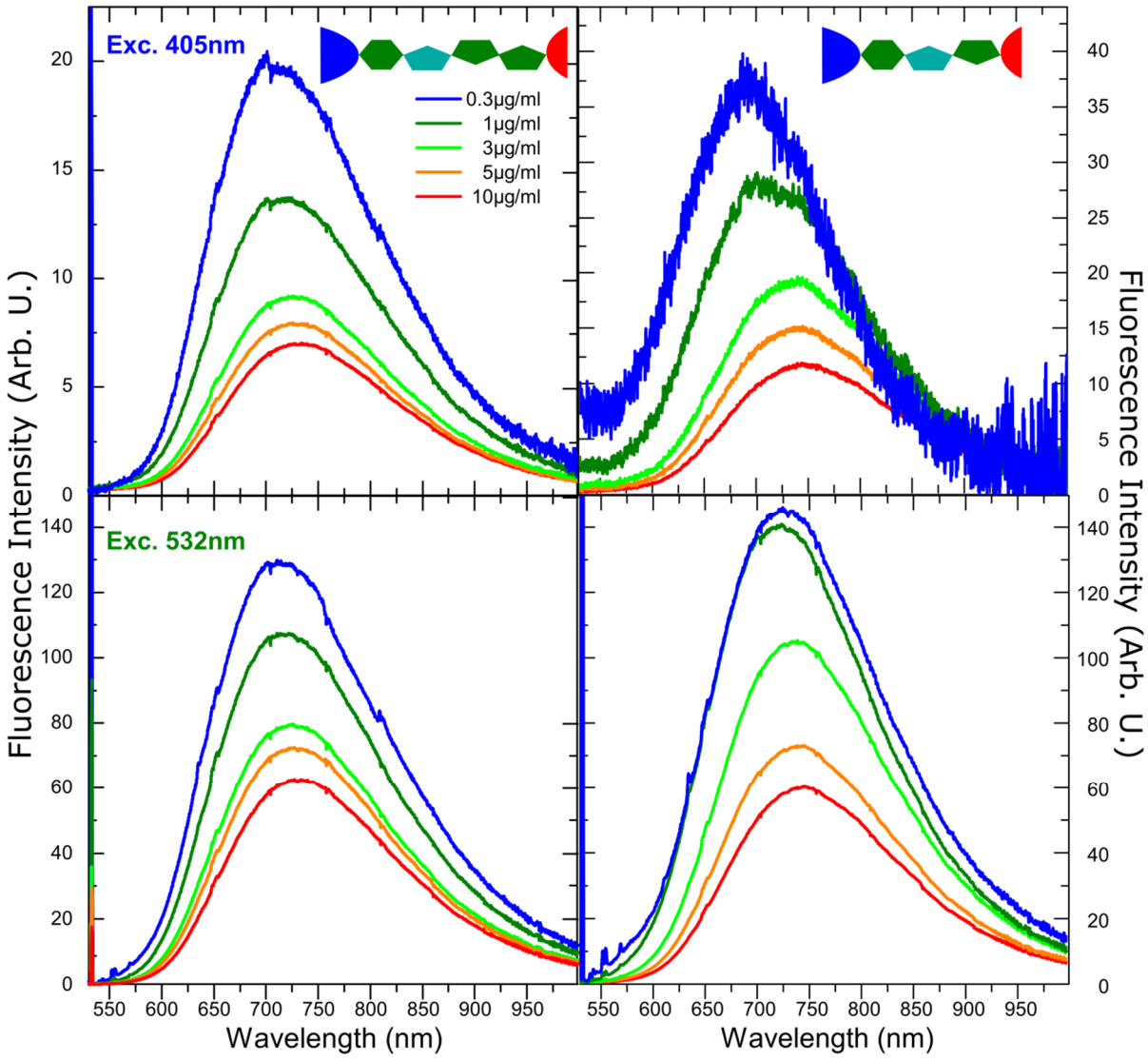

Figure 29 Concentration dependent fluorescence spectra of **D3A** (right column) and **D4A** (left column) measured in CF. The top row represents the spectra measured with an excitation wavelength of 405nm and the lower row is measured using 532nm as excitation. The emission is normalized with respect to the number of absorbed photons, hence the area is proportional to the fluorescence quantu7m yield.

Despite energetically lower lying dimeric states, different geometries of the different excited singlet states could also be a reason for the hindered transition from higher excited states to the fluorescing S_1 state[176]. The overall very low quantum efficiency indicates very fast non-fluorescent recombination channels. In order to verify or falsify the existence of such ultrafast recombination channels, transient absorption measurements were performed. To evaluate the nature of the emissive state, we performed time-dependent measurements on **D4A** in CF, which reveal the fluorescence-character of the luminescence with double exponential decay of τ=0.6 and τ=2.5 ns in CF, respectively (see Appendix Figure A 14).

By changing from solution to solid state films we were not able to measure any fluorescence from solid state thin film samples, meaning that in solid state all excited molecules non-radiatively decay to the ground state *via* most probably fast recombination channels[36]. These channels will be introduced by a high number of available electronic states in close proximity in an aggregate.[177] With the high number of energetically similar states, the excitation in an

aggregate can use several small energy steps to reach the ground state, which is possible by emitting phonons or vibrations. These recombination pathways are much faster than emitting one big portion of energy by *e.g.* a photon *via* fluorescence.[75] The recombination in *via* states located within the band gap of organic semiconductors is well established. The recombination is usually referred to tail states, where the density of energy levels in a disordered organic semiconductor is exponentially distributed below the band gap.[136, 178-180] With a higher number of efficient non-radiative decay channels not only fluorescence is quenched, the overall efficiency of DSSCs or organic solar cells should also decrease. This is in line with the reduced efficiency for DSSCs made with and w/o an aggregation inhibitor mentioned by Menzel *et al.*[71]

5.2 Excited State Dynamics of Solution and Thin Films

Transient absorption spectroscopy will now give the oportunity to take a closer look into the early processes after photoexcitation. These meassurements were performed first in solution and afterwards in solid state samples to quantifiy the differences in the ultrafast processes due to the presence of solvent molecules or different aggregates. In this study the aim is to understand the effects of aggregation on the ultrafast processes in the here used molecules and their effect on the efficiency of charge generation and recombination of dyes attached to the TiO_x surface[181-183]. In this work the focus will be on the difference between the kinetics of molecules in solution and in different solid states.

As solid states samples we used films with increasing aggregation or crystalinity, namely for spin casted, drop casted and LB-films, respectivley. For a comparison of the data spectral traces and kinetics are shown in the following figures, the decay associated spectra can be found in the appendix. For a better discrimination and classification of the ultrafast processes of **D3A** and **D4A** molecule in solution, we used DMSO and CF, which have a fairly different polarity. Due to the higher polarity of DMSO it should stabilize intramolecular charge transfer right after photoexcitation[75] of this donor-acceptor type molecules. Transient absorption (TA) spectra were recorded at two different excitation wavelengths. We chose 530 nm and 404 nm to pump the first, *i.e.*, the low-energy transitions and the second transitions, respectively. These two wavelengths were also chosen, because we used the same to determine the fluorescence quantum yields. Hence we can directly observe the kinetics, which lead to the dark recombination found by changing the excitation wavelength in the previous section.

For some spectra a SVD analysis was used to find components, which do not solely show an exponential decay. This might especially be useful for transient absorption data, where many spectrally overlapping components seem to be present, which show fairly difficult kinetics.[184] For some spectral features a peak fit by a self-written Labview program was performed. This gives the possibility to clearly distinguish between spectral shift and decay of specific features in the spectra.

In general, we would assume to see three different features in the TA-data: Ground state bleach (GSB), stimulated emission (SE) and excited state absorption (ESA)[104]. The GSB is caused by the reduction of the number of molecules in the ground state upon photo-excitation

Stability of the Molecules during the Transient Absorption Measurements

As it was found that the molecules show a significant change in their absorbance upon illumination, it had first to be checked if the data obtained with fs-TA spectroscopy are completely valid. In this respect it was found that, if the absorbance changes, the fs-TA spectral and kinetic traces significantly change. The comparison of the spectral and kinetic traces of a measurement of **D4A** in CF, before and after photo-aggregation is shown in Figure 30. To compare the transient absorption spectra with and without photo-aggregation we should focus on different transient absorption features: The GSB region of the monomer and aggregate at approx. 500 nm and approx. 400 nm, respectively and the ESA features at 575 and 730 nm. For the fresh solution we see a significant GSB signal at 500 nm, which is decaying slowly within the first few hundreds of ps. In contrast to this the photo-aggregated solution only shows a weak GSB signal at 500 nm which decays within approx. 1 ps. The ESA feature at 575 nm is present in both solutions but more pronounced in the photo-aggregated solution and also shows similar kinetics. The ESA feature at approx. 650nm is visible as shoulder in the fresh solution but as dominating ESA feature in the photo-aggregated solution. The respective kinetic traces at 650 and 700 nm are also similar in both cases, despite a much less pronounced buildup of TA signal in the photo-aggregated case in contrast to the fresh solution.

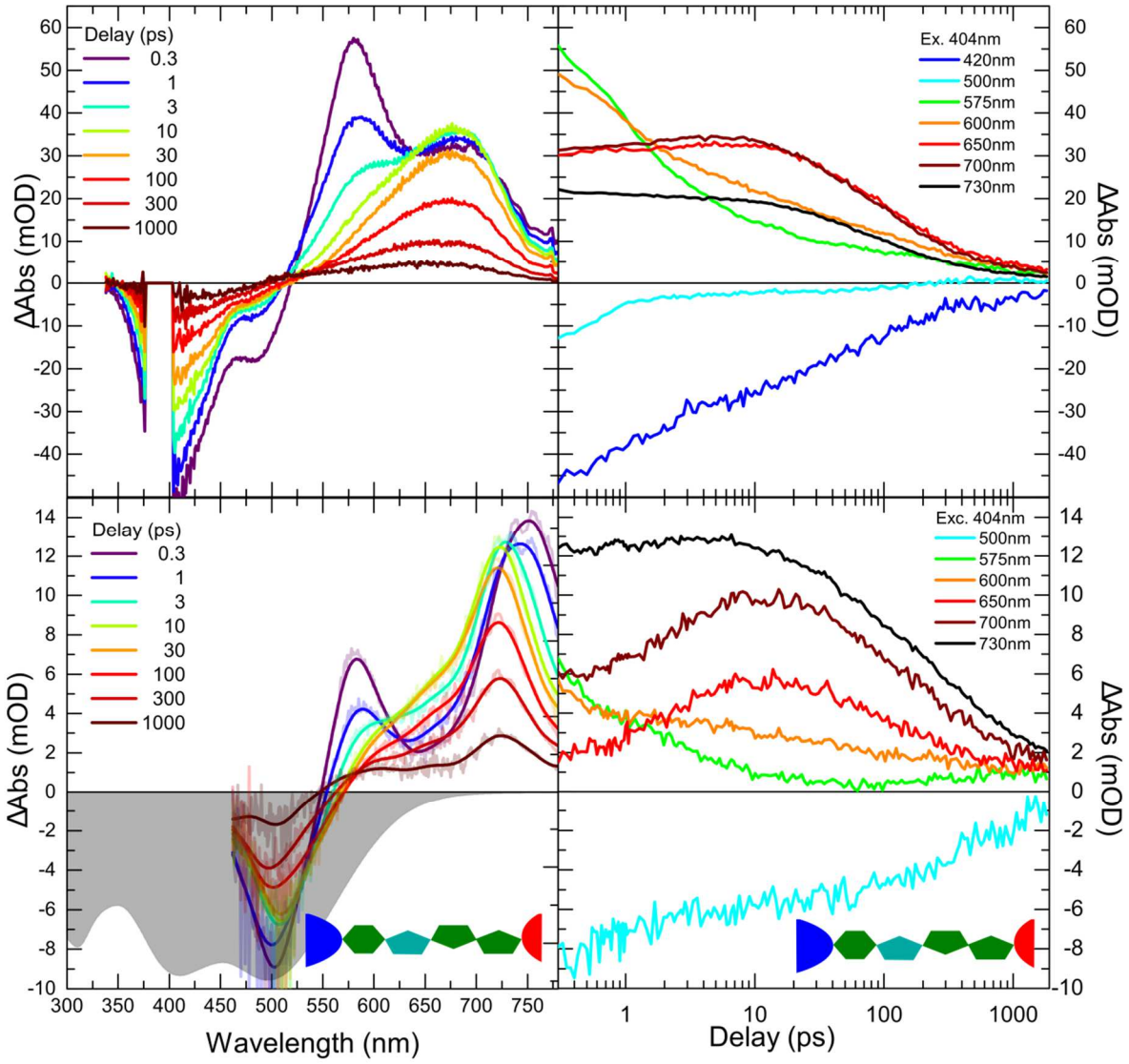

Figure 30 Spectral (left) and kinetic (right) traces of a photo-aggregated (top) and a freshly prepared (bottom) solution of **D4A** in CF. While the measurement in the upper panel shows drastically changes of the absorbance during the measurements, especially seen in the GSB region around 500 nm. The older measurement shown in the lower panel shows other features and a GSB which corresponds clearly to the absorbance measured for a fresh solution.

Especially the GSB region is drastically altered for the photo-aggregated samples. Here we can see that especially the GSB of the photo dimerized solution does not anymore correspond to the absorbance of the fresh solution. Hence, I would draw the conclusion that, as long as the GSB does not alter from the ground state absorbance we could use the measured fs-TA data for further analysis. Furthermore, the comparison of the transient spectra of **D4A** in CF shown in Figure 30 reveal that the ESAs located at 575 nm and 650 nm can be attributed to the photo dimer state, while the ESA at 730 nm can be attributed to single molecule.

*Transient Kinetics of **D3A***

D3A, as shown by the huge differences in the fluorescence quantum yield, should show clear differences for the observed kinetics in solution upon changing the pump wavelength. As **D3A** also shows very interesting supramolecular structures in LB-films, it is also interesting to investigate how these structures alter the kinetics after photoexcitation. Since aggregation in CF

is present in even low concenctrations we also used DMSO as second solvent, which should show no or a very low number of aggregates within the solution. With DMSO as second solvent,also the effect of solvent polarity can be investigated. To determine the effect of aggregation on the transient kinetics of D3A either solutions made with two different solvents (DMSO and CF) or solid thin films with different morphology made by drop casting, spin casting and the LB-technique were used.

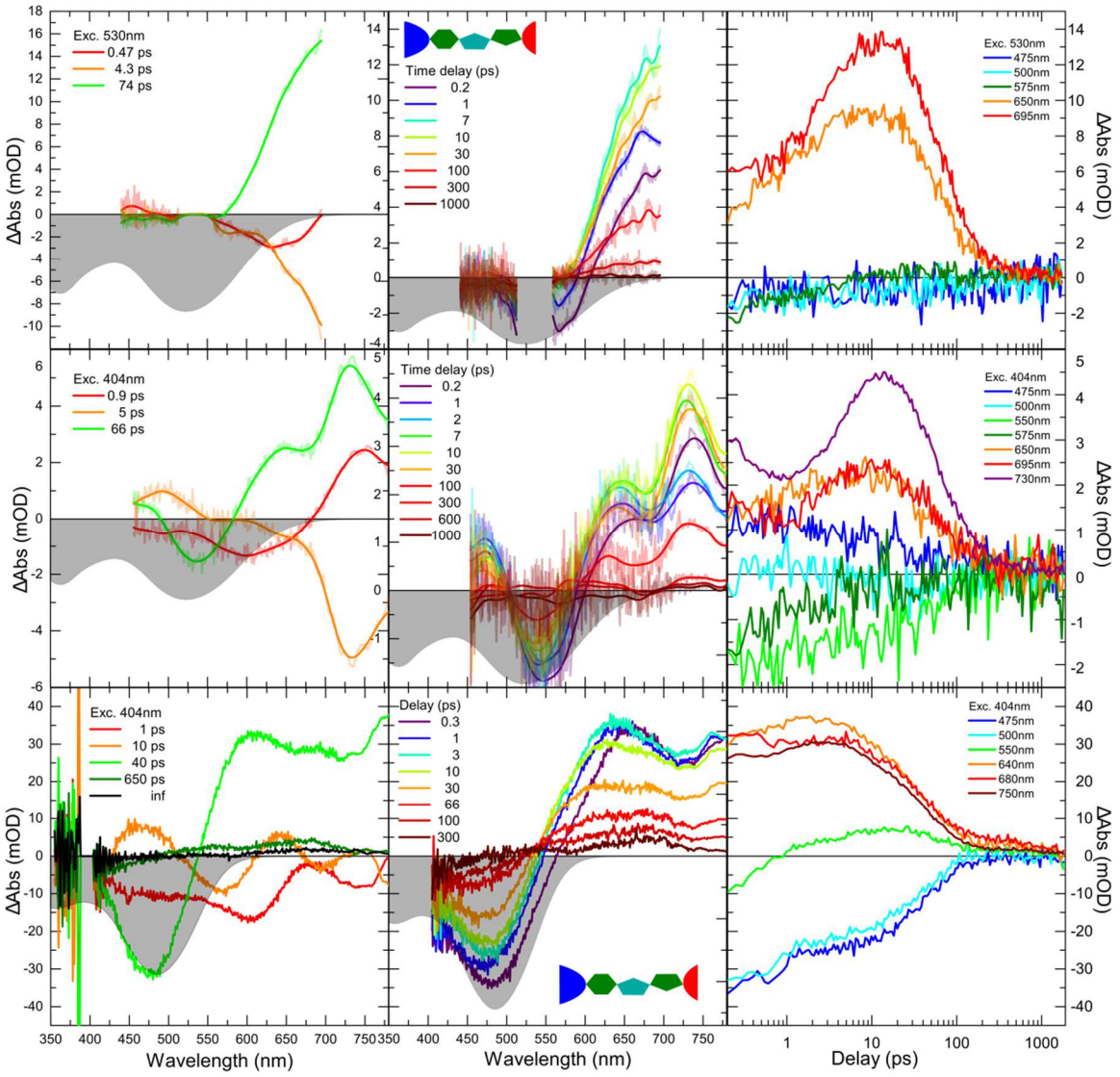

Figure 31 Comparison of the transient absorption spectra of **D3A** in CF and DMSO. DAS are shown in the left column, spectral traces in the middle column, while the kinetic traces are shown in the right column. The excitation of CF solutions was done with 530 nm for the upper and 404 nm for the lower row, while the data for DMSO excited at 404 nm is shown in the lower pannel.

Pumping the lowest energy transition at 530 nm, we get the transient kinetics and spectral traces shown in upper row of Figure 31, corresponding most probably to the S_0 to S_1 monomer transition, we find a build-up of excited-state absorption around 650 nm and above the detectable wavelength range. From the TA-spectra measured at an excitation wavelength of 404 nm shown in in the middle row of Figure 31, it can be concluded, that the ESA signals above

the measurable range are located roughly at 730 nm. The same conclusion can be made by taking a look onto the fs-TA data measured on the second batch of **D3A** shown in Figure A 17 in the appendix and in the DAS of the measurements of the new batch D3A shown in Figure 33. The build-up of the ESA at 695 nm is done within ten ps and can be assigned to the hypsochromic shift of this 730 nm ESA that happens upon vibrational cooling.[185] In addition, there is a GSB centered round 530 nm, which is not clearly visible since the signal is overlapped by scattered excitation light. The GSB and the excited-state absorption decay to the ground state with a time constant of roughly 70 ps, which was obtained by the multi-exponential fit routine.

Exciting at 404 nm, which is right in-between the S_1 to S_2 and the first dimeric transition, **D3A** in CF behaves differently in comparison to the case where only the monomeric S_1 state is excited. The spectral traces can be seen in the lower left panel in Figure 31. A decrease in signal to noise ratio caused by an overall lower signal, as compared to the measurement at λ_{ex}=530 nm, can be observed. Despite this an increase in the available spectral probe range was found due to the implementation of a CaF_2 white light and the implementation of a short pass filter cutting out residual intensity of the fundamental laser light. Furthermore some changes in the spectral form can be identified: the ESA peak centered at around 650 nm can be clearly seen in the measurement using λ_{ex} =404 nm in contrast to the first measurement using λ_{ex} =530 nm. For the peak centered at round about 730 nm, we can see an interesting kinetic (See lower right panel in Figure 31). During the first ps this peak decays fast, while it is increasing in intensity from 1 ps until approx. 10 ps. Within the same timeframe the peak at 730 nm shifts to the blue by approx. 15 nm, as found by the peak fitting program. The fit results are shown in. This peak shift can be assigned to a vibrational cooling or the planarization of the molecule as found for oligo-thiophene molecules.[186] Afterwards the ESA signal at 730 nm decays to zero within approx. 200 ps. Using the DAS spectra (see Figure 33) obtained by the multi-exponential fit routine gave a time constant of approx. 70 ps, like in the experiment using 530 nm excitation wavelength. Taking into account that the TA data of the 530 nm excitation experiment have a reduced spectral range, the remaining transient kinetics are almost identical. Hence, the transient kinetics does not give any evidence, why the fluorescence quantum yields are that much different upon using 405 nm and 532 nm as excitation wavelength. In general the overall decay times of the excited state are fairly short and do not change significantly upon changing the excitation wavelength. Hence, the further investigation of the transient kinetics of **D3A** in solution and in thin films will only be discussed for the excitation wavelength of 404 nm.

The TA spectra of **D3A** pumped at 404 nm in DMSO in comparison to the kinetics measured in CF are shown in the lower row of Figure 31. The spectral features taken from the spectral traces are a GSB centered at 490 nm and an ESA at 650 nm, which shifts to the blue within the first ten ps. By using the Labview fit software to describe this peak we get the kinetic of the peak position which is shown in Figure 32. Here we see that the peak shift is completed after approx. one ps. The later can be attributed to cooling of the first exited state. Furthermore, there is either a dip at approx. 720 nm or a second ESA peak above the spectral window of the used setup. A dip would perfectly fit to the emission peak in DMSO which is centered at approx. 710 nm. The kinetics can be divided into three different parts. The first 10 to 20 ps show only slightly changes in the GSB and ESA spectral regions. Hence while the cooling process occurs the recombination to the ground state is somehow hindered. Right after the cooling in the delay time range of 20 to approx. 100 ps the GSB and ESA decay has a steeper slope. This indicates a second process of

recombination starting once the relaxed most probably S_1 state is reached. For delay times above 100 ps the signal is again nearly constant with low signal strength until the maximum delay measurable with the given setup. Hence we have one long living state where only very few exited molecules end up. The results of the fit procedure gave time constants of 12, 65 and 600 ps plus an infinity component. In this manner the simple use of decay associated spectra (DAS) might not be the best choice, since the multi-exponential fitting routine is not very well suited to describe shifts of spectral features.

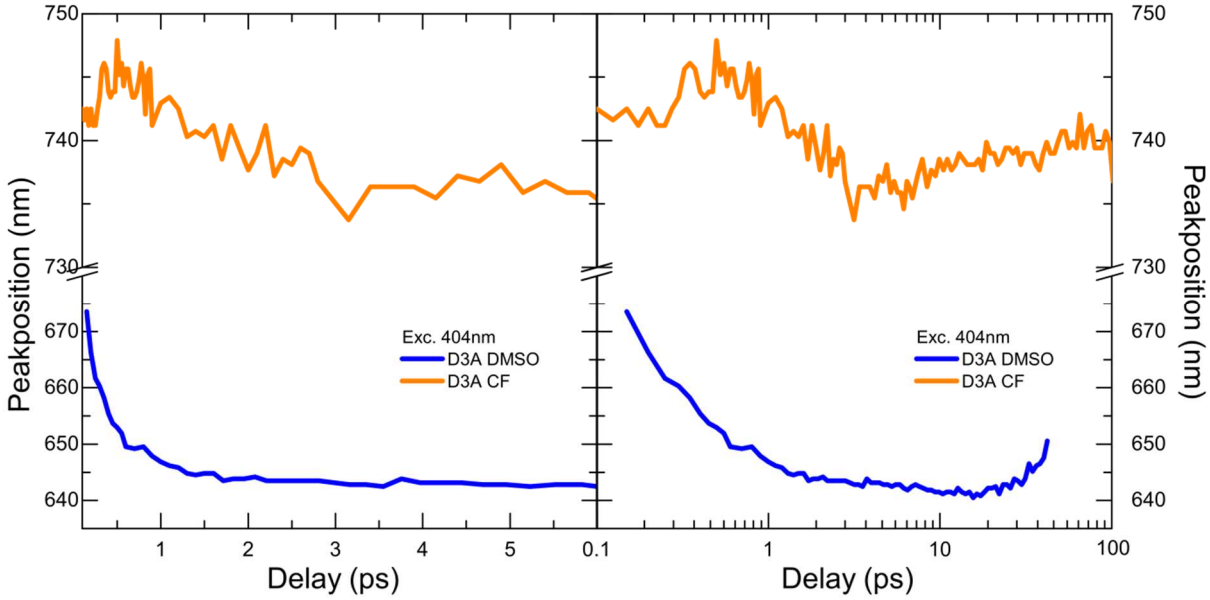

Figure 32 Position of the longest wavelength peak in the fs-TA data measured for **D3A** in either CF or DMSO and fitted by the Labview fit program. The left panel show the fit results on a linear timescale, while the right one is plotted on a logarithmic scaling. The pump wavelength of the data was 404 nm in each case.

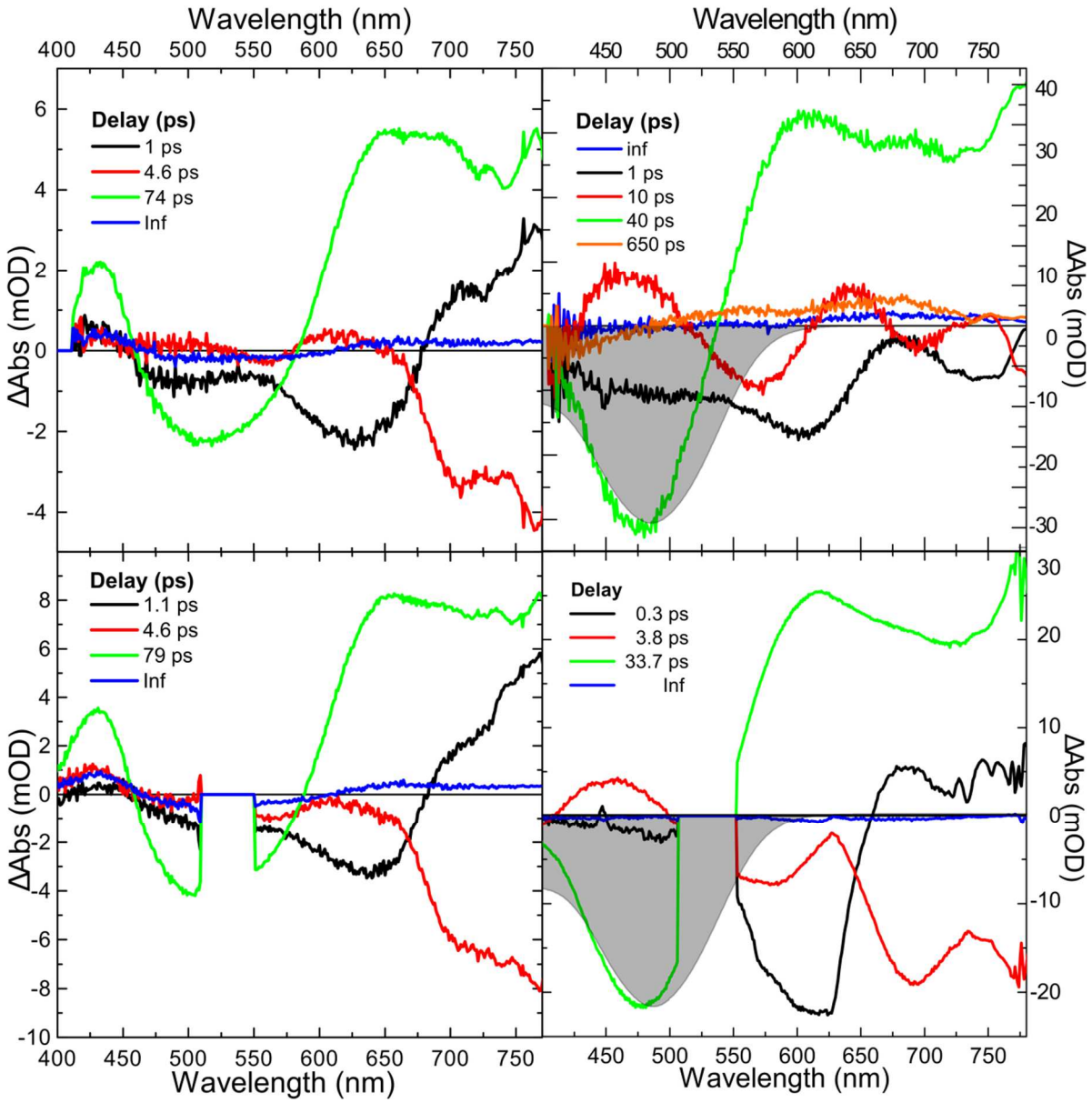

Figure 33 DAS of **D3A** in CF (left) and DMSO (right). The upper row represents the data for pumping at 404 nm and the lower row shows the data for a pump wavelength of 530 nm. The rather short time constants of 1 to 10 ps somehow represent vibrational cooling and structural re-organizations of the molecules in the excited state. These DAS are hard to be interpreted since, in this case, they have to represent the shifts in the ESA signals. These shifts are generally not well described by the multi-exponential fit with DAS.

The following time constants were not determined from the DAS, but by a simple estimation of the delay times between the reached maximum of the ESA peak at 650 nm (DMSO) and 730 nm (CF) and the decay to 1/e of this maximum. To simplify the data interpretation, the decay of the first ESA peak will be used for comparison of the effect of solvent and morphology in thin films for the following datasets. This gives a mean recombination time of the given excited states and allows using one number to compare the deactivation of the excited state in all solvents and solid state morphologies. This is especially useful, because in the solution case we have several processes like peak shifts and overlapping signals, which both are hard to handle by the fitting procedures used to calculate the DAS. Despite the decay of the signals, we see from the fit of the peak position, drawn in Figure 32 that the cooling process is much fast in DMSO in comparison

to CF: While the shift of the NIR peak is done within less than 1 ps in DMSO the peak shift in CF occurs within approx. 3 ps. The peak shifts by 100 cm^{-1} and 720 cm^{-1}, for CF and DMSO, respectively. Hence, in the more polar DMSO the polar ground and even more polar excited state is energetically better stabilized in comparison to the less polar CF. This indicates an energetically lowered excited state and hence an increased energy difference to the higher excited states. The faster cooling in DMSO can also be explained by the lower solvent dephasing times in comparison to CF as it was already published for Coumarin 153.[187]

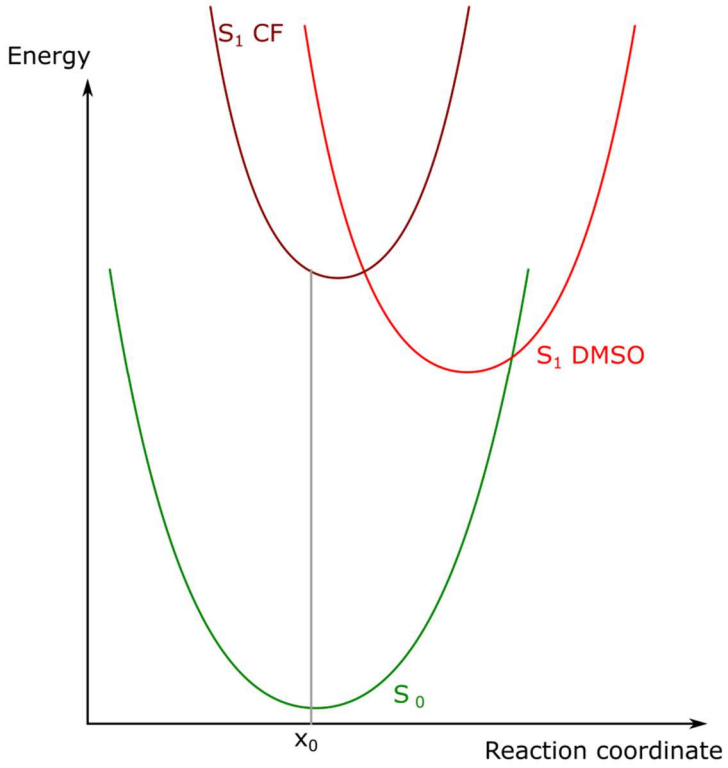

Figure 34 Schematic graph of the potential surfaces of **D3A** in either CF and DMSO drawn in comparison to Scheme 5 in the work of Ishow *et al*.[188] On the x-axis the reaction coordinate and on the y-axis the energy is drawn. The potential surfaces of the S_0 and S_1 states are simplified as parabolas having a different equilibrium displacement and energy for CF and DMSO, respectively.

The enhanced recombination, which seems to be counterintuitive for a more stabilized excited state, can be explained by an increased geometrical reorganization in the more polar DMSO as it is shown in Figure 34. This leads to a bigger displacement of the relaxed S_1 potential surface giving a much lower S_1/S_0 energy gap and potentially potential surfaces in very close proximity. This facilitates a fast internal conversion from S_1 to S_0 and hence a faster recombination.[188]

Comparing these time constants of the recombination between 10 and 100 ps we find that the recombination of **D3A** in DMSO is faster (40 ps) than in CF (85 ps). This is in line with the lower fluorescence quantum yield in DMSO in comparison to CF. Furthermore, in the more polar DMSO the recombination is faster, which is very common for molecules were the final excited state has a strong ICT character.[188, 189]

*Transient Kinetics in Thin Solid Films Made of **D3A** with Different Morphology*

Changing from the solution to a fairly disordered thin film morphology obtained by simple drop casting (DC) we find significant differences between the TA spectra of the solutions and of the DC-films shown in Figure 35. In contrast to the solution TA-data, the data obtained for the DC film, shown in Figure 35, no peak shifts are observed. Furthermore, the kinetics shows a monotonously decreasing signal. The ground state bleach for the lowest energy S_0 to S_1 transition is only visible as dip at around 570 nm. This is due to the superposition of a much stronger ESA ranging from 450 to above 770 nm giving a positive signal with the weaker negative signal of the GSB. To analyze the kinetic traces in more detail, DAS were calculated using the multi-exponential fit routine. The fit giving the DAS are not disturbed by significant peak shifts in case of the DC-films, in contrast to the solution cases. The DAS are shown in the middle panel of Figure 35. This fit gives decay time constants of 2, 22 and 260 ps plus an infinity component. The 1/e value determined at 750 nm, representing a median decay time constant, is 52 ps. Hence the recombination at early times is more efficient than in the CF solution, but less efficient than in DMSO. Furthermore, there is an infinity component, which was not found for either of the solution measurements. These long living ESA indicates the population of a state which is very stable. As long living states triplet states are candidates. The spectral signatures of these are often found right below the band gap, as it was observed for different merocyanine dyes.[190, 191] Because no evidence for the formation of a long living triplet state was found in the solution experiments, this explanation seems to be less probable. Hence, intermolecular states should be taken into account, which is somehow self-evident for molecules packed in a solid-state film. Delocalized excitonic or charge separated states are very common in solid state films of *e.g.* different thiophene dyes.[186] These states are also known to be relatively long living with lifetimes ranging up to the µs time regime. [186, 192] Also their kinetics should strongly depend on the intermolecular arrangement, which will be discussed in detail in comparison with the thin films made by LB-technique and spin casting (SC).

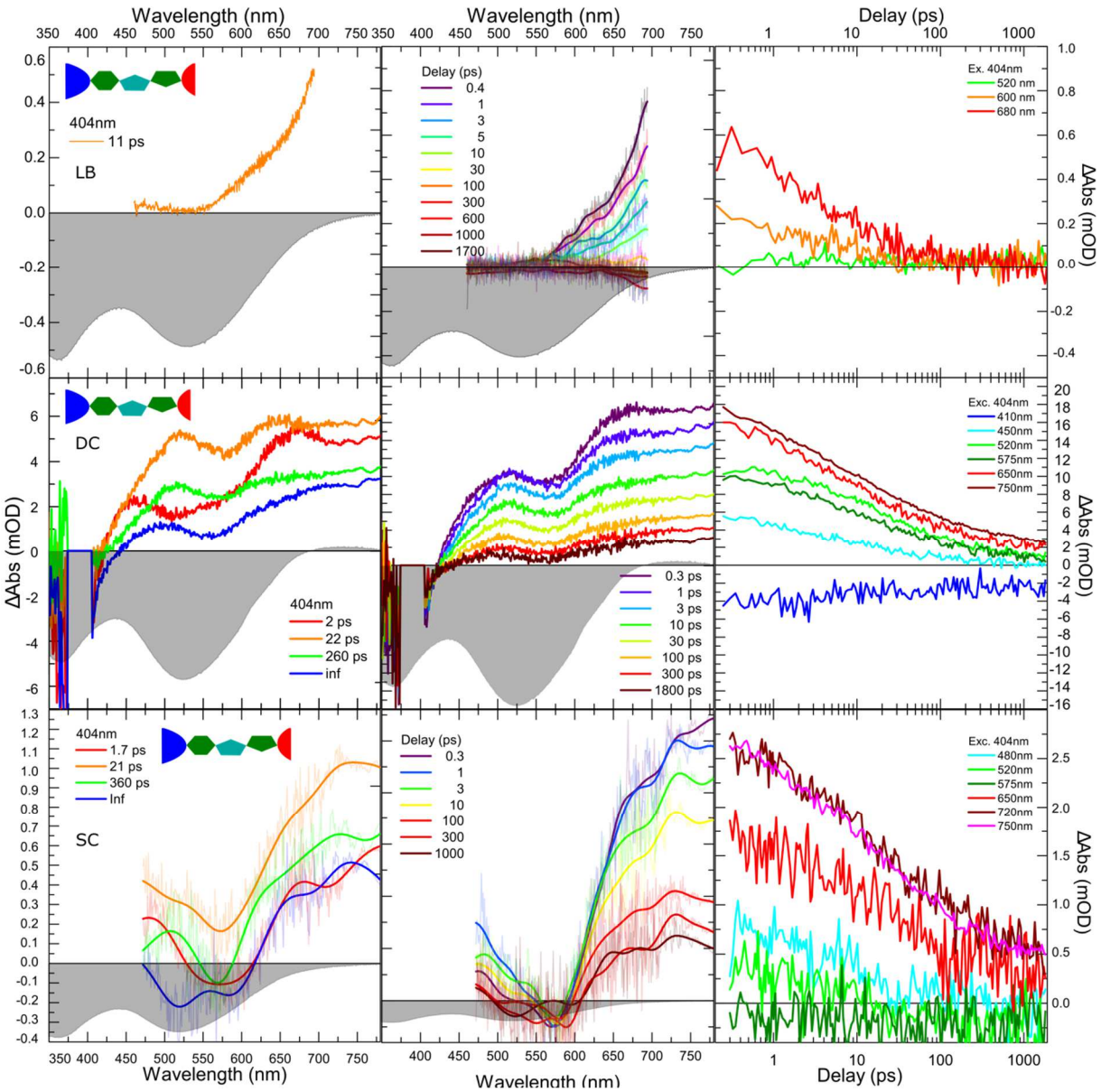

Figure 35 Comparison of the transient absorption spectra of **D3A** thin films. The DAS are shown in the left column, spectral traces in the middle column and the kinetic traces are shown in the right column. The samples were either LB-films transferred at 25mN/m (top row), drop casted (middle row) or spin casted (lower row). For the LB- and SC film smoothed lines are drawn as a guide to the eye, while the raw data are shown slightly opaque. The excitation was done with 404 nm.

Spin casted film show a different morphology in contrast to the drop casted ones, which was already shown exemplarily for **D4A** by AFM images in the previous Chapter. The major difference in the film formation is that in case of SC films the film formation and solvent evaporation are usually very fast. This leads to SC-morphologies that are far from thermodynamic equilibrium.[27, 193] The TA spectra of the SC-films show significant differences to the DC ones. Firstly, the signal-to-noise ratio is worse due to the low optical density as seen in the spectral trace in Figure 35.

The differences in the spectral features in comparison to the DC-films are the more visible GSB around 550 nm that is, at least less, masked by an ESA feature. Furthermore, we see similar ESA

signals around 480 and above 620 nm. The kinetics derived by the DAS reveals decay time constants of 2, 20 and 360 ps plus a long living infinity component. The 1/e time delay was determined at 720 nm to approx. 100 ps. Hence, the, in comparison to the DC –films more disordered, SC -film shows similar early stage process time constants. The slower processes above 100 ps shows a longer delay time. In comparison to the DC film the delay time is increased from 260 to 360 ps.

For the most ordered thin films made by the LB-technique and transferred at a surface pressure of 25 mN/m the kinetics and spectral traces are shown in Figure 35. Despite the low optical density of the used sample, we could get fairly enough signal to fit the data using a mono-exponential decay kinetics with a very short time constant of 11 ps and 1/e delay time of 6ps. Hence, this film with a high degree of order has the most efficient and fast excited state deactivation channel. The estimated decay times are in comparison with the more disordered SC- and DC- thin films and also with the molecules in solution at least one order of magnitude shorter. This very fast recombination is indeed the reason for the not measurable fluorescence and will also lead to reduced solar cell performance in DSSCs.

Comparing the 1/e values for solution and thin films we found the trend illustrated in Table 3. In solution we find that the decay time constants decrease by using the more polar DMSO in comparison to CF, when pumping the energetically lowest excited state (S_1). This acceleration of S_1 deactivation upon increased solvent polarity implies a polar nature of the S_1 state, as already discussed in Chapter 3. This was concluded from the charge difference densities obtained by the TD-DFT calculations, which also show a strong ICT character of the first bright excitation (see Figure 11). This means that we observe an internal charge transfer (ICT) state as final excited state and no long living triplet state.[189] This also fits to the charge difference densities obtained by the TD-DFT calculations, which also show a strong ICT character of the first bright excitation (see Figure 11). For the solid state films with different intermolecular orientation and degree of ordering it was found that for samples with a somehow amorphous character (SC and DC films) a long living, most probably intermolecular charge separated, state was formed. Furthermore, the recombination rate is increased, when the molecules have more time for film formation and hence getting closer to a thermodynamically favorable, more crystalline structure. At even higher molecular order, as induced in the LB-technique, a drastically increased deactivation rate is obtained and the intermolecular charge separated long living state could not be observed anymore. Hence, a parallel orientation, which should be promoted by the LB technique, is not able to stabilize a charge separated state. Because a very similar intermolecular orientation will usually be found by sensitizing TiO_x in DSSCs the increased recombination rate will decrease the device performance. Hence, for this molecule the use of aggregation inhibitors is strongly recommended and will, as shown by Menzel *et al*.,[71] increase efficiency of DSSCs made by **D3A** by a reduced recombination rate.

Table 3 Decay time constants for the NIR peak around 700 nm for D3A in solution and different thin films pumped at 404 nm. The time constants were determined by using the time were the ESA peak decays to 1/e of the maximum value.

Sample from **D3A**	CF solution	DMSO solution	SC thin film	DC thin film	LB thin film
$1/e$ delay time (ps)	85	40	100	52	6

*Transient Kinetics of **D4A***

The longest molecule, investigated in this work **D4A,** dissolved in CF, shows distinctly different behavior when pumped at one of the two lowest energy transition at around λ_{ex} =530 nm and λ_{ex} =404 nm, respectively. The transient kinetics and spectral traces of the transient absorption measured with a pump wavelength of 530 nm in CF are shown in Figure 36. Using 530 nm as pump wavelength the lowest energy transition is excited, which is most likely the monomeric S_0 to S_1 transition. Here the ground-state bleach (GSB) is found to be centered at 550 nm. Furthermore, an unstructured excited-state absorption ranging from 600 nm to above 700 nm could be seen in the same measurements. The ESA has a build-up time-constant of around 4 ps and a decay time of 140 ps. This seems to be very similar to the findings for **D3A** in CF pumped at 530 nm. In the case of **D3A** also a build-up of an ESA that was done within a few ps was observed. Afterwards this ESA decays to the ground state with a time constant of approx. 70 ps, which is shorter than in the case of **D4A**. The build-up of the ESA seen for **D4A** in CF is a combination of the vibrational cooling of an ESA peak centered right outside the observation window plus and stimulated emission centered at round about 600 nm. The first can be seen in the TA data shown for an excitation wavelength of 404 nm in Figure 37. The last can be concluded from the negative signals in the spectral region red shifted to the steady state absorption peak at very early times, which cannot be assigned to the longer living GSB. This can be attributed to a stimulated emission which decays within one ps. Furthermore, the signal is blue shifted in comparison to the normal steady state emission, hence we can clearly assign this to stimulated emission.

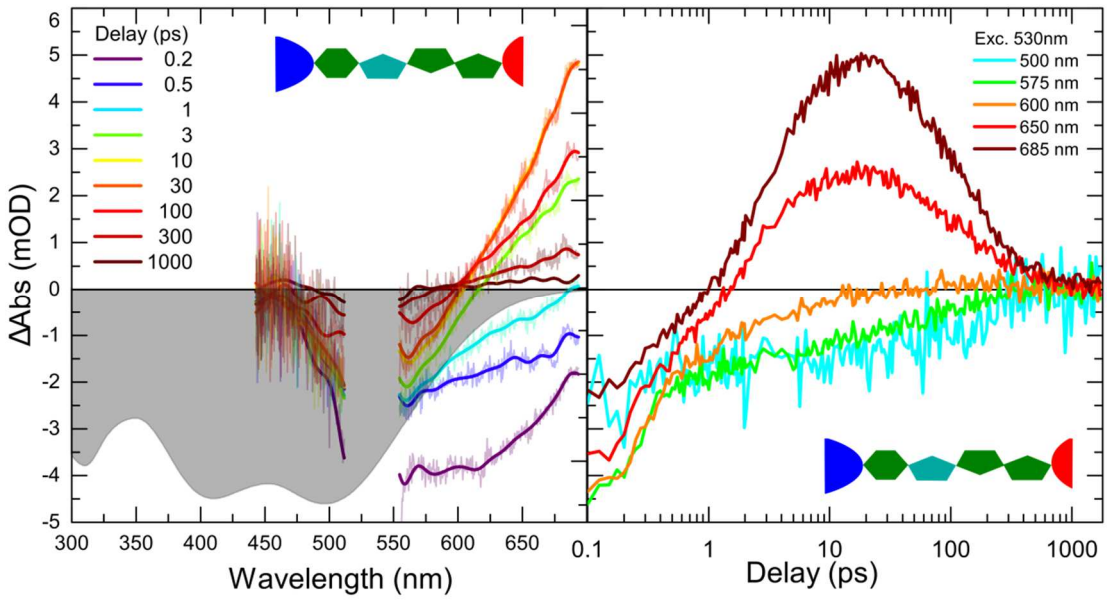

Figure 36 Spectral and kinetic traces of **D4A** in CF excited at 530 nm. The negative molar extinction coefficient is plotted in grey.

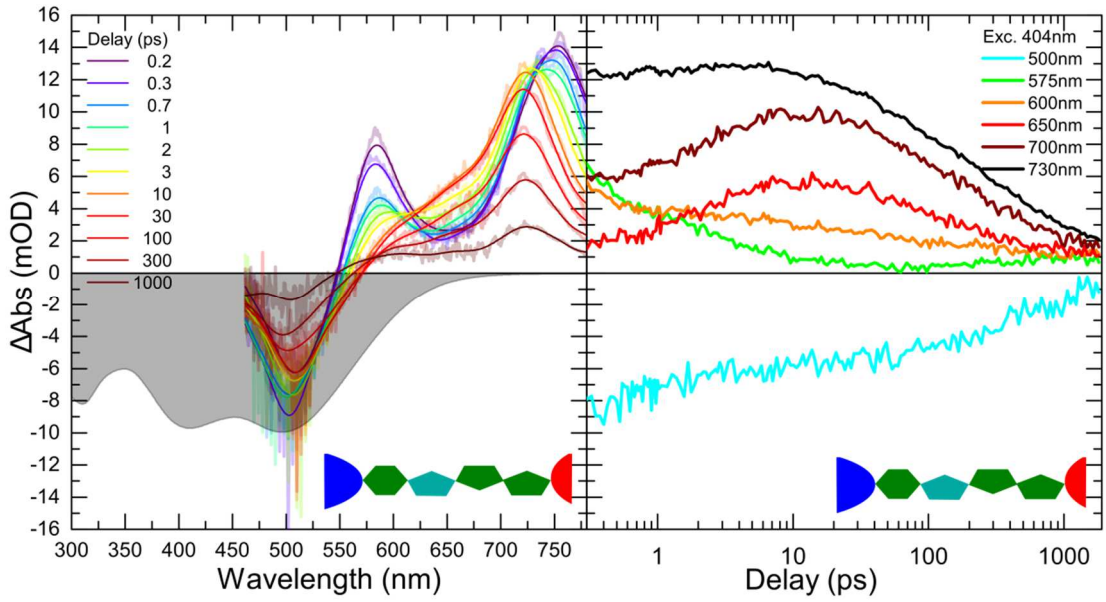

Figure 37 Transient absorption spectra of **D4A** in CF. Spectral traces are shown in the left panel while the kinetic traces are shown in the right panel. The excitation was done with 404 nm.

By exciting near the second absorption peak at 404 nm, which can be attributed to the dimeric transition, as discussed in Chapter 3, fairly different transient absorption features can be observed in comparison to the TA data observed for the pump wavelength of 530 nm. The kinetic and spectral traces of the measurement using 404 nm as excitation wavelength can be found in Figure 37. In general the here observed transient data have shown to be far away from a straight forward interpretation.

Here we see an ESA peak centered at 575nm, which decays within the first 5ps. This decay was fitted using a mono-exponential decay with time constant of 2.4 ps. This can either be the S_2 $\pi\pi^*$ state which is fast depopulated by an internal conversion to the S_1 ICT state. The other possibility would be a state localized on a dimer, which is then depopulated to the monomeric S_1 ICT state. For both processes the time constant of 2.4 ps is in the range observed for other triphenylamin dyes shown *e.g.* by Ishow *et al.*[188] This assignment can be further supported by taking into account the fs-TA spectra of the photo aggregated solution of **D4A** shown in Figure 30. Here the GSB of the monomer is very weak, while that of the photo dimer dominates. The short lived component centered at 575nm was shown to be the most prominent ESA feature of the photo dimer.

Within the decay time of this peak a shoulder is build up at 650 nm and the ESA peak at 750 nm shifts to the blue. The peak shift of the ESA at 750 nm can be assigned to a cooling process. This shift was specified by using the Labview fitting program and the results are shown in Figure 38. Here we see that the peak shift assigned to the cooling takes approx. 8 ps in CF. The overall shift is larger in comparison to **D3A** with approx. 560 cm^{-1}. Also the time needed for shifting and hence cooling is much larger for **D4A** with 8 ps in comparison to 3 ps for the **D3A** case. This indicates a more stable ICT state for **D4A**, which shows a higher structural reorganization in comparison to the very similar **D3A**.

The 1/e delay time for the decay at 730 nm is approx. 400 ps. This decay time is rather large in comparison to the 85 ps determined for **D3A** in CF. Furthermore, 400 ps is very close to time constant found in the transient emission measurement for **D4A** shown in Figure A 14. Hence, the final state from where the recombination to the ground state occurs is also the fluorescing state.

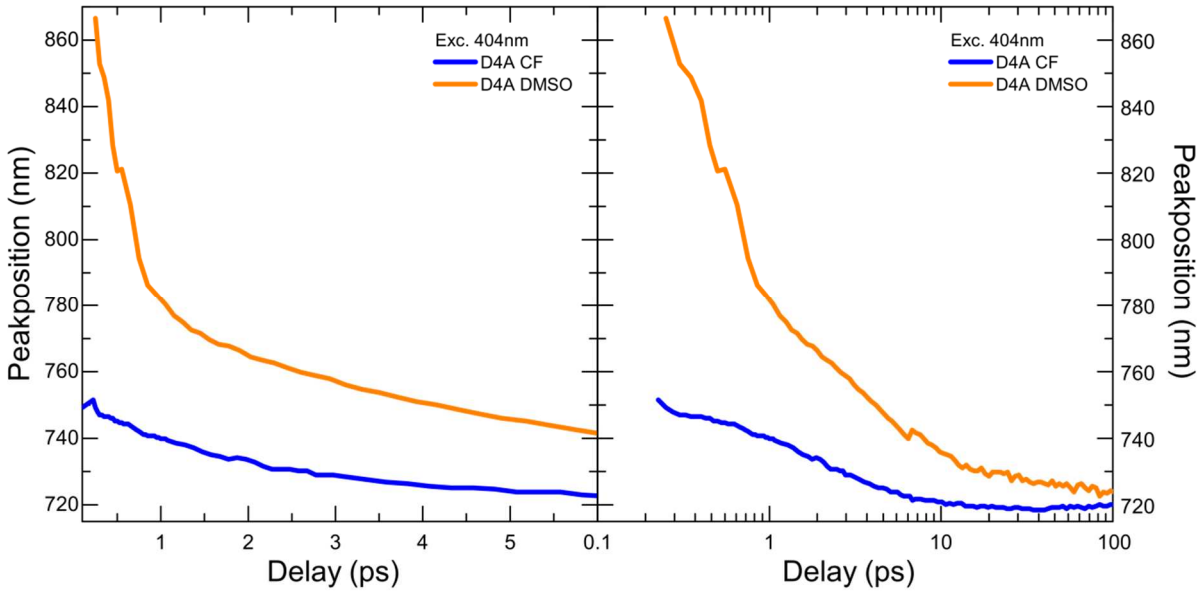

Figure 38 Peak position of the NIR fs-TA peak of **D4A** in CF and DMSO by using an excitation wavelength of 404 nm.

Hence, we have a GSB from different states with weak electronic coupling. This was also concluded from the difference in the fluorescence quantum yield shown in Figure 28 and can be attributed to the model, that the absorption peak at 400 nm is more likely a feature of dimer or higher aggregates, rather than the S_0 to S_2 transition. This is also explaining the completely different data of the transient kinetics and fluorescence obtained for the different excitation wavelength used.

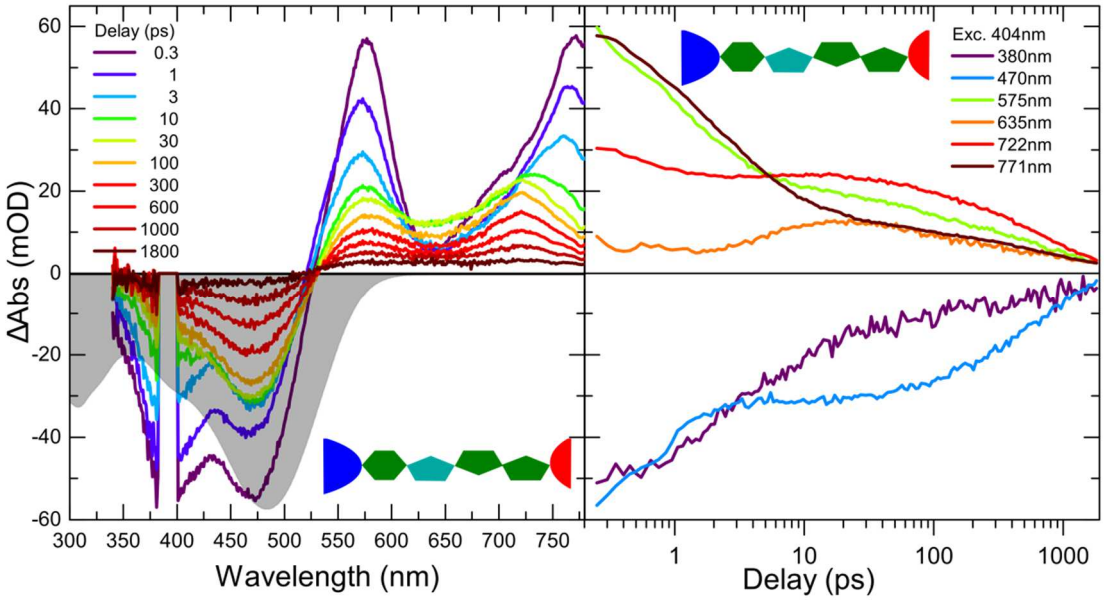

Figure 39 Transient absorption spectra of **D4A** in DMSO. The spectral traces are shown in the left panel while the kinetic traces are shown in the right panel. The excitation was done with 404 nm.

To get a deeper insight into the processes and to further determine the character of the states involved, we used the more polar solvent DMSO, like it was already done for **D3A**. By using the more polar DMSO and pumping at 404 nm, we excite the dimer or S_2 peak, which is DMSO only visible as a shoulder, as it can be seen in the grey area in the left panel of Figure 39, which

represents the absorbance of the used solution. The TA spectra reveal a very much different kinetic in comparison to the experiments in CF. The GSB does not completely correspond to the steady state absorption, because the shoulder at 400 nm is clearly visible as peak at very early delay times and vanishes within approx. 30 ps. The kinetics of this peak represented by the wavelength of 380 nm and that of the S_0 to S_1 transition represented by 470 nm reveal that the dimer state is monotonously depopulated over the whole available delay times, while the GSB corresponding to the S_1 is populated between one and 100 ps.

The ESA peak at 575 nm has a very different kinetic in comparison to that in the CF solution. Here the decay is fast for the first approx. 10 ps, but then the peak shows a much slower decay until the maximum delay time, where still some signal is left. Hence it seems that we have a state, which is only a short lived intermediate in less polar solvents like CF, which is stabilized by the more polar solvent DMSO. The cooling process in DMSO, indicated by the shift of the ESA peak above 700 nm, has a fairly different kinetic. At delay times smaller than one ps it is faster and for delay times above that it shows a kinetic similar to the measurement in CF. Furthermore the total energy shift of this peak is much higher. It is approx. 1800 cm^{-1} for DMSO in comparison to 560 cm^{-1} for CF. This means that **D4A** has a larger structural reorganization and most probably solvent shell reorganization, in contrast to **D3A**, to stabilize the highly polar excited state, found by the TD-DFT calculation ins Chapter 1.[95]

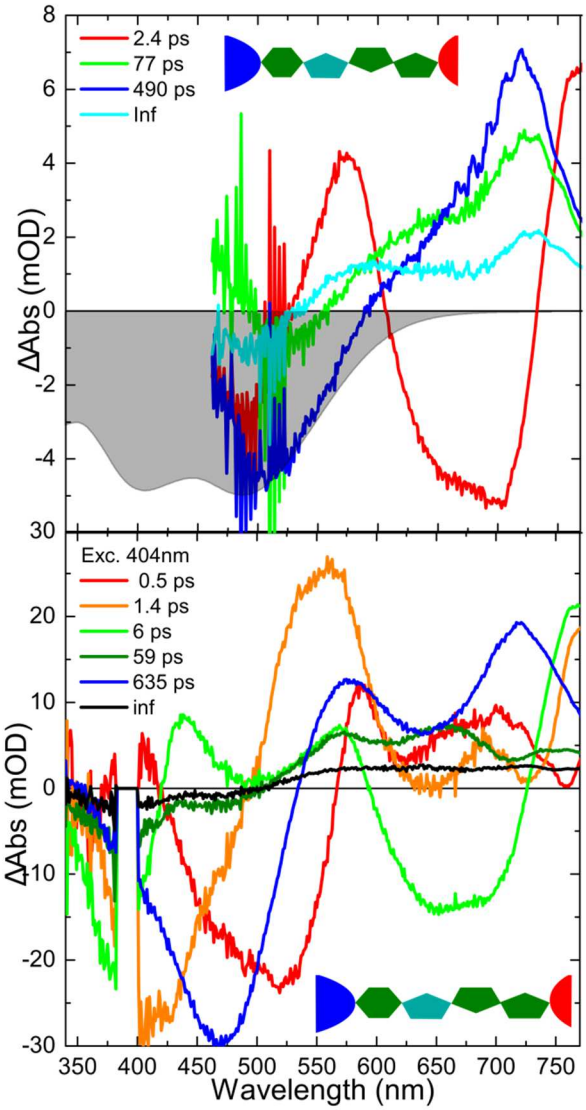

Figure 40 DAS of **D4A** in either CF (top) or DMSO (bottom) pumped at 404 nm. The high number of needed exponential curves to fit the data is mainly caused by peak shifts, which are fairly improper represented by the multi-exponential decay fit.

Using the DAS obtained by the multi-exponential fit procedure, shown in Figure 38, for interpretation is in this case not rational, due to the large shifts in the ESA peaks. This is especially obvious in the case of **D4A** in DMSO as illustrated in the lower panel of Figure 38, where six components were necessary to fully describe the measured data. The data obtained for the CF solution still need four components to be fitted. Hence, the interpretation of the transient absorption data of **D4A** in solution could not be merged into a conclusive model. This might be caused by the fairly difficult ultrafast processes occurring between single molecules and aggregates addressed by pumping at 404 nm. What can be concluded from the TA data of **D4A** in CF is that the complete decay to the ground state via the fluorescing final excited state is found by exciting the monomer S_0 to S_1 transition at 530 nm. By exciting the aggregate peak at 404 nm one always ends up in a long living state with intermediate states, which are fairly hard to be interpreted from the TA data. Comparing the solution transient absorption data obtained for **D4A** in DMSO, CF and photo aggregated **D4A** in CF the ESA signal centered at approx. 575 nm

can hardly be understood. What is obvious from the data is that the state correlated to this signature is a very short lived intermediate state. This state is depopulated within approx. 1.5, 2.4 and 3 ps for CF, DMSO and photo-aggregated **D4A** in CF, respectively. These time constants are extrapolated from the DAS in **Figure 45**. The depopulation seems to go to a long living state represented by a broad ESA feature centered at round about 650 nm. In case of the solution in DMSO and also slightly for the fresh CF solution there is a slight increase or a reduced depopulation of the single molecules S_0 to S_1 GSB signal at approx. 500 nm. This is more visible in the kinetic trace at 470 nm in DMSO (See Figure 39) and the kinetic trace at 500 nm in CF (See Figure 37). This transfer of energy from the unknown, most probably dimeric, state to the normal single molecule GSB is somehow only possible for molecules and photo dimers in close proximity. By going beyond (photo) aggregates in solution towards molecules densely packed into thin films by *e.g.* drop casting we suppose to see very different features in our transient absorption data, which was also seen for the shorter molecule **D3A**.

*Transient Absorption of Thin Films made of **D4A***

As first step the strongly disordered thin films made by drop casting *(DC)* are under investigation. Here we do not have one distinct type of intermolecular arrangement, but a rather diverse morphology. This can be seen by the only slightly suppressed S_0 to S_1 transition in comparison to the solution case.

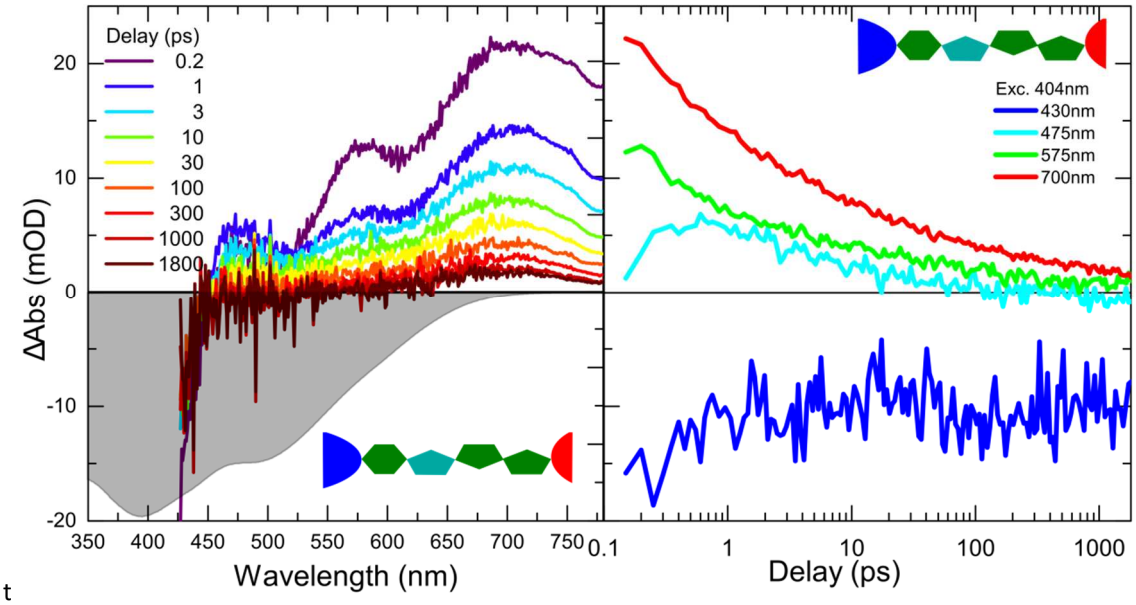

t

Figure 41 Transient absorption spectra of **D4A** drop casted films. The spectral traces are shown in the left panel while the kinetic traces are shown in the right panel. The excitation was done with 404 nm.

The TA spectra of the drop cast film reveals for the excitation at 530 nm only a mono-exponential decay with a time constant of 29 ps plus an additional infinity component shown in the DAS in Figure 44 The kinetics and spectral traces are shown in the appendix. By exciting the dimer at 404 nm, we found a significant different behavior illustrated in Figure 41. There is a negative signal below 430 nm, which fits to the dimeric absorption peak at round about 400nm and can hence, can be assigned to the GSB. Interestingly a GSB from the monomeric transition at around 500nm is not visible and the GSB is rather constant over within the timeframe of the experiment. Furthermore, there are three ESA peaks at 475, 575 and 700 nm. The peak at

475 nm corresponds to an ESA, which is build up within 1 ps. Afterwards this ESA decays to zero within approx. 50 ps with a 1/e delay time of 8 ps. The ESA peak at 575 nm shows no build up and decays slower than the ESA at 475nm. Since this feature is part of the fitted DAS corresponding to the time constants of 0.2, 1.4, 14 and 206 ps, shown in Figure 44, one could only state that parts of the signal are fairly long living, while 1/e decay time is rather slow with approx. 5 ps. The peak at 700 nm corresponds to the longest living species and has a1/e delay time of approx. 10 ps. Overall the kinetic traces reveal that we have several processes with fairly different time constants, which can be derived from the kinetic traces on the right panel of Figure 45, which do not show different regions with rather linear regions. For fitting the data four time constants and an infinity component were needed. The time constants gained are 0.2, 1.4, 14 and 206 ps and the DAS spectra are shown in Figure 44. The need for this high number of components might be caused by the highly diverse energetically landscape. The difference of the kinetics upon changing the excitation wavelength from 530 nm to 404 nm of the very amorphous DC-film reveals that there is a weak electronic coupling between the states that are populated. *E.g*., in the DC-film we do not observe a GSB signal from the monomer if we excite at the dimer transition and *vice versa*, which is fairly different from the transient data measured in solution. This is very much different from the behavior found for **D4A** dissolved in either CF or DMSO. In the DC-film we do not observe a GSB signal from the monomer if we excite at the dimer transition and *vice versa*, which means that we most probably start from different regions having not the same ground state.

The highly ordered Langmuir-Blodgett (LB) film made of **D4A** has been deposited at a very high surface pressure of 40 mN/m. It shows distinctly different behavior in TA-measurements depending on whether the aggregate main-absorption (Exc. 404 nm see Figure 43) or the suppressed monomeric transition (Exc. 530 nm see Figure 42) is pumped. Pumping the suppressed monomer peak at approx. 520 nm, we found a broad GSB similar to the monomeric transition and the blue tail of an ESA which starts right at the edge of the spectral range and is similar to the ESA of the DC film. The DAS shows a bi-exponential decay with time constants of 1.4 and 20 ps. Hence the recombination is much more efficient as compared to solution and drop cast films.

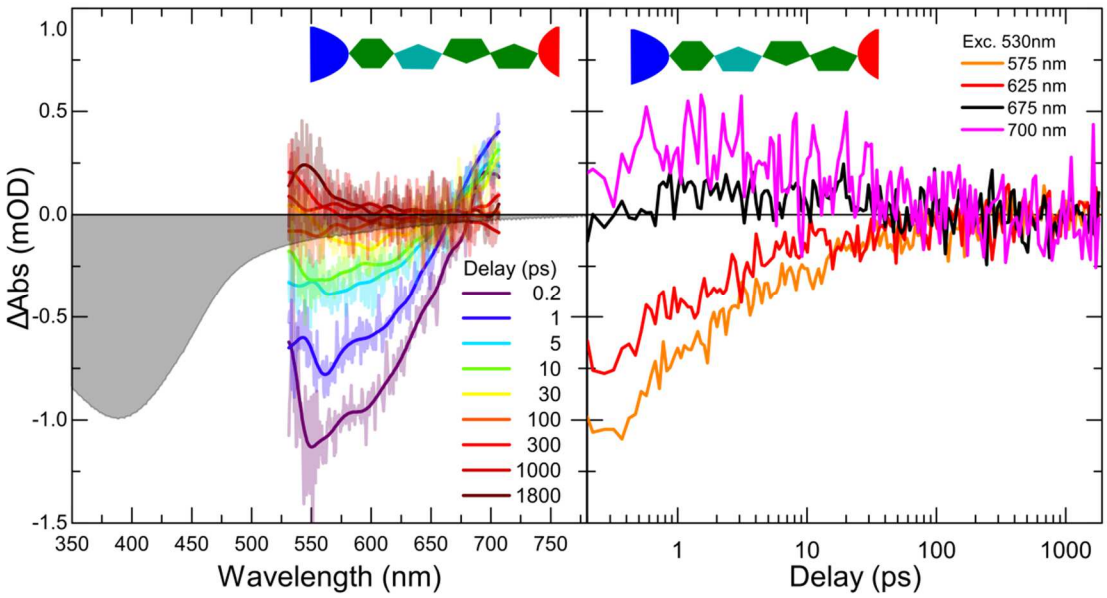

Figure 42 Transient absorption spectra of a **D4A** LB-film transferred at 40 mN/m. The spectral traces are shown in the left panel while the kinetic traces are shown in the right panel. The excitation was done with 530 nm.

Pumping the aggregate transition at 404 nm we got a complete different picture than by using λ_{ex} =530 nm . As shown in Figure 43, we see the tail of the GSB of the transition centered at 400nm, but no GSB signal at the monomeric transition, which was found for the experiment with λ_{ex} =530 nm. The ESA is dominated by a peak at approx. 500 nm and a broad structure that extends from 550nm to the end of the spectral window of the given experiment. The transient absorption data could be fitted by using two components having time constants of 4.3 and 170 ps. The corresponding DAS can be found in Figure 44. Comparing the time constants with those determined for a pump wavelength of 530nm, we find an increase of a factor 4 to 10. Hence, the recombination is still fast, but the recombination of the here pumped dimer state has a different pathway.

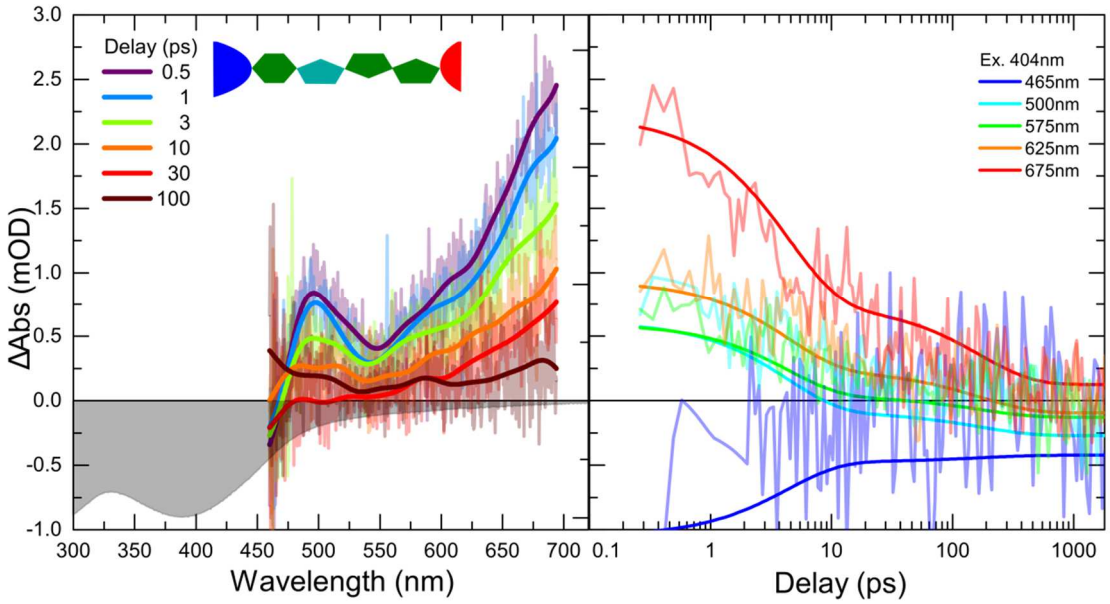

Figure 43 Transient absorption spectra of a **D4A** LB-film transferred at 40 mN/m. The spectral traces are shown in the left panel while the kinetic traces are shown in the right panel. The excitation was done with 404 nm.

The fs-transient absorption measurements reveal several differences in the kinetics of the dyes when dissolved in CF or DMSO as compared to thin films. Surprisingly, we also found the transient behavior to change drastically upon a change of the pump wavelength. This indicates that the electronic transitions are either localized on spatially separated units or that they are electronically decoupled due to forbidden transitions between the excited states[176]. This conclusion can also be drawn from the differences in fluorescence quantum efficiencies shown in Figure 28, because for all molecules investigated in this study the deactivation time-constants reduce from solutions to thin films. In more detail, this observation means that molecules in close proximity to each other, *i.e.*, aggregates in thin films, exhibit faster recombination channels for non-radiative deactivation than molecules that are far apart from each other, *i.e.*, solutions of low concentration.

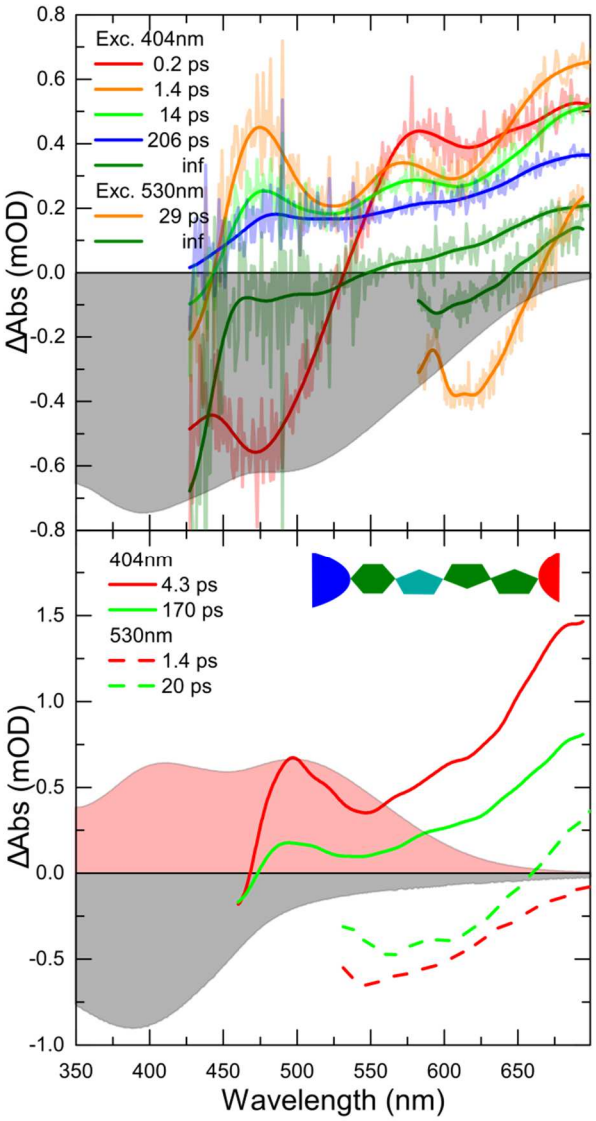

Figure 44 DAS of **D4A** of a drop cast film (top) and a LB- film (bottom). The absorption of the respective sample is shaded in grey. In case of the highly compressed LB-film the CF-solution absorbance is plotted in light red to visualize the position of the suppressed S_0 to S_1 transition.

Discussion

For different merocyanine dyes, it has been reported that excited-state absorption around 700nm can be assigned to the formation of different triplet states that are usually located right below the bandgap.[190, 191] The fast build-up time of about 2 ps for **D4A** and **D3A** corresponds to what has been reported by Lenz et al[190] and, hence, might be due to fast intersystem crossing in the presence of sulfur.[194] This explanation is contradicted by our measurements, which show a build-up time smaller than 200 fs in thin films, *i.e.*, the time-resolution of our setup. Furthermore, we were not able to determine phosphorescence in time dependent emission experiments. By exciting at the S_0 to S_1 transition we were also not able to measure any long living state, which could be assigned to a triplet state. Thus, the formation of triplet states is unlikely. A more likely explanation for fast the build-up is a planarization of the first excited state

geometry. Time constants as low as 5ps for the planarization process have been reported by Lanzani *et al.*[186] for oligothiophenes in solution.

Table 4 Decay time constants for the NIR peak around 700nm for **D4A** in solution and different thin films pumped at 404nm. The time constants were determined by using the time were the ESA peak decays to 1/e of the maximum value.

Sample from **D4A**	CF solution	DMSO solution	SC thin film	LB thin film
$1/e$ .delay time (ps)	400	7	10	7

The ESA peak at roughly 730 nm might be attributed to the positively charged triphenylamine moiety of the molecule. The spectral position and shape is in good agreement with a work from Roland *et al.*[195] Since the molecule has a relatively long π-electron bridge and a strong charge transfer character for the lowest transition, it is likely to see similar signatures as found for the positively charged donor moiety right after photoexcitation. This signature of the charged triphenylamine moiety would also explain the very fast build-up of this ESA feature, which takes approx. 300 fs. Furthermore, the reduced lifetime by changing from CF to the more polar DMSO is very common for strongly charge separated (ICT) states[189]. Furthermore, signals in the 700 nm region are also found for the cation of very similar DSSC dyes[101] and in the ESA spectrum of other triphenylamine containing molecules[196].

In the solution we could generally see that **D4A** has always an infinity component with a lifetime of more than 2 ns, while **D3A** is completely relaxes to the ground state within less than 2 ns. This difference might be caused by the longer π- bridge which allows a more stable intramolecular charge separated state (ICT) for **D4A** in comparison to **D3A**. Another possible explanation is the formation of dimeric intermolecular charge separated states, which finally lead to photo-dimers already described in Chapter 3. This would also explain the higher rate of photo-dimerization of **D4A** in comparison to **D3A**, which should be facilitated by the longer lifetime of the intermolecular charge separated state.

Changing the intermolecular arrangement of **D3A** in solid state films we find that with increased ordering or aggregation, in this case from spin coated to highly ordered LB-Films, the creation of very efficient and fast recombination channels to the ground state. Especially for the parallel inter-molecular arrangement obtained from the LB-technique a very fast recombination was found. This conformation is very similar to the conformation one would assume for dyes and dye-aggregates attached to the TiO_x of DSSCs. Hence the recombination of the pristine dye on the electron accepting oxide will drastically be increased with increased density of molecules.

For **D4A** the deactivation is also faster with increased aggregation, but it seems that the recombination has a different pathway, which includes the dimeric state that absorbs at approx. 400 nm. Additional sample series, which includes LB-films transferred at different surface pressures with tuned aggregation, were prepared several times, but it turned out that it was

impossible to get a decent TA signal from most of the measured LB-films. This clearly is due to the very low optical density of approx. 0.03 or less for LB-films.

6 Summary and Outlook

The supramolecular structure essentially determines properties and function of organic solar cells and other organic optoelectronic devices. Aggregation in organic bulk heterojunction (BHJ) solar cells is usually beneficial and a lack of aggregation is one of the main factors limiting the efficiency.[170, 197-201] In contrast to BHJ solar cells, aggregation in dye sensitized solar cells (DSSCs) usually reduces the efficiency.[31, 32] The research on morphology and aggregate structure of molecules used in BHJ solar cells is here just briefly mentioned, due to the numerous articles published on this topic.[6, 157, 162, 202-205] By a simple search for "morphology" and the most investigated polymer used in BHJ solar cells, which is "P3HT", more than 2700 papers can be found *via* the "web of knowledge". In the field of DSSCs, the research on aggregates and intermolecular structures is much less developed. The focus here is set on a possible decrease of the efficiency of DSSCs by aggregation of the dyes[41, 206, 207] and how it could be prevented by different aggregation inhibitors[35, 37, 57]. To enhance the knowledge about aggregation of dyes and their effect on electro optical parameters, it is very useful to have a model system of similar molecules, which can be forced into different intermolecular arrangements in thin films. With these model systems, it is possible to investigate the influence of different aggregate structures on the optical absorption, emission and recombination kinetics. Another point that turned out to be crucial is, that especially dipolar molecules tend to build dimers, micelles *etc*. in solution. Furthermore, it turned out that the dimerization can be enhanced by the illumination with light.[95]

For investigating the influence of different aggregate structures, the structure of the aggregates should be varied in a controllable manner. This tuning can either be done by changing process parameters at film formation[27, 76] or by changing side groups of the molecules[173] as established in tuning morphologies of BHJ solar cells. All these parameter changes will facilitate the formation of aggregate structures, which are formed by getting the molecules into different arrangements by *e.g.* spin coating and post-annealing. This will result in mixed local aggregate structures, which are made of highly crystalline parts and more amorphous regions.[6, 158, 208]

As a complementary technique to drop and spin casting the Langmuir-Blodgett (LB) technique[60] was applied here to get model systems made of thin films with tunable supramolecular structure. The LB technique itself has the advantage of controlling the intermolecular arrangement at the transfer from the water surface to the solid state substrate. The LB-technique is predestined for the use of amphiphilic molecules. As most of the organic dyes used in DSSCs already feature this amphiphilicity due to the hydrophilic acid group needed for binding to the TiO_x and a usually hydrophobic chromophore. Molecules of this class are promising candidates for the use in the LB-technique. Therefore, two different DSSC dyes synthesized by Menzel *et al.*[71] were used. Additionally, a very similar DSSC dye with a shorter chromophore from the Würthner group was investigated. All dyes have a common donor-π-bridge-acceptor design.[43] The difference in the π-bridge length and nature allows investigating the influence of the π-bridge length on the aggregation and their effect on the optical and electronical properties. The effect of aggregation of DSSC relevant dyes, like that one used here, was

investigated mainly by focusing on the effect of aggregation on DSSC device performance like it was done for H-aggregates made of Merocyanine 540.[209] Similar experiments were made for the here used thiazole-containing dyes by comparing only the device efficiency with and without using an aggregation inhibitor.[71] A detailed analysis of the structure of aggregates made of DSSC relevant dyes in thin films and attached on TiO_x is still missing.

In this thesis the effect of aggregate structures is investigated, firstly the optical properties of single molecules in solution had to be determined, as reference. Here, the extinction coefficient and fluorescence were the major observables. It turned out that in most of the used solvents, like THF and chloroform, the extinction coefficient depends on the concentration of the molecules. This indicates the presence of aggregates in solution for concentrations in the range of 10 mM.[44, 95] In the literature mainly two types of aggregates are described, namely H- and J-aggregates.[44, 47] While J-aggregates show a very narrow red shifted absorption, H-aggregates have a blue shifted absorption in comparison to the monomeric transition.[210] For the here investigated molecules only a decrease in the absorption of the monomeric peak was found, while the increase of the aggregate peak is much weaker. The increase in aggregate absorption is usually more pronounced in the literature.[49, 129, 139] The formation of different aggregates is always determined by the structure of the given molecule. This means that *e.g.* different very flat molecules usually tend to build aggregates in solution due to ππ-stacking or dipol-dipol interaction. As example the molecule class of cyanine dyes, squarines, porphyrines or perylenes can efficiently form aggregates, depending on the functionalization, that was applied to facilitate the formation of aggregates. [44] But the aggregation of DSSC relevant dyes already in solution was not found to be investigated in detail.

To get a deeper understanding of the altered optical transitions we used TD-DFT calculations to determine the nature of the optical excitations. For all used molecules the lowest energy S_0 to S_1 transition has a strong intra-molecular charge transfer character. Also elongation of the π-bridge is promoting a higher degree of charge transfer character.

Despite the change of the extinction coefficient by an increased concentration in solutions, we found that illumination of the samples with light alters the spectra upon irradiation in a very similar, but more efficient way. To quantify the changes upon illumination, a Labview software to automatically measure illumination dependent-UV-vis absorption spectra was programmed from scratch. This enables the data acquisition with constant illumination times and large illumination time dependent absorbance data sets to enhance the reproducibility. The change of the spectra in general might have two possible origins: light driven aggregation or degradation of the used molecules. Photo-aggregation and the closely related photo-dimerization are a rarely investigated process. While photo-aggregation upon the creation of J- and H-aggregates has been found for a merocyanine dye by Petrenko *et al.*[58] and Chibisov *et al.*[152, 211]. The formation of photo-dimers by creating new covalent bindings has been demonstrated for different dyes, especially if they have been forced into close proximity before starting the photoreaction.[59] Photodegradation has also to be taking into account, because it was already observed for different merocyanine dyes, having an elongated poly-methine bridge.[212] But for molecules that are more similar to the here used dyes no detailed study on either photo-aggregation, dimerization or degradation was found.

In this thesis the discrimination of both models turned out to be challenging, especially if the amount of available material is limited. First, model kinetics of 1st and 2nd order were fitted to the illumination-time –dependent absorption spectra to test for degradation that should happen according 1st order kinetics. While the reaction to dimers containing two molecules should show 2nd order kinetics. An investigation of the linearization of the 1st order kinetic, which does not give a straight line, makes the explanation of simple degradation of the molecules less probable. Also the linearization of the 2nd order kinetics model does not give a straight line, hence this simple model of dimerization does also not explain our data. Since a step growth model was already applied for similar photo aggregation processes[58], this model was fitted to the data. The fit shows an excellent reproduction of the experimental data. By varying the concentration we found that the photo-driven process is much faster with a higher concentration. This behavior could be assumed for a photo-driven aggregation or any other reaction needing more than one molecule to occur, but not for a simple disassembly of the molecules. Despite the simple use of the absorbance of one wavelength to determine the concentration and kinetics the 2D-matrix of absorbance over wavelength and illumination was put into a singular value decomposition (SVD) analysis. This analysis yields the significant spectral components of the change of the absorbance and the kinetics of the respective component.[94] This analysis gives basically three significant components (C1, C2 and C3), where the first one resembles the constant final spectra, the second one the main changes during the illumination and the third one gives some early time intermediate with low impact at the beginning of the experiment and no impact for larger illumination times. Hence the kinetic of C2 was used to fit the step growth model also applied to the simple absorbance at a particular wavelength. This fit gives very similar parameters as by using a single wavelength and hence the step growth model seems to apply.

A further hint towards a photo-aggregation was found by measuring particle sizes by dynamic light scattering (DLS). Here we observe that the number of particles is rising after illumination, while the mean particle size is decreasing slightly. Once the photoreaction is done, it was not possible to regain the monomeric species by *e.g.* more polar solvents or elevated temperature. Hence the created species have to have a high binding energy. This would also include dimers being covalently bonded. [213]

To find possible aggregate structures we identified thermodynamically favorable aggregates by using the program EnergyScan[214], which allows for identifying geometrical diverse aggregate structures. The dimers with the highest binding energy show a strong hydrogen bond between the carboxylic acid groups or between the carboxylic acid and the cyano group of the α cyano carboxylic acid moiety. The calculated binding energies were in the range of 400 to 1100 meV and hence far above the thermal energy at room temperature. Hence these dimers once formed, will hardly disassemble in solutions once they are formed. This fits pretty well to the missing reversibility that was observed. Also these kinds of dimers could act as a precursor for covalent bonds at the electron accepting α-cyano carboxylic acid moiety.[59]

Focusing on the solid state films different preparation methods were applied to identify the effect of different morphologies on the optical parameters. As reference, two different preparation methods to obtain more amorphous structures were used, drop- and spin-coating. With these methods mixed disordered morphologies were obtained having quite different optical properties as determined by UV-vis spectroscopy. The differences in morphology were

determined with atomic force microscopy. To get tunable morphologies the Langmuir-Blodgett (LB) technique was applied. Here it was found that many of the fully organic DSSCs dyes have a molecular structure, which is well suited for the use in the LB-technique. They show an amphiphilicity due to the hydrophilic cyano-carboxylic acid group at one end and the hydrophobic chromophore on the other side. Hence, these molecular structures together with the LB-technique enabled the investigation of different aggregate structures, which are fairly similar, but tunable, to the self-assembled structures at the TiO_x interface. With this method diverse morphologies were created. The achievable morphologies vary significantly with the used molecules and the applied transfer parameters. The variation of the process parameters of the films made by the LB-technique also strongly alters the optical absorption. For all molecules it was found that the lowest energy optical transition shows a decrease in absorption upon going from solution to solid state LB-films, in comparison to the second absorption found in the blue spectral region. This is also very similar to the effect found in the photo-aggregated molecules in solution.[95] This was one of the first indications for photo-aggregation rather than photo-degradation.

The influence on the optical properties of the varied surface pressure at which the LB-films were transferred is rather different for the three used molecules. The shortest molecule **D2A** shows the lowest absorption in the low energy transition for small surface pressures and an increase in this absorption for higher surface pressures as compared to **D3A** and **D4A**. This seems to be counterintuitive, since an increased crystallinity was suspected for higher surface pressures, but, by taking a closer look onto the morphology determined by AFM, one could clearly see that for higher surface pressures the disorder is increased. This is due to a partial collapse of the first monolayer on the LB-trough before transferring the monolayer onto the substrate. This collapse point was found in the isothermal curve and is only a few mN/m above the used surface pressure at the film-transfer. For the longer molecule **D3A** the trend of the absorption of the lowest energy transition is similar to **D2A**, while the formed morphologies are much more diverse. All LB-films made of **D3A** and **D4A** are transferred far below the collapse point of the isothermal curve. The LB-films are relatively flat but show additionall roundish particles for low and very high surface pressures. For the medium high surface pressure structures made of several sheets with a thickness of two molecule length (~2x2.5 nm=5 nm) are found. This indicates a structure like AN or AA, introduced in Chapter 3.2, having a hydrogen bond either between the carboxylic acid groups or in between the carboxylic acid and amine moieties of adjacent molecules. Despite this it also looks like a very small picture made by Picasso. For **D4A**, the molecules with the longest π-bridge, the effect of aggregation on the optical absorption is most pronounced. It could be clearly shown that the lowest energy transition nearly vanishes upon increased surface pressure at the LB-film transfer. Here the dominant morphology consists of fiber-like structures, which grow in size with increased surface pressure at the film transfer.

To study the influence of supramolecular structure on the processes right after photoexcitation steady state fluorescence measurements were performed. To measure even smallest fluorescence signals from solutions and thin films, a versatile and highly sensitive fluorescence setup was build and optimized. With this setup it is possible to measure even weakest emissions from thin films,[215] solutions,[216] vesicles[217] and even Langmuir monolayers on a water surface.[166] The determined fluorescence quantum yields revealed a strong influence of concentration and the used excitation wavelength in solution. For thin LB-films a complete quenching of

fluorescence in was found. By changing from solution to the solid state, it turned out that basically no fluorescence could be measured. Hence the aggregation causes new and efficient recombination channels.

Those recombination channels have been investigated using transient absorption spectroscopy in the femtosecond to nanosecond time regime. From the solution experiments in chloroforme and the more polar DMSO we found that the excited state has a strong intramolecular charge transfer (ICT) character. Starting from the relatively large shifts in the excited state absorptions (ESA) peaks, the transient absorption data cannot be described well by fitting with the normally used multi-exponential fit routine. Furthermore, a large number of different species and kinetics was found to describe the transient absorption data, especially by exciting at the dimeric transitions. A spectral and temporal overlap of different transient absorption features like ground state bleach (GSB), stimulated emission (SE) and ESA was also complicating the data analysis. While the structures of the molecules **D3A** and **D4A** are very similar, their photo-induced kinetics in solution are fairly different. While for **D3A** in solution the recombination to the ground state (GS) is completed within roughly 300 ps, the longer **D4A** shows a long living component with lifetimes above 2 ns. The observation of a long living excited state in **D4A** is most probably caused by an inter-molecular charge transfer or dimer state, which acts as a precursor for the photo-dimerization or aggregation found in the first Chapter. This would also explain the higher rate constant for photo-aggregation of **D4A** in comparison to **D3A** discussed in Chapter 3. At very short delay times we find a cooling process, which leads to small ESA peak shifts for **D3A**, while the shifts are much more pronounced in the case of **D4A**. This means that the intramolecular charge transfer state (ICT), which was concluded from the theory and the faster recombination in the more polar DMSO, is much better stabilized for the longer **D4A** in comparison to **D3A**.

Furthermore, some short lived intermediates were found for **D3A** and more pronounced for **D4A**, which are by now not fully understood. Because the effect of different morphologies on the kinetics after photoexcitation is a crucial part to understand the effect of aggregation on the device performance, the focus was set on the comparison of kinetics in solution and on different solid state morphologies. Here we find that thin films with different morphologies give fairly different recombination kinetics. Hence, the energetical landscape is significantly changed upon supramolecular structure variation. In contrast to the recombination in the less polar chloroforme the recombination is fast for **D3A** and **D4A** as found by the 1/e-decay time of the NIR ESA feature. Especially for **D3A** are significantly influenced by the morphology. Here the general trend is that the recombination is faster, if the molecules are more ordered. Especially if they are forced into a parallel arrangement by the Langmuir-Blodgett technique a drastical decrease of the lifetime of the excited state was found. For the disordered thin films also a more pronounced long living state was found, indicated by an infinity component in the fit and residual signal for the longest possible delay time. Hence, in this disordered morphology intermolecular charge separated states are populated after photoexcitation.

For a deeper insight into the processes of photo-aggregation different measurements in matrices or aggregation inhibitors has to be performed in a follow-up work. Also the exciton dissociation and recombination on TiO_x or within a bilayer system with an acceptor molecule like $PC_{60}BM$ should be researched to fully determine the impact of aggregation on device

performance in photovoltaic cells. Since the photo-aggregation or degradation processes of this kind of molecules is still not completely proven more work has to be done to get a proof for the exact reaction pathway.

Finally, in the thesis at hand I could highlight the impact of supramolecular structure on absorption and emission spectra as well as on the excited state kinetics. For this research we have focused on merocyanine dyes, which were well investigated in solution, but lacking a comprehensive understanding on how to broadly tuning the the supramolecular structure and their influence on optical and electronical properties as well as excited state dinyamics. We found that theformationextended 2D-layers was only possible with the medium sized merocyanine **D3A** and all of these dyes strongly tend to 3D-self aggregation. Nevertheless, we succeeded for D3A to systematically tune the supramolecular structure towards H-aggregates by means of depositing Langmuir layers at increasing surface pressures. The accompanied increase in supramolecular order leads to creation of efficient dark deactivation channels, what explains the lower power conversion efficiency by dye aggregation in a DSSC device.

7 Zusammenfassung

Aggregation und Intermolekulare Wechselwirkungen spielen eine wesentliche Rolle in den grundlegenden Prozessen in organischen Solarzellen und anderen opto-elektronischen Bauteilen aus organischen Molekülen. Aggregation ist in organischen Bulk-Heterojunction (BHJ) Solarzellen normalerweise förderlich für eine hohe Effizienz. Fehlende Aggregation oder unvorteilhafte Anordnung von Molekülen im Bauelement sind einer der wesentlichen limitierenden Faktoren für effiziente Solarzellen. [170, 197-201] Im Gegensatz dazu ist Aggregation zwischen Molekülen bei Farbstoffsolarzellen (DSSCs) einer der Hauptursachen für schlechte Solarzelleffizienz.[31, 32] Die Forschung auf dem Gebiet der Morphologie und Aggregation von Molekülen für BHJ Solarzellen sind bereits sehr weit fortgeschritten, was an der großen Auswahl an Veröffentlichungen zu diesem Thema abzulesen ist. Selbst bei einer einfache Suche nach den Schlagworten *„Morphology“* und dem am besten Untersuchten Donorpolymer für BHJ Solarzellen, *„P3HT“* (Poly(3-hexylthiophen)), wurden über „Web of Knowledge“ bereits mehr als 2700 Artikel gefunden. Für Farbstoffe, welche in Farbstoffsolarzellen eingesetzt werden ist die Anzahl an Veröffentlichungen zum Thema Aggregation und intermolekularen Wechselwirkungen deutlich kleiner. Der Fokus wurde in den bekannten Veröffentlichung im Wesentlichen auf die Effizienzverringerung durch Aggregation gelegt[41, 206, 207] und wie man diese durch z.B. geeignete Aggregationsinhibitoren unterdrücken kann.[35, 37, 57] Um den Effekt der gebildetten Aggregate auf die optoelektronischen Eigenschaften von Farbstoffen näher zu untersuchen bietet es sich an Modellsysteme aus ähnlichen Molekülen herzustellen und deren Eigenschaften mit denen von einzelnen Molekülen in Lösung zu vergleichen. Diese Modellsystem bestehen aus dünnen Filmen, in denen, durch geeigente Probenpräparation, die Moleküle in unterschiedlichen intermolekularen Anordnungen gezwungen werden. Mit diesen Modellsystemen ist es möglich die Auswirkung der verschiedenen Aggregatstrukturen auf Absorption, Emission und Rekombinationskinetiken zu untersuchen.

Um die Aggregatstrukturen und Morphologie zu kontrollieren, werden typischerweise die Prozessparamter bei der Dünnfilmherstellung *via* Dropcasting (DC) oder Spincasting (SC) variiert.[27, 76] Alternativ kann über die Einführung von verschiedenen Seitenketten an den Molekülen auch die Morphologie, inbesonder bei BHJ Solarzellen, gesteuert werden.[173] Mit diesen Methoden werden Aggregatstrukturen hergestellt, welche über nicht Gleichgewichtsthermodynamik beim Trocknen aus der Lösung erreicht werden. Das Ergebnis davon sind typischerweise stark heterogene lokale Aggregatstrukturen, welche z.B. aus kristallinen und amorphen Regionen in unterschiedlichen Verteilungen und Größen bestehen.[6, 158, 208] Als komplementäre Technik zu DC und SC wird die Langmuir-Blodgett Technik[60] verwendet, welche es ermöglicht definierte und variable supramolekulare Strukturen herzustellen. Dies wird ermöglicht indem man die Parameter der Monolage der Moleküle auf der Wasseroberfläche des LB-Trogs beim Transfer auf das feste Substrat variiert. Für die LB-Technik eignen sich insbesondere amphiphile Moleküle. Diese wird bei organischen Farbstoffen, die für die Anwendung in DSSCs synthetisiert wurden, über das meist hydrophobe Chromophor in Verbindung mit einer hydrophilen Ankergruppe realisiert. Die Ankergruppe besteht typischerweise aus Carbonsäuren, welche sehr gut an TiO_x binden.[43] Deshalb eignen sich gerade diese DSSC Farbstoffe für die LB-Technik. Des Weiteren werden über die LB-Technik auch gerade

die supramolekularen Strukturen erzeugt bei denen die Moleküle ähnlich wie bei DSSCs ausgerichtet sind, also jeweils die hydrophilen und hydrophoben Teile nebeneinander sind. Das entspricht dann auch der Ausrichtung, die in DSSCs zu erwarten ist, bei denen die Ankergruppen jeweils auf dem TiO_x gebunden sind. In dieser Arbeit wurden deshalb die DSSC Farbstoffe **D3A** und **D4A** verwendet, welche in der AG Beckert synthetisiert wurden. [71] Des Weiteren wurde ein ähnlicher Farbstoff mit einem kürzeren Chromophor verwendet, welche von der Würthner Gruppe bezogen wurde. Alle hier verwendeten Farbstoffe sind nach dem weit verbreiteten Donor-π-Brücke-Akzeptor Prinzip aufgebaut.[43] Der Vergleich der Farbstoffe zeigt, dass im Wesentlichen die π-Brückenlänge und in geringerem Maße deren Aufbau, variiert wird. Die Akzeptor- und Ankergruppe ist gleich und die Donorgruppe ist ähnlich. Deshalb eignen sich diese Moleküle, um den Einfluss der π-Brückenlänge und dessen Aufbau auf Aggregation und dessen Einfluss auf die optischen und elektronischen Eigenschaften zu untersuchen. Der Effekt der Aggregatbildung von DSSC relevanten Farbstoffen wurde bisher hauptsächlich in Bezug auf Solarzelleffizienz untersucht, wie z.B. bei Merocyanin 540. [209] Für die hier verwendeten Moleküle **D3A** und **D4A** wurden bereits der Effekt von Aggregationshemmern auf die Solarzelleffizienz untersucht.[71] Detailierte Studien über die Struktur von Aggregaten aus DSSC-relevanten Farbstoffen sind jedoch kaum zu finden.[30]

Um den Einfluss der Aggregation auf die optischen Eigenschaften von Molekülen zu untersuchen wurden zunächst die Eigenschaften von einzelnen Molekülen in Lösung als Referenz untersucht. Als nächster Schritt wurden, wie in vielen anderen Arbeiten über Aggregatebildung auch,[44, 130] konzentrationsabhängige Extinktionskoeffizienten und Fluoreszenzquantenausbeuten bestimmt. In den hier genutzten Lösungsmitteln Chloroform und Tetrahydrofuran (THF) sind sowohl der Extinktionskoeffizient als auch die Fluoreszenzquantenausbeute, bereits im mM Bereich, konzentrationsabhängig sind. Dies sind starke Indizien für Aggregate in Lösung.[44] Ausgehend von der Literatur sind typischerweise zwei Arten von Aggregaten beschrieben: H- und J-Aggregate.[44, 47] Wärend J-Aggregate, benannt nach E.E. Jelley[46], eine schmallbandige rot verschobene Absorptionsbande zeigen ist die Absorption von H-Aggregaten, abgeleitet von hypsochrom (blau) gegenüber der Monomerabsorption verschoben.[210] Für die hier untersuchten Moleküle ist die Zuordnung nicht so trivial, weil im Wesentlichen die Monomerabsorption bei steigender Konzentration Intensität verliert, während die Aggregatabsorption nur wenig an Intensität gewinnt. Insbesondere im Vergleich zur Literatur ist die Zunahme der Aggregatabsorption im Vergleich zur Abnahme der Monomerabsorption schwach ausgeprägt.[49, 129, 139] Die Neigung zur Aggregatbildung von Molekülen, insbesondere von Farbstoffen, ist stets bedingt durch die Struktur dieser. Das heißt, dass gerade flache Moleküle dazu neigen Aggregate über ππ-stacking oder Dipol-Dipol-Wechselwirkung zu bilden.[44, 139, 218] Dies wurde bereits für verschiedene Moleküle wie Cyaninfarbstoffe, Squarine, Porphyrine oder Perylene gezeigt, wobei neben der Grundstruktur auch die jeweilige Funktionalisierung einen wesentlichen Einfluss auf die Aggregatbildung gezeigt haben.[44] Aber gerade für die DSSC relevanten Farbstoffe wurde eine bereits in Lösung vorhandenen Aggregation bisher nicht untersucht, was dementsprechend auch für die hier verwendeten Farbstoffe gilt.

Neben der hier bestimmten Konzentrationsabhängigkeit der Extinktionskoeffizienten zeigte sich im späteren Verlauf der Experimente, dass die Beleuchtung der Lösungen mit Licht hohe Intensität die Extinktion der Lösung in einer ähnlichen Weise verändert. Diese Veränderung der Extinktion mittels Beleuchtung war aber deutlich effizienter als eine reine

Konzentrationserhöhung. Um diesen Effekt zu quantifizieren wurde zunächst eine Automatisierungsroutine für die UV-vis Transmissionsmessungen mittels Labview geschrieben. Dieses Programm übernimmt die komplette Steuerung des Spektrometers und der LED-Beleuchtungseinheit und ermöglich damit reproduzierbare Messungen mit exakt gleichen Beleuchtungs- und Messintervallen. Da nur für die Beleuchtungseinheit Labview Treiber vorhanden waren, musste das Spektrometer direkt über Hardwarebefehle gesteuert und die Daten ausgelesen werden, was die Softwareentwicklung deutlich komplexer machte. Mit dem hier generierten 2D-Datensatz aus Absorbanzspektren nach unterschiedlicher Beleuchtungszeit wurden die weiteren Kinetikanalysen durchgeführt. Grundsätzlich können die hier gemessenen Veränderungen der Absorbanz zwei Ursachen haben: Zum einen könnte es sich um eine photoinduzierte Aggregation oder eine Degradation der Farbstoffe handeln. Beispiele für Photoaggregation und die Ausbildung von H- und J-Aggregaten unter Bestrahlung mit Licht wurden von Petrenko *et al.*[58] und Chibisov *et al.*[152, 211] bereits für Merocyanin-Farbstoffe gezeigt. Neben der Ausbildung von schwach gebundenen Aggregaten wurde auch eine photoinduzierte Ausbildung von kovalent gebundenen Aggregaten beobachtet. [59] Diese ist insbesondere dann stark ausgeprägt, wenn die Moleküle bereits vor der Bestrahlung dicht gepackt waren.[59] Aber auch eine Photodegradation wurde für Merocyanin-Farbstoffe bereits gezeigt, wobei typischerweise die Polymethinbrücke als Schwachpunkt identifiziert wurde.[212] Für Moleküle die einen ähnlichen Aufbau wie die hier verwendeten haben, wurden bisher keine Veröffentlichungen gefunden, die einen der vorher genannten Prozess beschreiben. In Verbindung mit einer sehr limitierten Menge an Ausgangsmaterial gestaltet sich die Differenzierung zwischen den möglichen Prozessen als Herausforderung. Zunächst wurden versucht die Datensätze aus den beleuchtungszeitabhängigen Extinktionen mit einem Modell für Reaktionen erster und zweiter Ordnung zu beschrieben. Es ist hier zu erwarten, dass eine einfache Degradation einer Reaktion erster Ordnung folgt und eine Dimerbildung einer Reaktion zweiten Ordnung. Ein erster Test, bei dem die Extinktion bei der Wellenlänge des Maximums der S_0 zu S_1 Monomer Absorptionsbande über der Beleuchtungszeit gegenüber erster und zweiter Reaktionsordnung linearisiert wurde, zeigte weder für erste noch für zweite Ordnung eine gute Übereinstimmung. Dementsprechend scheint sowohl eine Degradation als auch eine einfache Dimerbildung unwahrscheinlich. Die Daten lassen sich aber sehr gut mit einer gestreckten Exponentialfunktion beschreiben, welche bereits in der Literatur für ein Stufenwachstum von Photoaggregaten genutzt wurde.[58] Durch eine Erhöhung der Konzentration in Lösung konnte eine Steigerung der Reaktionsgeschwindigkeit erreicht werden, was wiederum auf eine Dimerisierung oder andere dimolekulare Reaktion schließen lässt. Zur besseren Beschreibung der beleuchtungszeitabzhängigen Extinktionen wurde der 2D-Datensatz mittels einer Singulärwertzerlegung (SVD) analysiert.[94] Damit konnte der Datensatz in drei Wesentliche spektrale Komponenten, C1,C2 und C3 und deren Kinetiken zerlegt werden. Wobei sich zeigte, dass die Kinetik im Wesentlichen zeitlich Konstant war und die spektrale Form von C1 im Wesentlichen das Startspektrum darstellt. Die Komponente C2 liefert hier nahezu vollständig die Änderung der Spektren und die dazugehörige Kinetik lässt sich mit der gleichen gestreckten Exponentialfunktion beschreiben, wie die Kinetiken bei Verwendung einer Wellenlänge.

Neben der Kinetik der Extinktionsänderungen wurden auch Partikelgrößenmessungen zum Nachweis der Photoaggregationsthese durchgeführt. Diese zeigten, dass sich für **D4A** in Chloroform die Partikelanzahl unter Bestrahlung erhöhte, während sich die Größe der Partikel

leicht verringerte. Nachdem die Photoaggregation abgeschlossen ist, war es nicht möglich die gebildeten Strukturen wieder in Monomere zu zersetzen. Weder durch sehr polare Lösemittel noch durch Temperaturerhöhung konnte eine Reversibilität der Photoreaktion gezeigt werden. Die hier erzeugten Aggregate müssen also eine sehr hohe Bindungsenergie haben, was explizit auch kovalent gebundene Dimere mit einschließt.[213]

Um mögliche, energetisch vorteilhafte, Aggregatstrukturen zu finden wurde das Programm EnergyScan[214] verwendet. Dieses ermöglicht unter der Eingabe der Startgeometrie von Molekülen eine Vielzahl von unterschiedlichen, energetisch vorteilhaften Dimergeometrien zu berechnen. Die Dimere mit hoher Bindungsenergie, die mittels EnergyScan gefunden wurden, zeigen alle eine Wasserstoffbrückenbindung zwischen den einzelnen Carbonsäuregruppen oder zwischen der Carbonsäuregruppe und der Cyanogruppe des α-Cyanocarbonsäureeinheit. Die berechneten Bindungsenergien sind dabei typischerweise im Bereich von 400 bis 1100 meV und damit deutlich größer als die thermische Energie bei Raumtemperatur (25 meV). Dementsprechend sollten diese Dimere, wenn sie den einmal gebildet wurden, schwer zu trennen sein. Dies würde auch die fehlende Reversibilität der Photaggregation erklären. Des Weiteren könnten solche Dimere auch als Vorstufe zu kovalenten Bindungen zwischen den α Cyanocarbonsäureeinheiten dienen, was bereits für die α-Cyano-4-hydroxyzimtsäure gezeigt wurde.[59]

Beim Übergang von Molekülen und kleinen Aggregaten in Lösung zu Festkörpern und im Speziellen zu dünnen Filmen, spielen intermolekulare Strukturen eine wesentliche Rolle für die elektronischen und optischen Eigenschaften. Zur Untersuchung der Effekte der lokalen intermolekularen Strukturen wurden verschiedene Präparationsmethoden verwendet. Um amorphe, ungeordnete Referenzstrukturen zu erhalten, wurden Schleuderbeschichtung (Spincasting-SC) und Dropcasting (DC) verwendet. Die optischen Eigenschaften dieser zeigten bereits mittels Absorptionsspektroskopie deutliche Unterschiede zu den Lösungsspektren und auch zwischen DC- und SC-Filmen. Die Morphologie wurde standardmäßig mittels Atomkraftmikroskopie (AFM) untersucht. Um Filme mit einer steuerbaren Morphologie zu erhalten, wurde die Langmuir-Blodgett (LB) Technik verwendet.[60] Dabei hat sich herausgestellt, dass gerade die organischen Farbstoffe für Farbstoffsolarzellen (DSSCs) sich sehr gut für die LB-Technik eignen. Die für die LB-Technik notwendige Wasserunlösslichkeit wird durch das hydrophobe Chromophor gewährleistet, während die hydrophile Ankergruppe aus Cyano-Carbonsäure für eine bessere Morphologiekontrolle durch eine eingeführte Amphiphilie sorgt. Durch die Amphiphilie werden die möglichen Aggregatstrukturen eingegrenzt, sodass sich die Moleküle auf der Wasseroberfläche des LB-Trogs jetzt nur parallel ausrichten können. Dies entspricht auch der wahrscheinlichen Ausrichtung der Moleküle auf der TiO_x-Oberfläche einer Farbstoffsolarzelle. Durch die Variation der Komprimierung der Moleküle auf dem LB-Trog konnten im Anschluss dünne Filme mit verschiedenen Morphologien erzeugt werden, die sich deutlich von den amorphen SC- und DC-Filmen unterscheiden. Die optischen Eigenschaften, in diesem Fall die Absorption, der LB-Filme konnten dabei deutlich durch den gewählten Oberflächendruck variiert werden. Es hat sich gezeigt, dass bei allen hier untersuchten Molekülen die Absorption im Bereich des S_0 zu S_1 Übergangs für hoch geordnete Filme verringert wird und dafür die Absorption in der nächst höherenergetischen Absorptionsbande erhöht wird. Diese Umverteilung von Absorption aus dem S_0 zu S_1 Übergang zum nächsten blau verschobenen

Übergang ist ähnlich der für photoaggregierte Lösungen.[95] Dies ist ein weiteres Indiz, dass es sich eher um Photoaggregation als um Photodegradation der Moleküle handelt.

Durch Variation des Oberflächendrucks beim Transfer der Langmuir-Filme auf die festen Substrate konnten, in Abhängigkeit der verschiedenen hier verwendeten Moleküle, sehr unterschiedliche Effekte auf die Absorption der LB-Filme beobachtet werden. Für das kleinste Molekül **D2A** wurde für kleine Oberflächendrücke eine deutliche Reduzierung der Absorption in der S_0 zu S_1 Bande gefunden. Bei einer Erhöhung des Oberflächendrucks bei der Abscheidung zu Werten nahe dem Kollapspunkt erhöhte sich jedoch die Absorption dieser Bande. Dies konnte durch den Vergleich der AFM Bilder auf eine sehr vielfältige Morphologie, bestehend aus unterschiedlichen lokalen Strukturen, zurückgeführt werden. Dies wird durch einen partiellen Kollaps der ersten Monolage beim Transfer auf das Substrat verursacht. Da für die längeren Moleküle **D3A** und **D4A** deutlich höhere Oberflächendrücke erreicht werden, konnten alle Proben deutlich unterhalb des Kollapspunktes übertragen werden. Dies sollte zu gleichmäßigeren Morphologien der Filme nach dem Transfer auf das Substrat führen. Für das etwas längere Molekül **D3A** ist der Trend der S_0 zu S_1 Absorptionsbande mit steigendem Oberflächendruck ähnlich wie bei **D2A**, aber die AFM-Messungen zeigen deutlichere Unterschiede der lokalen Morphologien. Diese variiert von relativ glatten Filmen, bestehend aus kleinen runden Bereichen, bei niedrigen und hohen Oberflächendrücken zu Schichtstrukturen, welche die Dicke von zwei Moleküllängen haben (~2x2,5 nm=5 nm), bei mittleren Oberflächendrücken. Diese Doppellage würde gerade auf die in Kapitel 3.2 mittels Theorie gefundenen Dimerstrukturen AN oder AA hinweisen, welche sich durch eine Wasserstoffbrückenbindung zwischen den Carbonsäuregruppen auszeichnen. Gerade diese Morphologie liefert auch ein AFM Bild, welches auch aus der Hand von Picasso stammen könnte, nur in sehr viel kleinerem Maßstab. Für das Molekül mit der längsten π-Brücke **D4A** ist der Einfluss der Morphologie auf die optische Absorption am größten. Hier konnte, ähnlich wie für den Fall der Photoaggregation in Kapitel 3, ein nahezu vollständiges Verschwinden der S_0 zu S_1 Absorption beobachtet werden. Die Morphologie, welche mittels AFM bestimmt wurde, besteht hier im Wesentlichen aus faserartigen Strukturen, welche in ihrer Größe mit höherem Oberflächendruck zunehmen. Diese Strukturen könnten, im Vergleich zu Kapitel 3, zum Beispiel aus ANπ Dimeren bestehen, welche ein Kettenwachstum zulassen. Ein Beispiel aus sechs **D3A** Molekülen ist im Anhang in Figure A 2 abgebildet, wobei **D4A** sich, ausgerichtet durch die Wasserstoffbrückenbindung zwischen Cyano- und Carbonsäuregruppe, ähnlich anordnen sollte. Gerade für **D4A** hat sich auch gezeigt, dass verschiedene Morphologien auch über klassische Beschichtungsverfahren wie z.B. Spincoating erzeugen lassen. Des Weiteren konnte auch ein höherer Grad an Ordnung, zu sehen am graduellen verschwinden der S_0 zu S_1 Absorptionsbande, durch eine thermische Nachbehandlung erzielt werden.

Neben dem Einfluss der Morphologie auf die Absorption wurde auch der Effekt auf die Prozesse nach der Photoanregung untersucht. Als erster Schritt wurde die Fluoreszenz mittels eines dafür selbst konzipiert, aufgebaut und auf maximale Sensitivität optimierten Fluoreszenzmessplatzes gemessen. Mit diesem Aufbau ist es möglich auch kleinste Emissionen von dünnen Filmen,[215, 219] Lösungen,[216] Vesikeln[217] und Langmuir-Monolagen auf der Wasseroberfläche[166] zu messen. Aus der Messung der Fluoreszenz von Lösungen in Abhängigkeit von der Konzentration und der Anregungswellenlänge (405 nm und 532 nm) wurden die Fluoreszenzquantenausbeuten berechnet. Dabei hat sich gezeigt, dass zum einen mit steigender Konzentration die

Quantenausbeute sinkt und zum anderen die Quantenausbeute bei Anregung der S_0 zu S_1 Absorptionsbande mit 532 nm um ein Vielfaches höher ist als bei Anregung der Aggregatbande mit 405 nm. Beim Übergang zu LB-Filmen zeigt sich dann, dass die Fluoreszenz vollständig gelöscht wird. Beim Übergang zum hochgeordneten Festkörper werden also neue effiziente und dunkle Rekombinationskanäle eröffnet, welche eine schnelle Deaktivierung zum Grundzustand ermöglichen. Eine andere Erklärung wäre die Formation von intermolekularen ladungsgetrennten Zuständen (CT-States), welche zwar langlebig sind, aber keine Fluoreszenz zeigen.

Da die Kinetiken nach Photoanregung typischerweise im Femto- bis Nanosekunden Zeitfenster ablaufen, wurde die entsprechende ultraschnelle transiente Absorptionsspektroskopie (fs-TA) eingesetzt. Auch für die fs-TA Spektroskopie wurden zunächst Lösungen vermessen, um die Eigenschaften von einzelnen Molekülen bzw. kleinen Aggregaten in Lösung zu untersuchen. Dabei wurde neben Chloroform auch das deutlich polarere DMSO verwendet. Durch die Variation der Polarität konnte festgestellt werden, dass der angeregte Zustand sowohl in **D3A** als auch in **D4A**, einen starken intramolekularen Ladungstransfercharakter (ICT) hat. Die Datenanalyse der Messungen in Lösung war für beide Moleküle herausfordernd, da viele Signaturen wie Grundzustandsbleichung (GSB), stimulierte Emission (SE) und angeregte Zustandsabsorption (ESA) sich sowohl temporär als auch spektral überlagerten. Für eine bessere Vergleichbarkeit, der sehr unterschiedlichen spektralen Signaturen der angeregten Zustände wurde in diesem Fall mittlere Lebenszeit, also der Abfall auf 1/e, der ESA im Bereich zwischen 700 und 750 nm verwendet. Die Moleküle **D3A** und **D4A** sind zwar strukturell sehr ähnlich, zeigen aber sehr unterschiedliche transiente Kinetiken in Lösung. Während für **D3A** in Chloroform die Rekombination in den Grundzustand nach Photoanregung bereits nach etwa 300 ps abgeschlossen ist, zeigt das etwas längere Molekül **D4A** auch langlebige Komponenten mit einer Lebenszeit von mehr als 2 ns. Der langlebige Zustand der zu der entsprechenden ESA gehört ist vermutlich ein intermolekularer Ladungstransfer- oder Dimerzustand. Dieser könnte auch als Vorstufe zu den bereits in Kapitel 3 beschriebenen Photoaggregaten dienen. Das würde wiederum die höhere Photoreaktionsrate von **D4A** im Vergleich zu **D3A** erklären. Schaut man sich nun weiter die TA-Daten kurz nach der Photoanregung an und dabei insbesondere den Zeitbereich bis etwa Zehn ps, ist zunächst ein Cooling Prozess zu erkennen, welcher sich durch eine Blauverschiebung der ESA-Signale kennzeichnet. Vergleicht man die Kinetiken des Cooling, welche durch fitten des ESA-Peaks für alle Verzögerungszeiten mittels selbstgeschriebener, automatischer Labview-Routine erhalten wurden, für **D3A** und **D4A** fällt zunächst auf das die absolute energetische Verschiebung für **D3A** deutlich kleiner ausfällt als für **D4A**. Das bedeutet, dass der ICT-Zustand für **D4A**, welcher aus der schnelleren Rekombination im polareren DMSO und aus der Theorie gefolgert wurde, energetisch deutlich mehr abgesenkt wird. Dies lässt auf eine stärkere geometrische Relaxation oder größere Stabilisierung des ICT-Zustands für **D4A** im Vergleich zu **D3A** schließen. Die weiteren Prozesse und die darin involvierten kurzlebigen Zwischenzustände konnten im Rahmen dieser Arbeit nicht abschließend geklärt werden.

Da hier aber der Einfluss verschiedener Morphologien im Festkörper im Mittelpunkt steht, wurde sich auf die Änderungen der TA-Kinetiken beim Übergang vom Molekül in Lösung zu verschiedenen Festkörper-Morphologien konzentriert. Dabei hat sich gezeigt, dass verschiedene Morphologien zum einen sehr unterschiedliche Kinetiken zeigen und auch die spektralen Signaturen sich signifikant ändern. Das bedeutet, dass die energetische Landschaft sehr stark

von der Morphologie abhängt und damit auch die elektrooptischen Eigenschaften. Betrachtet man die gemittelten Rekombinationszeiten (1/e) der spektralen ESA-Signaturen im Bereich des NIR, sieht man, dass die Rekombination von Filmen aus **D3A** und **D4A** im Vergleich zur Lösung zunächst deutlich schneller erfolgt. Insbesondere für **D3A** konnte eine signifikante Reduktion der Lebenszeit ausgehen von Lösung über einen ungeordneten DC Film hin zum hochgeordneten LB-Film beobachtet werden. Dabei reduzierte sich die gemittelte Lebenszeit von 85 ps (Chloroform - Lösung) über 50 ps (DC-Film) zu 6 ps (LB-Film). Wenn die Moleküle in eine parallele Anordnung gezwungen werden, wie hier mit der LB-Technik oder wie es für DSSCs zu erwarten wäre, werden neue ultraschnelle Rekombinationskanäle erzeugt. Dies erklärt auch, warum die Effizienz von DSSCs aus **D3A** und **D4A** unter Verwendung von Aggregationshemmern, welche gerade die Dichte dieser lokalen Aggregatstrukturen reduzieren, deutlich verbessert wird.[71] Bei sehr ungeordneten Strukturen, wie z.B. bei der Verwendung der SC oder DC Technik zur Filmpräparation, von **D3A** ergibt sich ein anderes Bild: Die SC-Filme mit der wahrscheinlich höchsten Unordnung, zeigen zum einen eine leichte Erhöhung der mittleren Rekombinationszeit (100 ps) im Vergleich zur Chloroform Lösung (85 ps) und zum anderen gibt es eine langlebige Komponente, welche zu einem Zustand gehört der auch nach 2 ps noch nicht rekombiniert ist. Diese kann einem intermolekularen Ladungstransferzustand zugeordnet werden und ist sowohl für SC- als auch für DC-Filme vorhanden. Generell konnte der Trend zu deutlich verkürzten Lebenszeiten der angeregten Zustände in verschiedenen Festkörpern auch für **D4A** bestätigt werden. Im Falle von **D4A** sind die Lebenszeiten aber bereits im DC-Film von 400 ps (Chloroform -Lösung) auf 10 ps gesunken um im hochgeordneten LB-Film noch weiter auf 7 ps abzusinken. Auch hier gibt es für den DC-Film eine langlebige Komponente, welche auch hier wahrscheinlich einem intermolekularen Ladungstransferzustand zugeordnet werden kann, welcher aber nicht für den hochgeordneten LB-Film gefunden wurde.

Für die hier untersuchten Moleküle zeigt sich, dass die Aggregatstrukturen, welche mittels LB-Technik erzeugt wurden, die Rekombinationsraten deutlich erhöht werden. Des Weiteren ist die Absorption im Bereich des sichtbaren Lichts reduziert, was gerade für **D4A**, eine weitere signifikante Reduktion der DSSC Effizienz zur Folge hat.[71]

Um die Photoaggregation, deren Kinetiken und eventuell vorhandene Photoreaktionen besser zu verstehen sind weitere Untersuchungen sinnvoll. Der Effekt von Aggregationshemmern oder Matrixmolekülen auf die Photoaggregation und die ultraschnellen Prozesse nach Photoanregung sind ein weiteres Feld um weitere Einblicke in diese Prozesse zu erhalten und entsprechende Verbesserungen an z.B. DSSCs zu entwickeln.

Schlussendlich konnte ich in dieser Arbeit den signifikanten Einfluss der supramolekularen Struktur auf Absorption, Emission und die Kinetiken des angeregten Zustands zeigen. Dies wurde anhand von drei ähnlichen Merocyanin-Farbstoffen untersucht. Bei diesen waren die optischen Eigenschaften der Einzel Moleküle in Lösung bereits bekannt, aber die gezielte Erzeugung von verschiedenen supramolekularen Strukturen und deren Einfluss auf die elektronischen und optischen Eigenschaften sowie die Kinetiken nach Photoanregung wurden bisher nicht untersucht. Es zeigte sich, dass die Herstellung von definierten 2-dimensionalen (Doppel-) Schichten nur für das mittelgroße Molekül **D3A** möglich war. Für die anderen Farbstoffe wurde hier nur eine 3-dimensionale Aggregatbildung gefunden. Trotz dessen konnten mittels LB-Technik Proben hergestellt werden, welche einen systematischen Anstieg der Konzentration von

H-Aggregaten mit steigendem Oberflächendruck zeigten. Mit dem erhöhten Maß an Ordnung in der Schicht, ging aber eine steigende Anzahl an effizienten dunklen Rekombinationskanälen einher. Gerade diese effizientere Rekombination ist die wesentliche Ursache für die reduzierte DSSC Effizienz, welche den literaturbeschriebenen positiven Effekt von Aggregationshemmern auf die Solarzelleffizienz erklärt.

Bibliography

1. C. K. Chiang, C. R. Fincher, Jr., Y. W. Park, A. J. Heeger, H. Shirakawa, E. J. Louis, S. C. Gau and A. G. MacDiarmid, *Physical Review Letters*, 1977, **39**, 1098.
2. H. Shirakawa, E. J. Louis, A. G. MacDiarmid, C. K. Chiang and A. J. Heeger, *Journal of the Chemical Society, Chemical Communications*, 1977, 579.
3. R. H. Partridge, *Polymer*, 1983, **24**, 733-738.
4. V. Vohra, K. Kawashima, T. Kakara, T. Koganezawa, I. Osaka, K. Takimiya and H. Murata, *Nat Photon*, 2015, **9**, 403-408.
5. Z. He, B. Xiao, F. Liu, H. Wu, Y. Yang, S. Xiao, C. Wang, T. P. Russell and Y. Cao, *Nature Photonics*, 2015, **9**, 174-179.
6. J. A. Reinspach, Y. Diao, G. Giri, T. Sachse, K. England, Y. Zhou, C. Tassone, B. J. Worfolk, M. Presselt, M. F. Toney, S. Mannsfeld and Z. Bao, *ACS Applied Materials & Interfaces*, 2016, **8**, 1742–1751.
7. A. Salleo, *Nature Materials*, 2015, **14**, 1077-1078.
8. S. Wang, S. Fabiano, S. Himmelberger, S. Puzinas, X. Crispin, A. Salleo and M. Berggren, *Proceedings of the National Academy of Sciences*, 2015, **112**, 10599-10604.
9. J. Desilvestro, M. Gratzel, L. Kavan, J. Moser and J. Augustynski, *Journal of the American Chemical Society*, 1985, **107**, 2988-2990.
10. B. Oregan and M. Gratzel, *Nature*, 1991, **353**, 737-740.
11. S. R. Forrest, *Nature*, 2004, **428**, 911-918.
12. S. Kirchmeyer, *Translational Materials Research*, 2016, **3**, 010301.
13. R. R. Søndergaard, M. Hösel and F. C. Krebs, *Journal of Polymer Science Part B: Polymer Physics*, 2013, **51**, 16-34.
14. K. Schwetlick, *Organikum*, Wiley2009.
15. A. Hagfeldt, G. Boschloo, L. Sun, L. Kloo and H. Pettersson, *Chem Rev*, 2010, **110**, 6595-6663.
16. K. Müllen and U. Scherf, *Organic Light Emitting Devices*, Wiley-VCH, Weinheim, 2006.
17. P. Würfel, *Physik der Solarzellen*, Spektrum Akademischer Verlag2000.
18. A. Hagfeldt and M. Grätzel, *Accounts Of Chemical Research*, 2000, **33**, 269-277.
19. Y. Wu and W. Zhu, *Chemical Society Reviews*, 2013, **42**, 2039-2058.
20. H. Yersin, W. Humbs and J. Strasser, *Coordination Chemistry Reviews*, 1997, **159**, 325-358.
21. K. Kalyanasundaram and M. Grätzel, *Coordination Chemistry Reviews*, 1998, **177**, 347-414.
22. A. Arjona-Esteban, M. R. Lenze, K. Meerholz and F. Wurthner, in *Elementary Processes in Organic Photovoltaics*, ed. K. Leo2017, vol. 272, pp. 193-214.
23. J. N. Clifford, E. Martinez-Ferrero, A. Viterisi and E. Palomares, *Chemical Society Reviews*, 2011, **40**, 1635-1646.
24. X. Jiang, K. M. Karlsson, E. Gabrielsson, E. M. J. Johansson, M. Quintana, M. Karlsson, L. Sun, G. Boschloo and A. Hagfeldt, *Advanced Functional Materials*, 2011, **21**, 2944-2952.
25. J. Wiberg, T. Marinado, D. P. Hagberg, L. Sun, A. Hagfeldt and B. Albinsson, *The Journal of Physical Chemistry B*, 2010, **114**, 14358-14363.
26. A. Mishra, M. K. R. Fischer and P. Bäuerle, *Angewandte Chemie*, 2009, **121**, 2510-2536.
27. S. Engmann, V. Turkovic, G. Gobsch and H. Hoppe, *Advanced Energy Materials*, 2011, **1**, 684-689.
28. J. R. Mann, M. K. Gannon, T. C. Fitzgibbons, M. R. Detty and D. F. Watson, *The Journal of Physical Chemistry C*, 2008, **112**, 13057-13061.
29. K. R. Mulhern, M. R. Detty and D. F. Watson, *The Journal of Physical Chemistry C*, 2011, **115**, 6010-6018.
30. L. Zhang and J. M. Cole, *Journal of Materials Chemistry A*, 2017, **5**, 19541-19559.
31. C. H. Lee, S. A. Kim, M. R. Jung, K. S. Ahn, Y. S. Han and J. H. Kim, *Japanese Journal of Applied Physics*, 2014, **53**, 5.
32. M. Pastore and F. De Angelis, *Acs Nano*, 2010, **4**, 556-562.
33. F. Nüesch and M. Grätzel, *Chemical Physics*, 1995, **193**, 1-17.
34. F. Nuesch, J. E. Moser, V. Shklover and M. Gratzel, *Journal of the American Chemical Society*, 1996, **118**, 5420-5431.
35. M. Hosseinnezhad, K. Gharanjig and S. Moradian, *Mater. Technol.*, 2015, **30**, 189-192.
36. M. Hosseinnezhad, S. Moradian and K. Gharanjig, *Opto-Electron. Rev.*, 2015, **23**, 126-130.
37. J. S. Luo, Z. Q. Wan, C. Y. Jia, Y. Wang and X. C. Wu, *Electrochimica Acta*, 2016, **215**, 506-514.
38. J. S. Panicker, B. Balan, S. Soman, T. Ghosh and V. C. Nair, *Journal of Chemical Sciences*, 2016, **128**, 101-110.
39. R. Sirohi, D. H. Kim, S. C. Yu and S. H. Lee, *Dyes and Pigments*, 2012, **92**, 1132-1137.
40. Y. Hua, S. Chang, J. He, C. Zhang, J. Zhao, T. Chen, W.-Y. Wong, W.-K. Wong and X. Zhu, *Chemistry – A European Journal*, 2014, **20**, 6300-6308.
41. S. Feng, Q. S. Li, L. N. Yang, Z. Z. Sun, T. A. Niehaus and Z. S. Li, *Journal of Power Sources*, 2015, **273**, 282-289.

42. M. W. Kryman, J. N. Nasca, D. F. Watson and M. R. Detty, *Langmuir*, 2016, **32**, 1521-1532.
43. Y. Wu, W.-H. Zhu, S. M. Zakeeruddin and M. Grätzel, *ACS Applied Materials & Interfaces*, 2015, **7**, 9307-9318.
44. F. Würthner, T. E. Kaiser and C. R. Saha-Möller, *Angewandte Chemie International Edition*, 2011, **50**, 3376-3410.
45. G. Scheibe, *Angewandte Chemie*, 1937, **50**, 212-219.
46. E. E. Jelley, *Nature*, 1937, **139**, 631-631.
47. A. Eisfeld and J. S. Briggs, *Chemical Physics*, 2006, **324**, 376-384.
48. A. Datta and S. K. Pati, *Chemical Society Reviews*, 2006, **35**, 1305-1323.
49. T. E. Kaiser, V. Stepanenko and F. Wurthner, *Journal of the American Chemical Society*, 2009, **131**, 6719-6732.
50. U. Rosch, S. Yao, R. Wortmann and F. Wurthner, *Angew Chem Int Ed Engl*, 2006, **45**, 7026-7030.
51. J. N. Israelachvili, in *Intermolecular and Surface Forces (Third Edition)*, Academic Press, San Diego2011, pp. 71-90.
52. J. N. Israelachvili, in *Intermolecular and Surface Forces (Third Edition)*, Academic Press, San Diego2011, pp. 107-132.
53. J. N. Israelachvili, in *Intermolecular and Surface Forces (Third Edition)*, Academic Press, San Diego2011, pp. 151-167.
54. S. Das, J. Preiß, J. Plentz, U. Brückner, M. von der Lühe, O. Eckardt, A. Dathe, F. H. Schacher, E. Täuscher, U. Ritter, A. Csáki, G. Andrä, B. Dietzek and M. Presselt, *Advanced Energy Materials*, 2018, **0**, 1801737.
55. D. L. Wood and J. Tauc, *Physical Review B*, 1972, **5**, 3144-&.
56. W. Shockley and W. T. Read, *Physical Review*, 1952, **87**, 835-842.
57. F. Zhang, S. R. Wang, X. G. Li, Y. Xiao and J. J. Guo, *Journal of Molecular Structure*, 2016, **1107**, 329-336.
58. V. Y. Petrenko and O. P. Dimitriev, *Chemphyschem*, 2014, **15**, 3938-3943.
59. T. Hoyer, W. Tuszynski and C. Lienau, *Chemical Physics Letters*, 2007, **443**, 107-112.
60. K. Ariga, Y. Yamauchi, T. Mori and J. P. Hill, *Advanced Materials*, 2013, **25**, 6477-6512.
61. I. Langmuir, *Journal of the American Chemical Society*, 1917, **39**, 1848-1906.
62. I. Langmuir and V. J. Schaefer, *Journal of the American Chemical Society*, 1938, **60**, 1351-1360.
63. A. Ulman, *An Introduction to Ultrathin Organic Films: From Langmuir-Blodgett to Self-assembly*, Academic Press1991.
64. S. Chakraborty, D. Bhattacharjee and S. A. Hussain, *Journal of Luminescence*, 2014, **145**, 824-831.
65. G. Zhavnerko and G. Marletta, *Materials Science and Engineering B-Advanced Functional Solid-State Materials*, 2010, **169**, 43-48.
66. N. F. de Sales and H. S. Mansur, *Materials Research-Ibero-American Journal of Materials*, 2008, **11**, 477-482.
67. A. K. Dutta, H. Lavoie, K. Ohta and C. Salesse, *Langmuir*, 1997, **13**, 801-807.
68. Y. Hamanaka, O. Kawasaki, H. Kurasawa, T. Yamauchi, Y. Mizutani, S. Kuroda and A. Nakamura, *Colloids and Surfaces A: Physicochemical and Engineering Aspects*, 2005, **257–258**, 105-109.
69. H. Tachibana, Y. Yamanaka, H. Sakai, M. Abe and M. Matsumoto, *Journal of Luminescence*, 2000, **87-9**, 800-802.
70. M. Matsumoto, T. Nakazawa, R. Azumi, H. Tachibana, Y. Yamanaka, H. Sakai and M. Abe, *The Journal of Physical Chemistry B*, 2002, **106**, 11487-11491.
71. R. Menzel, D. Ogermann, S. Kupfer, D. Weiß, H. Görls, K. Kleinermanns, L. González and R. Beckert, *Dyes Pigm.*, 2012, **94**, 512-524.
72. F. Etzold, I. A. Howard, N. Forler, A. Melnyk, D. Andrienko, M. R. Hansen and F. Laquai, *Energy & Environmental Science*, 2015, **8**, 1511-1522.
73. R. Sawada, M. Sakomura, K. Hirukawa and M. Fujihira, *Colloids and Surfaces A: Physicochemical and Engineering Aspects*, 2006, **284–285**, 448-452.
74. A. Aljarilla, C. Herrero-Ponce, P. Atienzar, S. Arrechea, P. de la Cruz, F. Langa and H. Garcia, *Tetrahedron*, 2013, **69**, 6875-6883.
75. J. R. Lakowicz, *Principles of fluorescence spectroscopy, 3rd Edition*, Springer-Verlag US2006.
76. J. A. Renz, T. Keller, M. Schneider, S. Shokhovets, K. D. Jandt, G. Gobsch and H. Hoppe, *Solar Energy Materials and Solar Cells*, 2009, **93**, 508-513.
77. S. Zhang, L. Ye, H. Zhang and J. Hou, *Materials Today*, 2016, **19**, 533-543.
78. A. Pivrikas, H. Neugebauer and N. S. Sariciftci, *Solar Energy*, 2011, **85**, 1226-1237.
79. K. B. Blodgett, *Journal of the American Chemical Society*, 1934, **56**, 495-495.
80. K. B. Blodgett, *Journal of the American Chemical Society*, 1935, **57**, 1007-1022.
81. H. S. Nalwa and A. Kakuta, *Applied Organometallic Chemistry*, 1992, **6**, 645-678.
82. M. C. Petty, *Thin Solid Films*, 1992, **210**, 417-426.
83. T. Konuma, T. Akutagawa, T. Yumoto, T. Nakamura, J. Kawamata, K. Inoue, T. Nakamura, H. Tachibana, M. Matsumoto, H. Ikegami, S. Horiuchi, H. Yamochi and G. Saito, *Thin Solid Films*, 1998, **327**, 348-352.
84. G. J. Ashwell, T. W. Walker, P. Leeson, U. W. Grummt and F. Lehmann, *Langmuir*, 1998, **14**, 1525-1527.
85. G. J. Ashwell, D. J. Zhou, R. Hamilton, K. Skjonnemand and A. Green, *Synthetic Metals*, 2001, **121**, 1455-1458.
86. T. Srikhirin, P. M. Cham, J. A. Mann and J. B. Lando, *Journal of Polymer Science Part a-Polymer Chemistry*, 1999, **37**, 1771-1779.

87. M. Parchine, J. McGrath, M. Bardosova and M. E. Pemble, *Langmuir*, 2016, **32**, 5862-5869.
88. A. Aoki, Y. Abe and T. Miyashita, *Langmuir*, 1999, **15**, 1463-1469.
89. J. Matsui, S. Yoshida, T. Mikayama, A. Aoki and T. Miyashita, *Langmuir*, 2005, **21**, 5343-5348.
90. A. Aoki and S. Fukayama, *Electrochemistry*, 2010, **78**, 178-180.
91. A. J. G. Allan, *Journal of Colloid Science*, 1958, **13**, 273-274.
92. L. Wilhelmy, *Annalen der Physik*, 1863, **195**, 177-217.
93. J. Corporation, *Serial Line Communication Protocol Version 2.0 for JASCO V-5OO Series UVvis/NIR Spectrophotometer*, 1995.
94. J. Zabalza, J. C. Ren, Z. Wang, H. M. Zhao, J. Wang and S. Marshall, *Ieee Journal of Selected Topics in Applied Earth Observations and Remote Sensing*, 2015, **8**, 2845-2853.
95. F. Herrmann-Westendorf, T. Sachse, M. Schulz, M. Kaufmann, V. Sivakov, R. Beckert, T. J. Martinez, B. Dietzek and M. Presselt, *J Phys Chem A*, 2018.
96. A. M. Brouwer, *Pure Appl. Chem.*, 2011, **83**.
97. S. Fery-Forgues and D. Lavabre, *Journal of Chemical Education*, 1999, **76**, 1260.
98. R. Berera, R. van Grondelle and J. T. M. Kennis, *Photosynthesis Research*, 2009, **101**, 105-118.
99. D. W. Gehrig, I. A. Howard and F. Laquai, *Journal of Physical Chemistry C*, 2015, **119**, 13509-13515.
100. S. Singh and Z. V. Vardeny, *Materials*, 2013, **6**, 897-910.
101. J. Wiberg, T. Marinado, D. P. Hagberg, L. Sun, A. Hagfeldt and B. Albinsson, *Journal of Physical Chemistry B*, 2010, **114**, 14358-14363.
102. P. J. M. Johnson, V. I. Prokhorenko and R. J. D. Miller, *Optics Express*, 2009, **17**, 21488-21496.
103. B. Dietzek, T. Pascher, V. Sundström and A. Yartsev, *Laser Physics Letters*, 2007, **4**, 38-43.
104. H. Satzger and W. Zinth, *Chemical Physics*, 2003, **295**, 287-295.
105. E. L. Kovrigin, *bioRxiv*, 2017.
106. B. J. Berne and R. Pecora, *Dynamic Light Scattering: With Applications to Chemistry, Biology, and Physics*, Dover Publications2000.
107. J. W. Goodman, *J. Opt. Soc. Am.*, 1976, **66**, 1145-1150.
108. W. I. Goldburg, *American Journal of Physics*, 1999, **67**, 1152-1160.
109. D. Necas and P. Klapetek, *Cent Eur J Phys*, 2012, **10**, 181-188.
110. A. Leray, D. Rouede, C. Odin, Y. Le Grand, O. Mongin and M. Blanchard-Desce, *Optics Communications*, 2005, **247**, 213-223.
111. M. Gratzel, *Journal of Photochemistry and Photobiology C-Photochemistry Reviews*, 2003, **4**, 145-153.
112. M. Gratzel, *Inorganic Chemistry*, 2005, **44**, 6841-6851.
113. L. He, C. Jiang, Rusli, D. Lai and H. Wang, *Applied Physics Letters*, 2011, **99**, 021104.
114. M. Wright and A. Uddin, *Solar Energy Materials and Solar Cells*, 2012, **107**, 87-111.
115. S. K. Das, F. H. Schacher, U. Ritter, J. Plentz, G. Andrä, B. Dietzek and M. Presselt, *to be determined*, 2017.
116. S. Fischer, J. Vestfrid, A. Mahammed, F. Herrmann-Westendorf, M. Schulz, J. Müller, O. Kiesewetter, B. Dietzek, Z. Gross and M. Presselt, *ChemPlusChem*, 2016, **81**, 594-603.
117. M. C. Petty, *Biosensors & Bioelectronics*, 1995, **10**, 129-134.
118. J. Frischeisen, D. Yokoyama, C. Adachi and W. Brütting, *Appl. Phys. Lett.*, 2010, **96**, 073302.
119. C. Mayr, T. D. Schmidt and W. Brütting, *Applied Physics Letters*, 2014, **105**, 183304-183301 - 183304.
120. Y. X. Gao, J. Qi, J. Zhang, S. S. Kang, W. Q. Qiao, M. Li, H. Z. Sun, J. P. Zhang and K. Ariga, *Chemical Communications*, 2014, **50**, 10448-10451.
121. S. S. Babu and D. Bonifazi, *ChemPlusChem*, 2014, **79**, 895-906.
122. S. Das, F. Herrmann-Westendorf, F. H. Schacher, E. Tauscher, U. Ritter, B. Dietzek and M. Presselt, *ACS Applied Materials & Interfaces*, 2016, **8**, 21512-21521.
123. S. H. Habenicht, S. Schramm, S. Fischer, T. Sachse, F. Herrmann-Westendorf, A. Bellmann, B. Dietzek, M. Presselt, D. Weiß, R. Beckert and H. Görls, *Journal of Materials Chemistry C*, 2016, **4**, 958-971.
124. M. L. Hupfer, M. Kaufmann, F. Herrmann-Westendorf, D. Weiß, R. Beckert, B. Dietzek and M. Presselt, *to be submitted*, 2019.
125. T. Sachse, T. J. Martinez, B. Dietzek and M. Presselt, *J Comput Chem*, 2018.
126. H.-J. Son, C. H. Kim, D. W. Kim, N. C. Jeong, C. Prasittichai, L. Luo, J. Wu, O. K. Farha, M. R. Wasielewski and J. T. Hupp, *Acs Applied Materials & Interfaces*, 2015, **7**, 5150-5159.
127. S. Grimme, J. Antony, T. Schwabe and C. Muck-Lichtenfeld, *Organic & Biomolecular Chemistry*, 2007, **5**, 741-758.
128. D. M. Gampe, M. Kaufmann, D. Jakobi, T. Sachse, M. Presselt, R. Beckert and H. Gorls, *Chemistry*, 2015, **21**, 7571-7581.
129. F. Würthner, S. Yao, T. Debaerdemaeker and R. Wortmann, *Journal of the American Chemical Society*, 2002, **124**, 9431-9447.
130. F. Würthner, *Accounts of Chemical Research*, 2016, **49**, 868-876.
131. Z. Chen, A. Lohr, C. R. Saha-Moller and F. Wurthner, *Chem Soc Rev*, 2009, **38**, 564-584.
132. G. Li, K.-J. Jiang, Y.-F. Li, S.-L. Li and L.-M. Yang, *The Journal of Physical Chemistry C*, 2008, **112**, 11591-11599.
133. Y. Wu, M. Marszalek, S. M. Zakeeruddin, Q. Zhang, H. Tian, M. Grätzel and W. Zhu, *Energy & Environmental Science*, 2012, **5**, 8261.

134. C. Chen, X. Yang, M. Cheng, F. Zhang and L. Sun, *ChemSusChem*, 2013, **6**, 1270-1275.
135. W. J. D. Beenken and T. Pullerits, *Journal of Chemical Physics*, 2004, **120**, 2490-2495.
136. W. J. D. Beenken, F. Herrmann, M. Presselt, H. Hoppe, S. Shokhovets, G. Gobsch and E. Runge, *Physical Chemistry Chemical Physics*, 2013, **15**, 16494-16502.
137. J. Preiß, M. Jäger, S. Rau, B. Dietzek, J. Popp, T. Martínez and M. Presselt, *ChemPhysChem*, 2015, **16**, 1395-1404.
138. D. M. Gampe, M. Kaufmann, D. Jakobi, T. Sachse, M. Presselt, R. Beckert and H. Görls, *Chemistry – A European Journal*, 2015, **21**, 7571-7581.
139. F. Würthner and S. Yao, *Angew. Chem. Int. Ed.*, 2000, **39**, 1978-1981.
140. T. Kiyohiko and T. Osamu, *Bulletin of the Chemical Society of Japan*, 2015, **88**, 1466-1478.
141. S. J. GRABOWSKI, *Hydrogen Bonding-New Insights*, Springer2006.
142. S. S. Kuduva, D. Blaser, R. Boese and G. R. Desiraju, *Structural Chemistry*, 2001, **12**, 259-266.
143. E. E. Emelina, A. A. Petrov, A. O. Borissova, D. V. Filyukov and M. Y. Antipin, *Journal of Molecular Structure*, 2012, **1014**, 63-69.
144. L. D'Ascenzo and P. Auffinger, *Acta Crystallographica Section B*, 2015, **71**, 164-175.
145. J. Gershberg, F. Fennel, T. H. Rehm, S. Lochbrunner and F. Wurthner, *Chemical Science*, 2016, **7**, 1729-1737.
146. F. Wurthner, C. Thalacker, S. Diele and C. Tschierske, *Chemistry-a European Journal*, 2001, **7**, 2245-2253.
147. S. Lahiri, J. L. Thompson and J. S. Moore, *Journal of the American Chemical Society*, 2000, **122**, 11315-11319.
148. R. B. Martin, *Chemical Reviews*, 1996, **96**, 3043-3064.
149. T. Sachse, B. Dietzek, T. Martínez and M. Presselt, *Journal of Computational Chemistry*, 2017.
150. A. Klamt and G. Schüürmann, *Journal of the Chemical Society-Perkin Transactions 2*, 1993, 799-805.
151. R. F. Pasternack, C. Fleming, S. Herring, P. J. Collings, J. dePaula, G. DeCastro and E. J. Gibbs, *Biophysical Journal*, 2000, **79**, 550-560.
152. D. A. Voznyak and A. K. Chibisov, *Nanotechnologies in Russia*, 2008, **3**, 543.
153. F. Leyvraz, in *On Growth and Form: Fractal and Non-Fractal Patterns in Physics*, eds. H. E. Stanley and N. Ostrowsky, Springer Netherlands, Dordrecht1986, pp. 136-144.
154. Y. Sakuragi, X. F. Wang, H. Miura, M. Matsui and T. Yoshida, *Journal of Photochemistry and Photobiology a-Chemistry*, 2010, **216**, 1-7.
155. J.-M. Y. Carrillo, R. Kumar, M. Goswami, B. G. Sumpter and W. M. Brown, *Physical Chemistry Chemical Physics*, 2013, **15**, 17873-17882.
156. W. Chen, M. P. Nikiforov and S. B. Darling, *Energy & Environmental Science*, 2012, **5**, 8045-8074.
157. S. K. Das, J. Plentz, U. Brückner, M. von der Lühe, O. Eckhard, F. H. Schacher, E. Täuscher, U. Ritter, G. Andrä, B. Dietzek and M. Presselt, *Advanced Energy Materials*, 2018, **submitted**.
158. N. Zhou, H. Lin, S. J. Lou, X. Yu, P. Guo, E. F. Manley, S. Loser, P. Hartnett, H. Huang, M. R. Wasielewski, L. X. Chen, R. P. H. Chang, A. Facchetti and T. J. Marks, *Advanced Energy Materials*, 2014, **4**.
159. R. F. Khairutdinov and N. Serpone, *The Journal of Physical Chemistry B*, 1997, **101**, 2602-2610.
160. P. A. Antunes, C. J. L. Constantino, R. F. Aroca and J. Duff, *Langmuir*, 2001, **17**, 2958-2964.
161. J. Israelachvili and R. Pashley, *Nature*, 1982, **300**, 341.
162. Y. Diao, L. Shaw, Z. Bao and S. C. B. Mannsfeld, *Energy & Environmental Science*, 2014, **7**, 2145-2159.
163. H. Hoppe and N. S. Sariciftci, *Polymer Solar Cells*, Springer, Heidelberg, Berlin, 2008.
164. D. Bauman, R. Hertmanowski, K. Stefańska and R. Stolarski, *Dyes Pigm.*, 2011, **91**, 474-480.
165. A. Lodi, F. Momicchioli, M. Caselli, G. Giancane and G. Ponterini, *RSC Adv.*, 2013, **3**, 1468-1475.
166. S. H. Habenicht, S. Schramm, S. Fischer, T. Sachse, F. Herrmann-Westendorf, A. Bellmann, B. Dietzek, M. Presselt, Wei, R. Beckert and H. Görls, *Journal of Materials Chemistry C*, 2016, **4**, 958-971.
167. T. Martyński, R. Hertmanowski, R. Stolarski and D. Bauman, *Thin Solid Films*, 2008, **516**, 8834-8838.
168. E. E. Jelley, *Nature*, 1936, **138**, 1009.
169. F. Würthner, T. E. Kaiser and C. R. Saha-Möller, *Angewandte Chemie*, 2011, **123**, 3436-3473.
170. H. Hoppe, M. Niggemann, C. Winder, J. Kraut, R. Hiesgen, A. Hinsch, D. Meissner and N. S. Sariciftci, *Advanced Functional Materials*, 2004, **14**, 1005-1011.
171. K. C. Deing, U. Mayerhoffer, F. Wurthner and K. Meerholz, *Physical Chemistry Chemical Physics*, 2012, **14**, 8328-8334.
172. F. Laquai, D. Andrienko, R. Mauer and P. W. M. Blom, *Macromolecular Rapid Communications*, 2015, **36**, 1001-1025.
173. J. Hou and X. Guo, in *Organic Solar Cells*, ed. W. C. H. Choy, Springer, London2013, ch. 2, pp. 17-42.
174. A. Yamaguchi, N. Kometani and Y. Yonezawa, *Journal of Physical Chemistry B*, 2005, **109**, 1408-1414.
175. P. Wang and S. Y. Feng, *Journal of Photochemistry and Photobiology a-Chemistry*, 2010, **214**, 241-247.
176. J. A. Mondal, H. N. Ghosh, T. Mukherjee and D. K. Palit, *J Phys Chem A*, 2005, **109**, 6836-6846.
177. P. Verma and H. Pal, *Journal of Physical Chemistry A*, 2014, **118**, 6950-6964.
178. T. Kirchartz, B. E. Pieters, J. Kirkpatrick, U. Rau and J. Nelson, *Physical Review B*, 2011, **83**, 115209.
179. M. Presselt, F. Herrmann, S. Shokhovets, H. Hoppe, E. Runge and G. Gobsch, *Chemical Physics Letters*, 2012, **542**, 70-73.
180. M. Presselt, F. Herrmann, H. Hoppe, S. Shokhovets, E. Runge and G. Gobsch, *Advanced Energy Materials*, 2012, **2**, 999-1003.

181. H. Ellis, I. Schmidt, A. Hagfeldt, G. Wittstock and G. Boschloo, *Journal of Physical Chemistry C*, 2015, **119**, 21775-21783.
182. I. A. Howard, M. Meister, B. Baumeier, H. Wonneberger, N. Pschirer, R. Sens, I. Bruder, C. Li, K. Muellen, D. Andrienko and F. Laquai, *Advanced Energy Materials*, 2014, **4**.
183. M. Fakis, P. Hrobarik, O. Yushchenko, I. Sigmundova, M. Koch, A. Rosspeintner, E. Stathatos and E. Vauthey, *Journal of Physical Chemistry C*, 2014, **118**, 28509-28519.
184. C. Ruckebusch, M. Sliwa, P. Pernot, A. de Juan and R. Tauler, *Journal of Photochemistry and Photobiology C-Photochemistry Reviews*, 2012, **13**, 1-27.
185. X. Tan, T. L. Gustafson, C. Lefumeux, G. Burdzinski, G. Buntinx and O. Poizat, *The Journal of Physical Chemistry A*, 2002, **106**, 3593-3598.
186. G. Lanzani, G. Cerullo, S. Stagira and S. De Silvestri, *Journal of Photochemistry and Photobiology A: Chemistry*, 2001, **144**, 13-19.
187. M. L. Horng, J. A. Gardecki, A. Papazyan and M. Maroncelli, *The Journal of Physical Chemistry*, 1995, **99**, 17311-17337.
188. E. Ishow, G. Clavier, F. Miomandre, M. Rebarz, G. Buntinx and O. Poizat, *Physical Chemistry Chemical Physics*, 2013, **15**, 13922-13939.
189. W. Akemann, D. Laage, P. Plaza, M. M. Martin and M. Blanchard-Desce, *The Journal of Physical Chemistry B*, 2008, **112**, 358-368.
190. M. O. Lenz and J. Wachtveitl, *The Journal of Physical Chemistry C*, 2008, **112**, 11973-11977.
191. A. C. Benniston, K. S. Gulliya and A. Harriman, *J. Chem. Soc., Faraday Trans.*, 1997, **93**, 2491-2501.
192. G. Klein, *Chemical Physics Letters*, 2000, **320**, 65-69.
193. D. Minh Trung, L. Hirsch, G. Wantz and J. D. Wuest, *Chemical Reviews*, 2013, **113**, 3734-3765.
194. M. A. El-Sayed and T. Pavlopoulos, *The Journal of Chemical Physics*, 1963, **39**, 1899-1900.
195. T. Roland, E. Heyer, L. Liu, A. Ruff, S. Ludwigs, R. Ziessel and S. Haacke, *Journal of Physical Chemistry C*, 2014, **118**, 24290-24301.
196. J. Moreno, A. L. Dobryakov, I. N. Ioffe, A. A. Granovsky, S. Hecht and S. A. Kovalenko, *Journal of Chemical Physics*, 2015, **143**.
197. V. Dyakonov, *Applied Physics A-Materials Science & Processing*, 2004, **79**, 21-25.
198. D. Chirvase, J. Parisi, J. C. Hummelen and V. Dyakonov, *Nanotechnology*, 2004, **15**, 1317-1323.
199. H. Hoppe and N. S. Sariciftci, *Journal of Materials Chemistry*, 2006, **16**, 45-61.
200. R. M. Beal, A. Stavrinadis, J. H. Warner, J. M. Smith, H. E. Assender and A. A. R. Watt, *Macromolecules*, 2010, **43**, 2343-2348.
201. C. R. Singh, M. Sommer, M. Himmerlich, A. Wicklein, S. Krischok, M. Thelakkat and H. Hoppe, *Physica Status Solidi-Rapid Research Letters*, 2011, **5**, 247-249.
202. C. L. Zhan and J. N. Yao, *Chemistry of Materials*, 2016, **28**, 1948-1964.
203. T. Heumueller, W. R. Mateker, A. Distler, U. F. Fritze, R. Cheacharoen, W. H. Nguyen, M. Biele, M. Salvador, M. von Delius, H.-J. Egelhaaf, M. D. McGehee and C. J. Brabec, *Energy & Environmental Science*, 2016, **9**, 247-256.
204. J. Rehman, H. Y. Araghi, A. Q. He and M. F. Paige, *Langmuir*, 2016, **32**, 5341-5349.
205. M.-J. Sun, X. Zhang, Y.-W. Zhong, C. Zhan and J. Yao, *Inorganic Chemistry*, 2016, **55**, 13007-13013.
206. S. Shalini, R. Balasundaraprabhu, T. S. Kumar, N. Prabavathy, S. Senthilarasu and S. Prasanna, *International Journal of Energy Research*, 2016, **40**, 1303-1320.
207. S. Feng, Q. S. Li, P. P. Sun, T. A. Niehaus and Z. S. Li, *Acs Applied Materials & Interfaces*, 2015, **7**, 22504-22514.
208. A. G. Gagorik, J. W. Mohin, T. Kowalewski and G. R. Hutchison, *Advanced Functional Materials*, 2015, **25**, 1996-2003.
209. A. C. Khazraji, S. Hotchandani, S. Das and P. V. Kamat, *The Journal of Physical Chemistry B*, 1999, **103**, 4693-4700.
210. F. C. Spano and C. Silva, *Annual Review of Physical Chemistry*, 2014, **65**, 477-500.
211. A. K. Chibisov, T. D. Slavnova and H. Gorner, *Chemical Physics Letters*, 2004, **386**, 301-306.
212. S. J. Yang, H. Tian, H. M. Xiao, X. H. Shang, X. D. Gong, S. D. Yao and K. C. Chen, *Dyes and Pigments*, 2001, **49**, 93-101.
213. N. K. Nath, K. Manoj, A. S. Gaz and P. Naumov, *Chemistry-a European Journal*, 2013, **19**, 8094-8099.
214. T. Sachse, T. J. Martinez, B. Dietzek and M. Presselt, *Journal of Computational Chemistry*, 2018, **39**, 763-772.
215. M. L. Hupfer, M. Kaufmann, F. Herrmann-Westendorf, T. Sachse, L. Roussille, K. H. Feller, D. Weiss, V. Deckert, R. Beckert, B. Dietzek and M. Presselt, *ACS Appl Mater Interfaces*, 2017, **9**, 44181-44191.
216. M. Schulz, F. Dröge, F. Herrmann, J. Schindler, H. Görls and M. Presselt, *Dalton Transactions*, 2016, **45**, 4835-4842.
217. A. De la Cadena, T. Pascher, D. y. Davydova, D. Akimov, F. Herrmann, M. Presselt, M. Wächtler and B. Dietzek, *Chemical Physics Letters*, 2016, **644**, 56-61.
218. F. Würthner, *Nature Chemistry*, 2014, **6**, 171-173.
219. M. Kaufmann, M. L. Hupfer, T. Sachse, F. Herrmann-Westendorf, D. Weiß, B. Dietzek, R. Beckert and M. Presselt, *Journal of Colloid and Interface Science*, 2018, **526**, 410-418.

220. O. V. Kozlov, X. Liu, Y. N. Luponosov, A. N. Solodukhin, V. Y. Toropynina, J. Min, M. I. Buzin, S. M. Peregudova, C. J. Brabec, S. A. Ponomarenko and M. S. Pshenichnikov, *The Journal of Physical Chemistry C*, 2017, **121**, 6424-6435.
221. F. Würthner, S. Yao and U. Beginn, *Angewandte Chemie International Edition*, 2003, **42**, 3247-3250.
222. R. Eisenschitz and F. London, *Zeitschrift für Physik*, 1930, **60**, 491-527.
223. C. A. Hunter and J. K. M. Sanders, *Journal of the American Chemical Society*, 1990, **112**, 5525-5534.
224. F. Padinger, R. S. Rittberger and N. S. Sariciftci, *Advanced Functional Materials*, 2003, **13**, 85-88.
225. P. J. Brown, D. S. Thomas, A. Kohler, J. S. Wilson, J. S. Kim, C. M. Ramsdale, H. Sirringhaus and R. H. Friend, *Physical Review B*, 2003, **67**.
226. T. Erb, U. Zhokhavets, G. Gobsch, S. Raleva, B. Stuhn, P. Schilinsky, C. Waldauf and C. J. Brabec, *Advanced Functional Materials*, 2005, **15**, 1193-1196.
227. F. Würthner, C. Thalacker and A. Sautter, *Advanced Materials*, 1999, **11**, 754-758.
228. A. Moliton, *Optoelectronics of Molecules and Polymers*, Springer, Berlin, 2006.
229. D. Wei, *International Journal of Molecular Sciences*, 2010, **11**, 1103-1113.
230. L. Giribabu, R. K. Kanaparthi and V. Velkannan, *Chemical Record*, 2012, **12**, 306-328.
231. J. A. Gutierrez, R. D. Falcone, J. J. Silber and N. M. Correa, *Journal of Physical Chemistry A*, 2010, **114**, 7326-7330.
232. P. L. Wash, E. Maverick, J. Chiefari and D. A. Lightner, *Journal of the American Chemical Society*, 1997, **119**, 3802-3806.
233. K. Ikegami, *Curr. Appl Phys.*, 2006, **6**, 813-819.
234. C. Ruckebusch, M. Sliwa, P. Pernot, A. de Juan and R. Tauler, *Journal of Photochemistry and Photobiology C: Photochemistry Reviews*, 2012, **13**, 1-27.
235. S. Ogi, V. Stepanenko, J. Theirs and F. Wurthner, *Journal of the American Chemical Society*, 2016, **138**, 670-678.

Appendix

Driving forces of aggregate formation

The origin of the formation of different supramolecular-structures is a superposition of the forces between the single molecules and the paramters and kinetics at the aggregate formation process.

The dipole-dipole interaction has usually significant impact for very polar molecules[51]. The binding energy is typically in the range of kT (25 meV) and only emerges above that for very polar molecules[51]. The dipole-dipole intermolecular force depends strongly on the alignment of the molecules dipoles. The dipole-dipole force reaches its maximum for parallel aligned molecules and is reduced by a factor of two for an in-line allignement[51]. Hence the dimer formation of ordered linear structures is facilitated, while the growth in the second dimension is less pronounced.

As stated by a review from Frank Würthner[130] the dipole-dipole interaction can be used to produce much defined supramolecular structures especially with the molecule class of merocyanines[129-131]. The use of merocyanines is very beneficial since they usually have a very high ground state dipole moment, which exceed 10 Debye. Even values close to 20 Debye are reported[130, 131]. Also most of the organic push-pull or donor-(π)-acceptor dyes used in modern organic photovoltaic devices[74, 220] have a strong dipolar character. This is caused by the need of a strong charge transfer character of the first excitation to move the first absorption peak as far as possible to the red or NIR spectral region[15].

With this dipole-dipole assembled molecules big linear structures could be assembled via a supramolecular polymerization leading to highly bound aggregates. These could be transferred to the solid state by a simple spin coating process[221]. The production of these long tubular structures can afterwards also lead to a surprising gelation, which is usually found for polymeric materials rather than small dye molecules.

The dipole-moment of push-pull dyes can typically be further enhanced upon charge transfer (CT) excitations[19, 43, 132, 133], thus possibly causing the formation of different supramolecular structures as compared to the dark. Consequently, it appears to be essential to determine the influence of light on supramolecular structure formation, which was recently reported for cyanine dyes[58].

Most organic dyes which absorb in the Vis to NIR region usually have an extended aromatic chromophore, which is in most cases relatively flat. Hence the formation of aggregates due to the London dispersion interaction is very likely. The London dispersion force is, in most cases, the main distribution to the overall van der Waals forces.[52] The origin of the dispersion force is the spontaneous polarization due to quantum mechanically fluctuations of the dipole moments of neutral molecules.[222] The dispersion force can be repulsive or attractive and are non-additive. For small round particles the force is proportional to r^{-6}, but for all larger molecules or particles the behavior will be very much different.[52] The dispersion force is also able to align

molecules in a defined way, but the alignment will not be as efficient as for *e.g.* dipole-dipole interactions.

The molecular interactions between many dyes with extended π-systems are governed by dispersion interactions.[127, 128] A special case for the aggregation by London dispersion is the π- π-stacking, which is very prominent in the aggregation of flat dye molecules with an extended π-systems.[223] Many classes of molecules used in organic optoelectronic devices show this π- π-stacking. One example is the partially crystallization of polymers used in organic bulk-heterojunction solar cells, which is known to enhance the device efficiency drastically for *e.g.* P3HT[197, 224-226]. π-π-stacking in small molecules is in depth researched for different perylene derivatives[167, 227] and several other classes of molecules. [147] The π- π-stacking of the molecules is usually leading to an enhanced electronic coupling between the adjacent molecules. This is very favorable due to the close distance in a π- π-stack leading to a significant improved hopping probability of electrons from one molecule to the adjacent one.[228]

Hydrogen bonds

As many of the dyes used in *e.g.* DSSC devices have different acid groups[26, 229, 230] to be bound to the electron accepting semiconductor, hydrogen bonds have to be taken into account. Hydrogen bonds are usually created between a electronegative atom like *e.g.* oxygen and a hydrogen covalently bound to another strong electronegative atom.[53] Those bonds are fairly directional and show a relatively high binding energy, which can reach values of 5-10 kT(125-250meV). These kind of bonds can exist either intermolecular[145] or intramolecular[231] and will usually exist in a non-polar environment.[52] Beneath the acid groups also cyano[143] or amid[232] moieties can be part of a hydrogen bond. Due to their high binding energy and high degree of directionality hydrogen bonds are often seen in crystal structures of different dyes like *e.g.* merocyanines.[71]

Amphiphilisity

Water always likes to be stabilized by its inherent hydrogen bonds. The introduction of molecules, which do not have the possibility of forming hydrogen bonds will always force the surrounding water molecules into non optimal arrangements, which in principle will cost energy.[53] These kind of molecule or even moieties of molecules are denoted as hydrophobic molecules. Examples of hydrophobic molecules are hydrocarbons. The hydrophobic effect itself describes that the two hydrophobic molecules in a water environment will have a strong driving force to form aggregates or to assemble at the water air surface. The energetically gain from the hydrophobic effect is a mainly entropic effect, which arises due to the need for rearrangement of the hydrogen bonds of the water molecules that surround the hydrophobic molecules. This means that the hydrophobic molecules will always try to minimize the contact area with water or other hydrogen bonding solvent molecules.

Despite this hydrophobic effect also a hydrophilic interactions exists. This is usually present for molecular moieties, which tend to form hydrogen bonds with the surrounding solvent rather than interacting with each other. Hydrophilic groups are for example carboxylate, sulfonate, polyethylene oxide, amine or alcohol groups.

By assembling molecules with hydrophilic and hydrophobic groups we gain amphiphilic molecules like soaps, detergents or lipoproteins. These special types of molecules tend to organize at the interface of water or other polar media and non-polar media. The non-polar

media in this case can be *e.g.* air, a non-polar solvent like hexane or a hydrophobic solid state surface. With the approach of using amphiphilic molecules very different aggregates could be created using for example porphyrinoids[121] or merocyanines[233].

Steric hindrance

As aggregation is not always favorable like in *e.g.* most of the DSSC devices[19, 31, 35, 39], the implementation of stearic hindrances is possible to prevent aggregation. As steric hindering groups *e.g.* linear and branched alkyl groups are often used.[19] Despite the chemical binding of sterically demanding groups also sterically demanding molecules can be used. These classes of molecules are known as aggregation preventing agents. Derivatives of the cholic acid[35, 71] are often used as such aggregation prevention agent.

Quantum chemically derived properties of dimers

In the following, van der Waals surfaces with electrostatic potentials are shown for various dimers in Figure A 1 and characteristic geometric properties are listed in Table 5. Also the structure of one oligomer is shown to visualize the possibility of polymerization as discussed in the main text. The absorption spectra of the dimers and the oligomer are compared in Figure A 3.

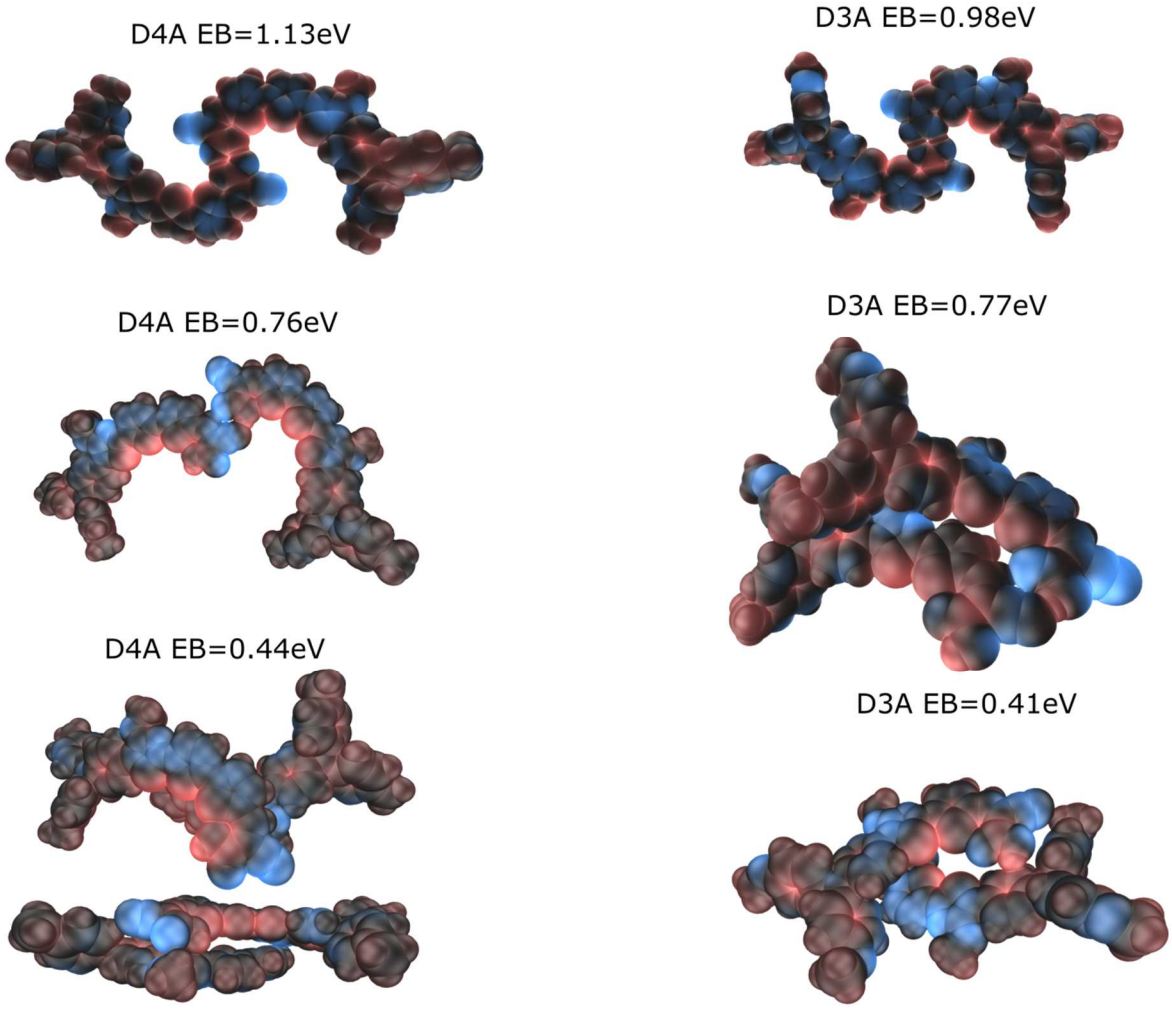

Figure A 1 Electrostatic potential at the van der Waals surfaces and binding energies for the different dimes.

Table 5 Binding energies and geometric parametersof selected dimers

	E_{bin} [eV]	|r|(C=O--H) [Å]	|r|(O-H--O) [Å]	|r|(C≡N--H) [Å]	|r|(N--H-O) [Å]
D3A , AA	0.98	1.589	2.598		
D3A , AN	0.77	2.308	3.376	1.738	2.726
D4A , AA	1.13	1.536	2.556		
D4A , AN	0.76	2.072	3.155	1.737	2.728

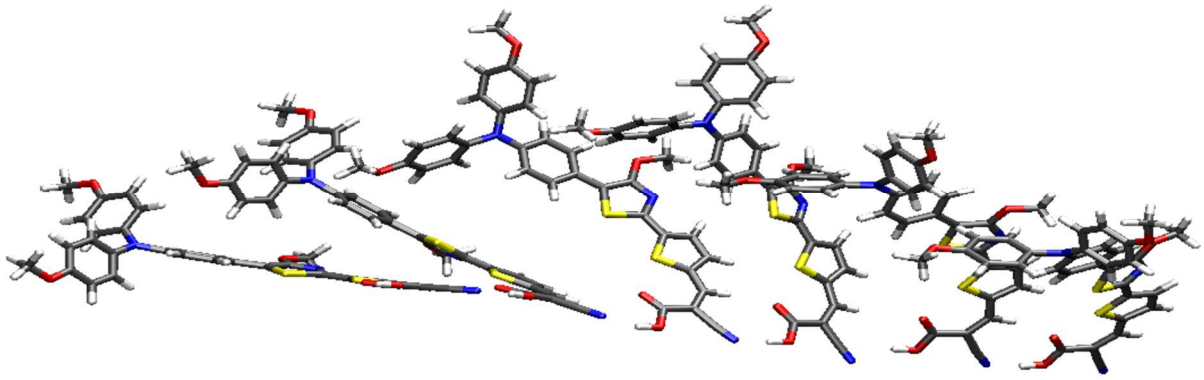

Figure A 2 **D3A** Oligo-aggregate constructed from the ANPi-dimer with 6 monomeric units.

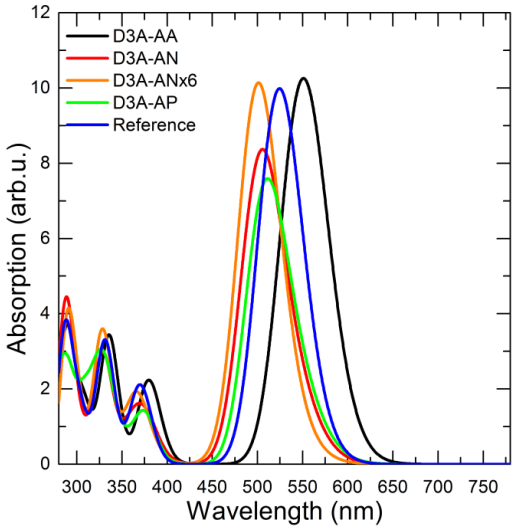

Figure A 3 Absorption spectra of dimers and one hexamer (orange line) of **D3A** calculated by TD-DFT. All spectra were calculated in vacuum and shifted by 400 meV to the red. The broadening of the peaks was set to 300 meV.

Dynamic light scattering (DLS) experiments

In the following, the reduction in particle size due to irradiation is shown in Figure A 4. This reduction is in line with the formation of small dimers with compensating dipole moments, here from larger aggregates, as discussed in the main text. Formation of dimers or small aggregates when decreasing the solvent polarity is shown by the DLS data shown in Figure A 5.

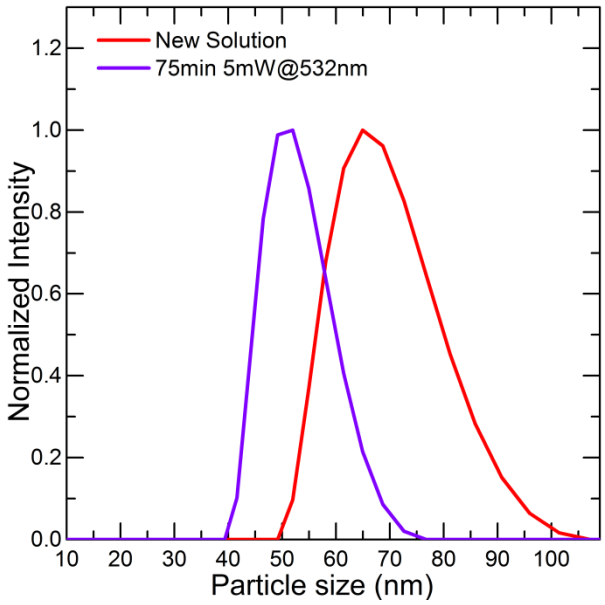

Figure A 4 Particle size distribution of **D4A** in chloroform with a concentration of 1 mg/ml before and after illumination with a 532 nm laser. After illuminating the solution the size distribution is getting narrower and shifts to smaller diameters. Furthermore, the mean scattering intensity increases by a factor of four. This indicates an increase in the number of particles in the solution.

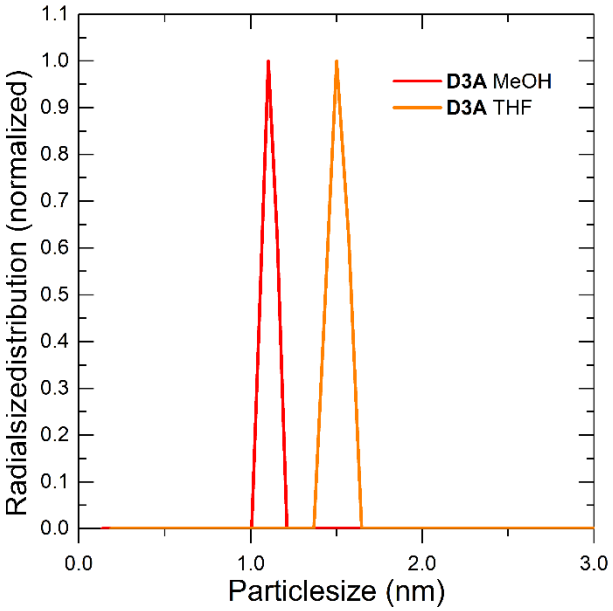

Figure A 5 Fits of the DLS data of **D3A** in methanol (c=0.4 mM) and THF (c=0.2 mM). The methanol-solution shows one peak centered at ~1 nm, what corresponds to the monomeric molecular size.

SVD analysis for photoaggregation data

A singular-value decomposition (SVD) analysis was performed, which is a common method for the data analysis of hyperspectral images.[94] This method splits the 2D matrix of absorbance values (A-matrix) into a spectral component (U-matrix) and a specific kinetic trace for every component (V-matrix). This is coupled by the diagonal S matrix, which gives a weighting of the single component. The diagonal values are usually merged into a vector S in descending order.

$$A = U \cdot S \cdot V^T \tag{2.2}$$

To determine the significant components only those components are chosen, which have a reasonable high value in the corresponding element of the S vector. The SVD analysis was performed using the respective tool in the Labview math package. With the SVD analysis we get a model-free set[234] of components and their respective kinetics. The kinetics can afterwards be analyzed using *e.g.* the model Pasternack *et al*.[151]

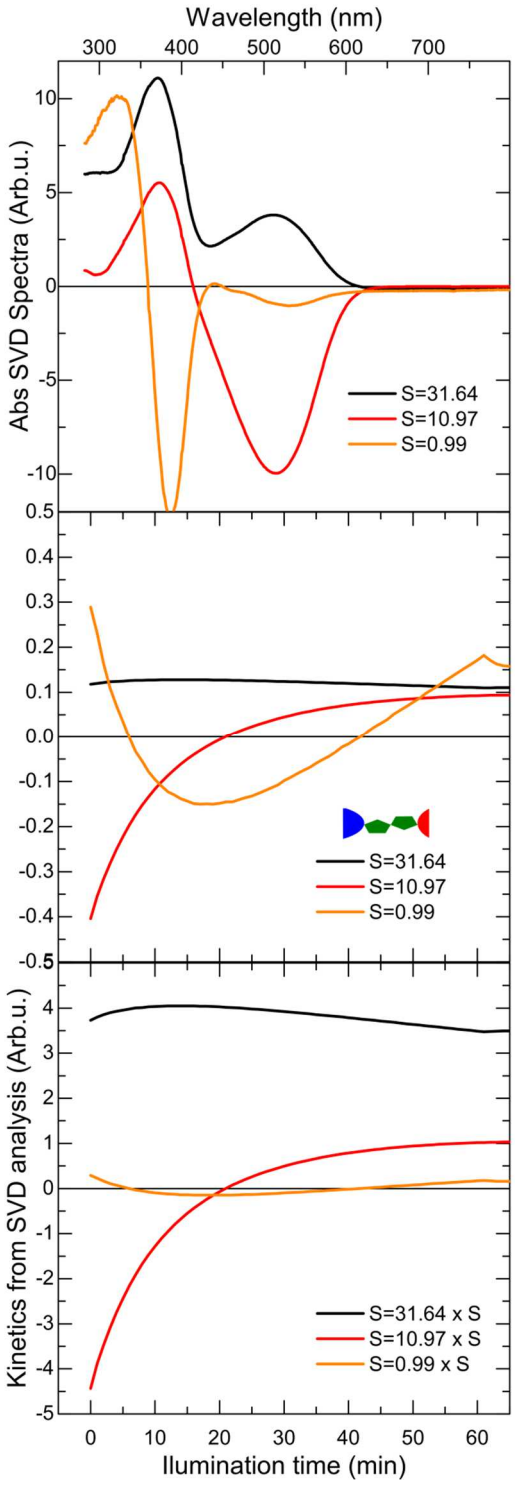

Figure A 6 Example of the SVD analysis of illumination dependent UV-vis spectra. Here the spectra measured with **D2A** in CF with a concentration of 23.4 mM are presented. The upper panel shows the spectral traces of the first three components. The middle panel shows the non-normalized kinetic traces, while the lower panel shows the kinetics multiplied by the respective value of the S vector.

For all datasets measured we get three significant components (C1, C2 and C3). Values in the S vector, resembling the significance of the respective component, are shown in the main text. In

the kinetics graph the curves are multiplied by the corresponding value of the S-vector. This is done to illustrate the weighting of the components right in the kinetics curve.

The first component C1 resembles the final spectra obtained after 60 min of illumination. Hence it turned out to have, by far, the highest significance value. The C2 component mainly describes the changes in the spectra upon illumination. Hence, we have chosen the kinetic of C2 for fitting with the stretched exponential model discussed in the main text. The third component C3 already has much smaller significance and represents slight shifts in the absorption bands of the monomer and dimer, which occur mainly in the first 30 min of illumination. C3 might be assigned to intermediate states or to reorganization of the dimers and accompanied spectral shifts, cf. TD-DFT-derived absorption spectra of the different dimers.

Kinetics

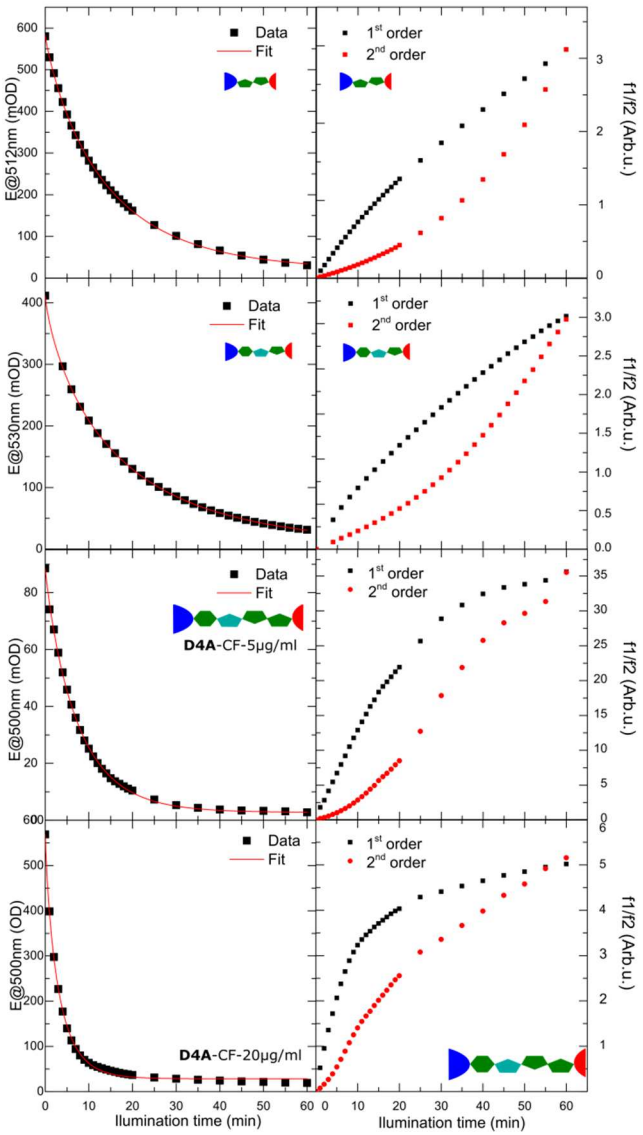

Figure A 7 Evolution of the extinction *E* of **D2A**, **D3A** and **D4A** with time and line fits according a stretched exponential model (left column) and order determination by checking for linearity of the functions f1, f2 for first, second order, respectively (right column).

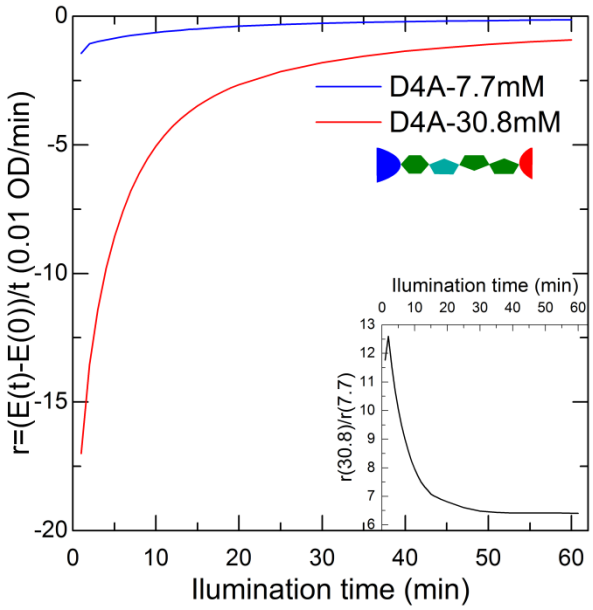

Figure A 8 Reaction rates *r* plotted over the illumination time of **D4A** in chloroform with different concentrations. The inset shows the *r*-ratio for the two different concentrations r(c=30.8 mM)/r(c=7.7 mM).

Analysis of the photo dimers

To gain better information about possible degradation, NMR measurements were performed with **D3A** in different solvents. The same experiments were not made with **D4A** and **D2A** since both materials were already empty at this point. **D3A** could be newly synthesized on a relatively short timescale. A new batch of **D4A** was not synthesized due to a highly toxic reaction step in the synthesis.[71] As solvents $DCCL_3$, THF-d_6 and DMSO-d_6 were chosen. In DMSO the spectra look like they should since it is a very good solvent for **D3A**, but the relevant hydrogen at the carboxylic acid group is not measurable in DMSO due to the fast hydrogene deuterium exchange with the solvent. The signals obtained in THF and $DCCl_3$ are shown in Figure A 9.

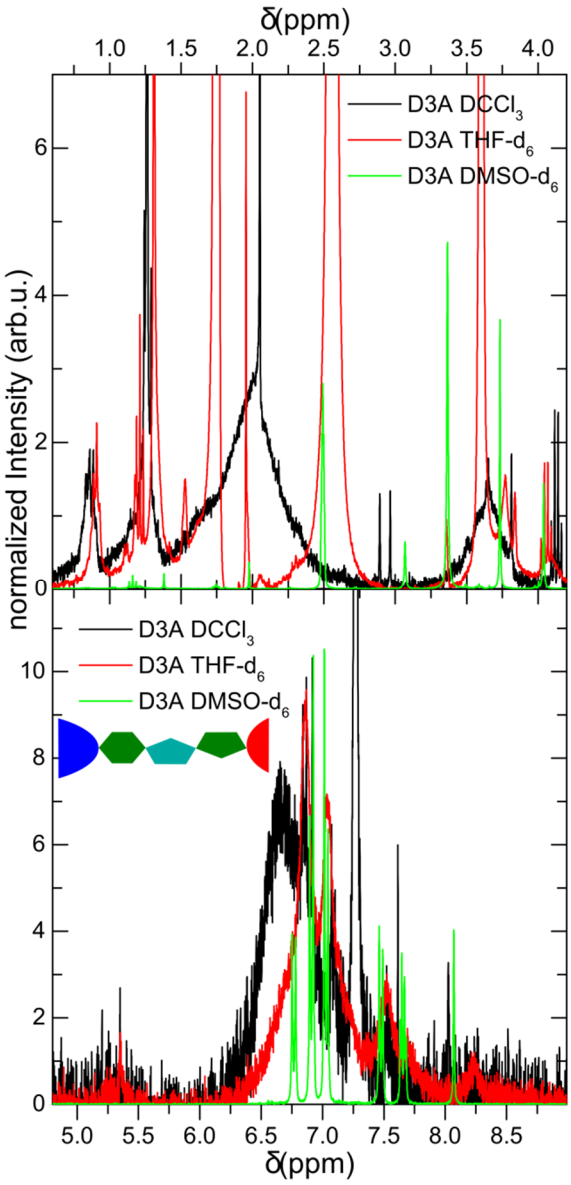

Figure A 9 1H-NMR spectra of **D3A** in different solvents. The upper panel resembles non-aromatic part, while the lower panel is showing the aromatic part of the molecule. While the spectra in DMSO-d_6 clearly show all expected features, the spectra in THF-d_6 and $DCCl_3$ show very broad and shifted peaks. Since the solubility in the later solvents is much lower than in DMSO, the spectra resemble somehow different aggregates rather than monomeric species.

The 1H-NMR spectra measured in DMSO show very narrow peaks and all expected signals could be found for the measured molecule. In $DCCl_3$ the signals are partly shifted in comparison to the DMSO-d_6 spectra. Furthermore, the aromatic and non-aromatic spectral range is overlaid by strong broad signals, which is common for aggregated molecules. In THF-d_6 the signals are also broad and shifted, but the broad background signals are slightly reduced in comparison to the $DCCl_3$ case. One point that has to be denoted in this manner is that we could grow a little **D3A**-THF-d_6 worm with a gelatinous consistency in the NMR tube. A picture of this worm can be found in Figure A 13. Furthermore, experiments using highly concentrated solutions of **D3A** in chlorobenzene created a red gel with the consistence of wobbly jelly, also shown in the appendix.

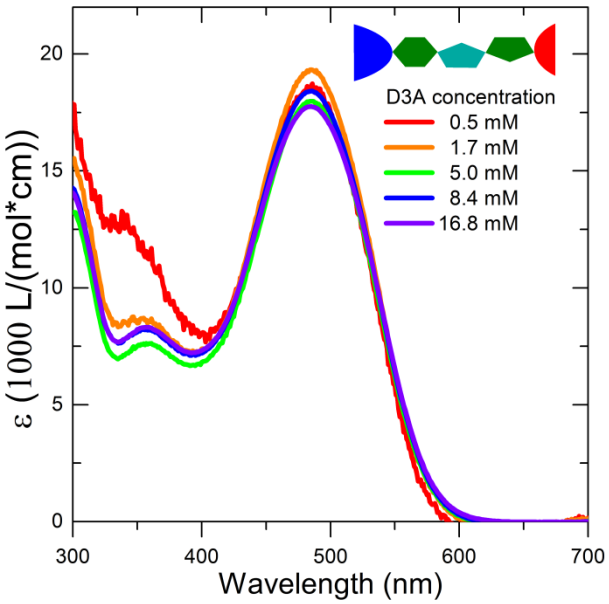

Figure A 10 Concentration dependent molar extinction coefficient of **D3A** in DMSO.

As writen in the main part of Chapter 3, the extinction coefficient of **D3A** does not depend on the concentration using the highly polar solvent DMSO.

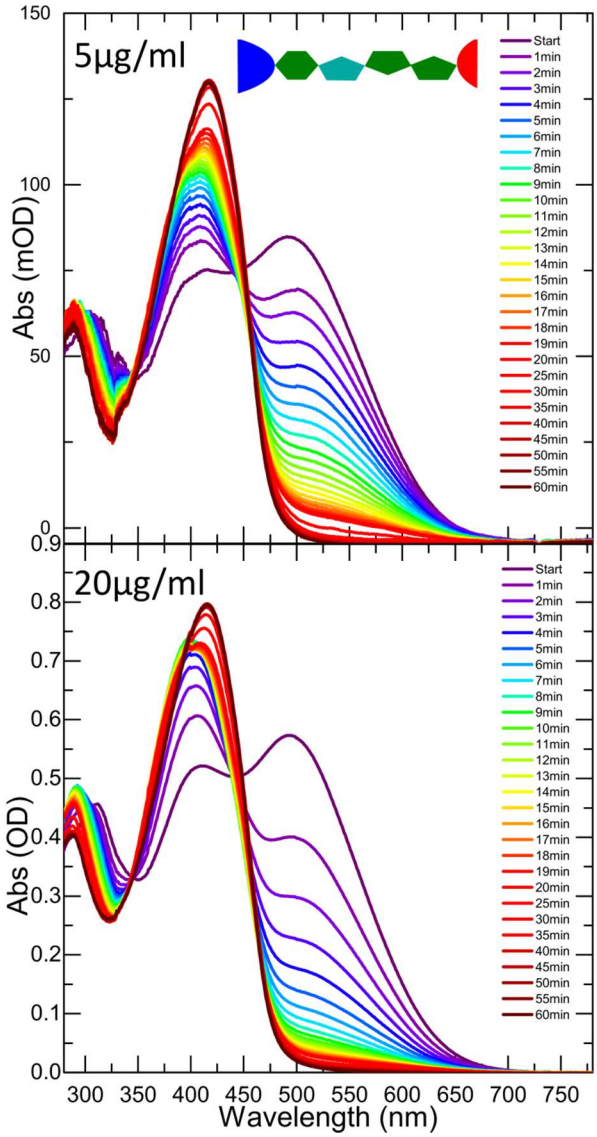

Figure A 11 Photoaggregation of **D4A** in CF with dye concentrations of 5 and 20µg/ml.

Gel formation in highly concentrated solutions

Surprisingly we also found that **D3A** forms gels in chlorobenzene and THF-d6. In chlorobenzene this behavior was reproduced several times with a concentration of approximately 10mg/ml (~17mM). Since this concentration basically is in the range of 1% by weight, the gel formation was not expected. Only for molecules with a very different non-covalent polymerization, *eg* amide-functionalized perylene bisimide, similar gels could be found for lower concentrations (1mM)[235]. The chlorobenzene wobbly jelly is shown in the upper panel of Figure A12. The microscopic structure is shown in the middle and lower panel of the same figure. The microscopic pictures were prepared by jamming a portion of the jelly in-between two microscopy slides and investigating this sample by a standard Zeiss microscope with a 20 fold magnification objective. As it can be seen in the microscope pictures the gel consists of fiber like structures.

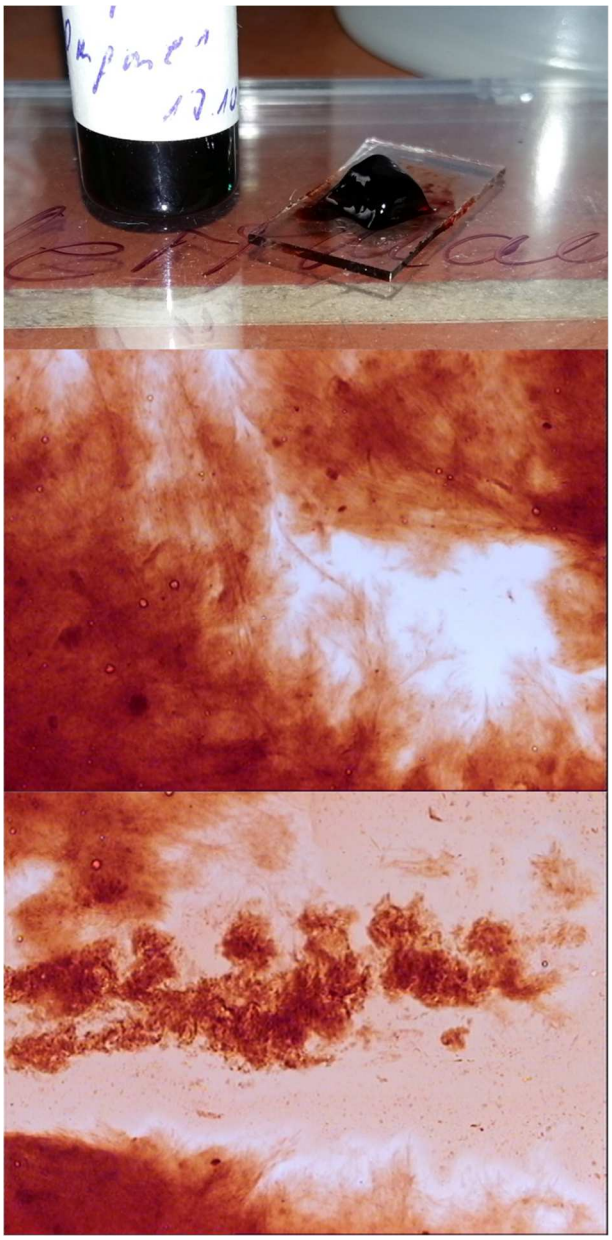

Figure A 12 Gel formed from a 10mg/ml solution of **D3A** in chlorobenzene. **D3A** tends to create red jelly like gel after being stored at elevated temperature of about 50°C. After being compressed between two microscopy slides we could observe the fiber like structure of the gel with an optical microscope from Zeiss with a 20 fold magnification shown in the lower panels.

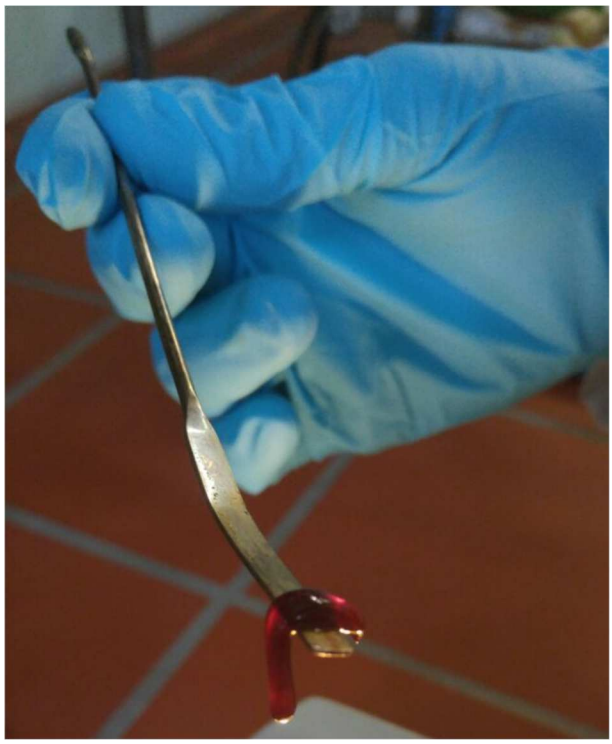

Figure A 13 Little gel worm grown in a NMR-tube with **D3A** in THF-d6.

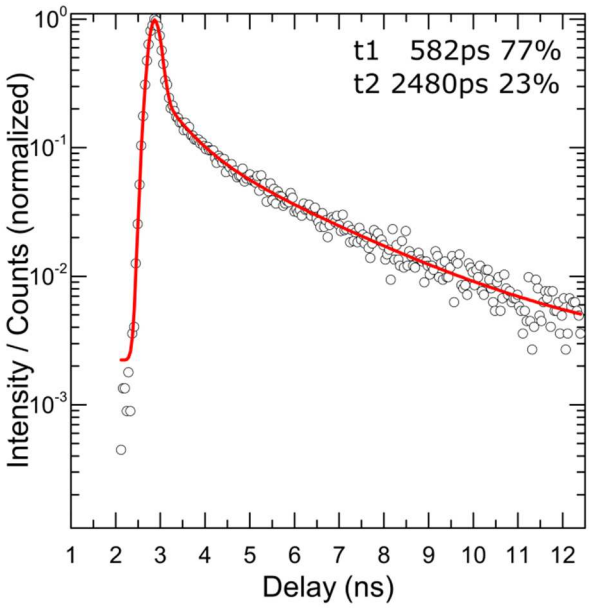

Figure A 14 Time correlated emission of **D4A** in CF.

Transient absorption of ***D2A***

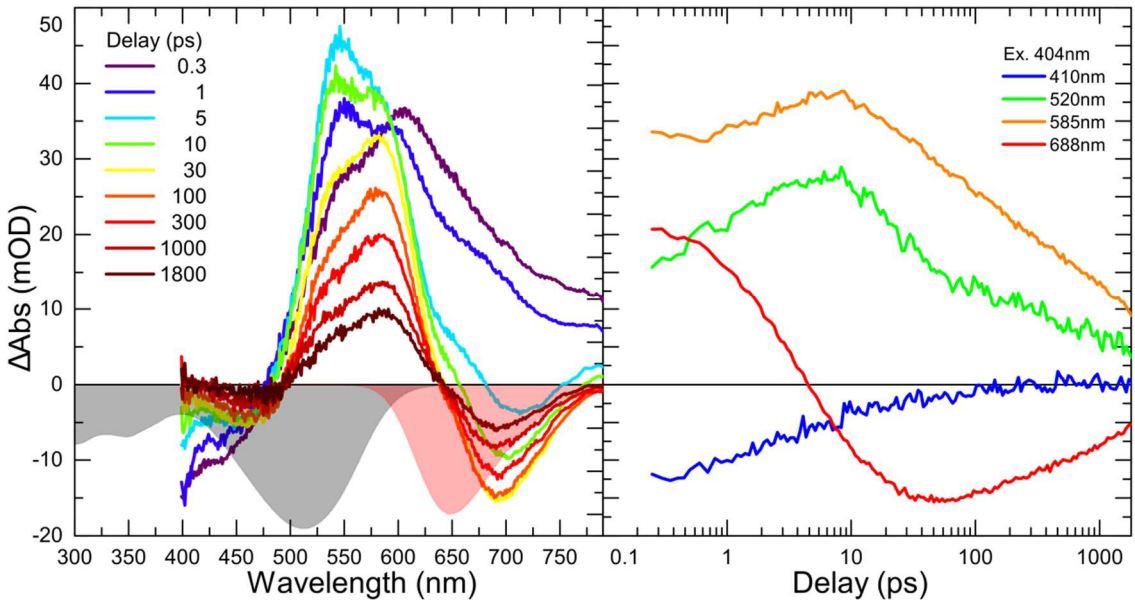

Figure A 15 Spectral traces(left)) at404nm pump and kinetic traces (right) of **D2A** in CF. The negative absorption and negative emission are shown as shaded areas in grey and red, respectively.

Upon excitation at 530 nm, **D2A** dissolved in CF shows a single exponetial decay with a timeconstant of 31 ps plus a long living infinity component. The DAS spectra of the TA spectra gained by pumping either at 404 and 520 nm are shown in Figure A 16. The infinity component consists of a peak at 580 nm (2.15 eV) and a stimulated emission (SE) centered at around 700 nm. This component is similar to a component with 390 ps decay time observed in the experiment with 404 nm excitation wavelength. The component with 31 ps resembles the build up and shift of the SE and the excited state absorption, respectivly. Upon excitation at 404 nm, *i.e.*, at an energy between those of the first and second lowest transitions, three distinct contributions to the DAS can be seen. The component observed in the 530 nm TA-spectrum is similar to the 17 ps and 390 ps decay components of the 404 nm TA-spectrum. Taking the S_0-to S_n energy values obtained from the absorption in the UV-region, we could assume to find excited state absorptions (ESA) at 550 nm (2.25 eV) and 660 nm (1.88 eV). These could be assigned to the $S_1 \rightarrow S_4$ and $S_1 \rightarrow S_3$ transitions, respectively. But only the band at 580 nm is clearly pronounced in the TA-spectra. Interestingly, no ground state bleach (GSB) could be observed for both excitation wavelengths. We furthermore could only find one negative part in the 390 ps and infinity component of the 404 nm excitation and in the infinity component of the 530 nm centered at around 700 nm. This can be attributed to a stimulated emission (SE) of the S_1 state, since it is located just slightly red shifted from the steady state fluorescence peaking at 650 nm and shown red shaded in. Using the spectral traces with the improved spectral range up to 780 nm we could clearly observe the temproral evolution of the GSB and the SE. The SE is visible after approx. 5 ps and than shifts slightly to the blue by increasing its amplitude up to 30 ps. This can be attributed to a somehow slow vibrational cooling. Which could be expected since we have excited into S_2 and a very hot S_1 state. The SE is somehow red shifted compared to the

steady state experiment, which is most probably due to the spectral overlap of the ESA centered at 600 nm, the soulder at 650nm, seen in the early delay times, and SE signal.

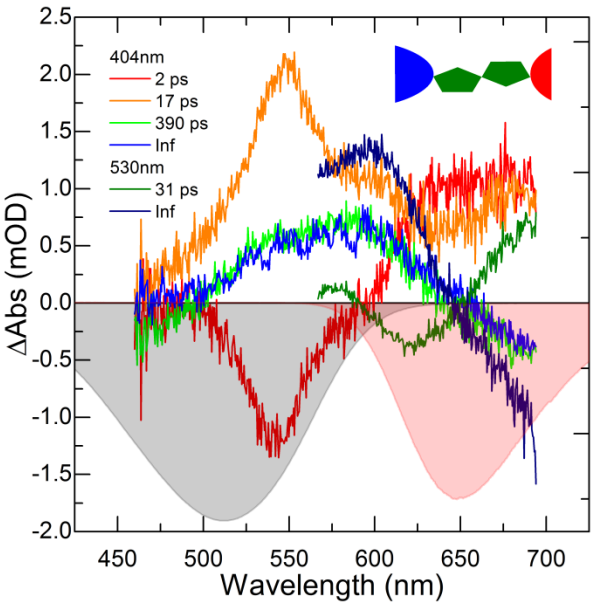

Figure A 16 DAS of **D2A** in CF for both excitation wavelengths (530 nm and 404 nm). The negative extinction coefficient is shaded in grey while the emission is shaded in light red.

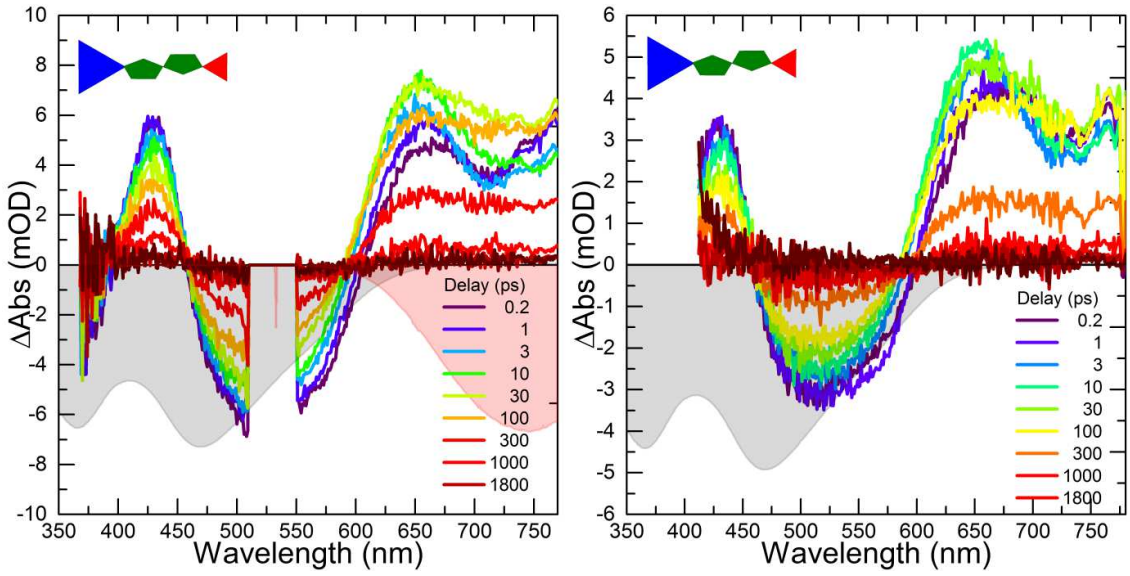

Figure A 17 Spectral traces of **D3A** new batch in CF at 530 nm excitation wavelength (left) and spectral traces at 390nm excitation wavelength (right). The negative molar extinction coefficient is plotted in grey and the fluorescence spectrum in red (new batch).

Danksagung

An erster Stelle möchte ich mich bei meinem Betreuer Dr. Martin Presselt für die gute Betreuung bedanken. Insbesondere für die stete Unterstützung in der langwierigen und anstrengenden Phase des Anträge, Anträge und noch mehr Anträge Schreibens, um die Finanzierung der Forschung zu meiner Dissertation zu gewährleisten. Vielen Dank für die Geduld, Hilfe und Motivation in Phasen, wo Photoreaktionen der Untersuchten Moleküle eine komplette Neubewertung der Daten und viele neue Experimente notwendig machten. Einen besonderen Dank auch für die Möglichkeit während der Promotion selbstständig sehr sensitive optische Messaufbauten realisieren zu können. Beim Arbeiten am PDS und Fluoreszenzaufbau habe ich sehr viel gelernt und es war unheimlich spannend die Messplätze von der Projektierung bis zum fein Tuning der Software und steten Erhöhung der Sensitivität immer weiter zu optimieren. Ich danke auch für die Geduld bei der Überarbeitung und Diskussion meiner verschiedenen Paper Manuskripte und der Dissertationsschrift, bei denen mal ein Fein-, aber öfters auch ein Grobschliff notwendig war.

Ich danke auch ganz besonders Prof. Benjamin Dietzek für die Betreuung meiner Arbeit und die vielen wertvollen Hinweise, Diskussionen und konstruktiven Kritiken ohne die diese Arbeit kaum möglich gewesen wäre.

Prof. Beckert und Prof. Würthner und deren Arbeitsgruppen danke ich für die Bereitstellung der hier untersuchten Farbstoffe.

Hier sei insbesondere Martin Kaufmann hervorgehoben, der mir stets alle Fragen eines Physikers in Bezug auf organische Chemie beantworten durfte. Vielen Dank auch für die kurzfristige Nachsynthese von **D3A**, um damit meine Experimente abschließen zu können.

Ich danke auch Torsten Sachse für die Bereitstellung der Theorieergebnisse. Vielen danke auch für die zahlreichen Diskussionen über Ergebnisse, Möglichkeiten und Einschränkungen der theoretischen Chemie.

Ein riesen Dank noch an Maximilian Hupfer, durch dessen zahllose Experimente es möglich war, alle Messaufbauten und die entsprechende Steuerungssoftware bis heute zu optimieren und diverse Fehler und Fehlerchen auszumerzen.

Karin Kobow danke ich für die die Unterstützung im Laboraltag und die Herstellung eines Teils der Proben und Lösungen, die für diese Arbeit verwendet wurden.

Ich danke allen aus der AG Dietzek, die mir beim Einarbeiten in die fs-TA Spektroskopie geholfen haben und mich stets unterstützt haben, wenn das einjustieren der Delaylines mal wieder etwas länger gedauert hat.

Zuletzt möchte ich meinen Kindern Liam und Iain und meiner Frau Madlen danken die mich auf dem Weg zur Promotion stets unterstützt und motiviert haben. Auch meinen Eltern danke ich die mich immer unterstützt haben.

List of Publications

Refereed publications in scientific journals

1. Felix Herrmann-Westendorf, Torsten Sachse, Martin Schulz, Martin Kaufmann, Vladimir Sivakov, Rainer Beckert, Todd J. Martínez, Benjamin Dietzek, Martin Presselt: *Photo-Annealing of Merocyanine Aggregates*. The Journal of Physical Chemistry A 11/2018, DOI:10.1021/acs.jpca.8b09048
2. M. Kaufmann, M.L. Hupfer, T. Sachse, F. Herrmann-Westendorf, D. Weiß, B. Dietzek, R. Beckert, M. Presselt: *Introducing Double Polar Heads to Highly Fluorescent Thiazoles: Influence on Supramolecular Structures and Photonic Properties*. Journal of Colloid and Interface Science 04/2018; 526, DOI:10.1016/j.jcis.2018.04.105
3. Maximilian Lutz Hupfer, Martin Kaufmann, Felix Herrmann-Westendorf, Torsten Sachse, Ludovic Roussille, Karl-Heinz Feller, Dieter Weiss, Volker Deckert, Rainer Beckert, Benjamin Dietzek, Martin Presselt: *On the Control of Chromophore Orientation, Supramolecular Structure and Thermodynamic Stability of an Amphiphilic Pyridyl-Thiazol upon Lateral Compression and Spacer Length Variation*. ACS Applied Materials & Interfaces 11/2017; DOI:10.1021/acsami.7b13042
4. Julia Preiß, Felix Herrmann-Westendorf, Thien H. Ngo, Todd J. Martínez, Benjamin Dietzek, Jonathan P Hill, Katsuhiko Ariga, Mikalai M. Kruk, Wouter Maes, Martin Presselt: *Absorption and Fluorescence Features of an Amphiphilic meso -Pyrimidinylcorrole: Experimental Study and Quantum Chemical Calculations.* The Journal of Physical Chemistry A 10/2017; DOI:10.1021/acs.jpca.7b08910
5. Ruri Agung Wahyuono, Felix Herrmann-Westendorf, Andrea Dellith, Christa Schmidt, Jan Dellith, Jonathan Plentz, Martin Schulz, Martin Presselt, Martin Seyring, Markus Rettenmeyer, Benjamin Dietzek: *Effect of Annealing on the Sub-Bandgap, Defects and Trapping States of ZnO Nanostructures*. DOI:10.1016/j.chemphys.2016.12.002
6. Saunak Das, Felix Herrmann-Westendorf, Felix H Schacher, Eric Täuscher, Uwe Ritter, Benjamin Dietzek, Martin Presselt: *Controlling Electronic Transitions in Fullerene van der Waals Aggregates via Supramolecular Assembly*. ACS Applied Materials & Interfaces 08/2016; 8(33), DOI:10.1021/acsami.6b06800
7. Stefanie Heike Habenicht, Stefan Schramm, Stefan Fischer, Torsten Sachse, Felix Herrmann, Andrea Bellmann, Benjamin Dietzek, Martin Presselt, Dieter Weiss, Rainer Beckert, Helmar Görls: *Tuning the Polarity and Surface Activity of Hydroxythiazoles – Extending Applicability of Highly Fluorescent Self-Assembling Chromophores to Supramolecular Photonic Structures*. Journal of Materials Chemistry C 02/2016; 4(5):958-971, DOI:10.1039/C5TC03632A
8. Martin Schulz, Fabian Dröge, Felix Herrmann, Julian Schindler, Helmar Görls, Martin Presselt: *Neutral, heteroleptic copper(I)-4H-imidazolate complexes: Synthesis and characterization of their structural, spectral and redox properties*. Dalton Transactions 02/2016; 45(11), DOI:10.1039/C5DT04435A
9. Stefan Fischer, Jenya Vestfrid, Atif Mahammed, Felix Herrmann-Westendorf, Martin Schulz, Jürgen Müller, Olaf Kiesewetter, Benjamin Dietzek, Zeev Gross, Martin Presselt: *Photometric Detection of Nitric Oxide Using a Dissolved Iron(III) Corrole as a Sensitizer*. ChemPlusChem 02/2016; 81(7), DOI:10.1002/cplu.201500553
10. Alejandro De la Cadena, Torbjörn Pascher, Dar'ya Davydova, Denis Akimov, Felix Herrmann, Martin Presselt, Maria Wächtler, Benjamin Dietzek: *Intermolecular exciton-exciton annihilation in phospholipid vesicles doped with [Ru(bpy)2dppz]2+*. Chemical Physics Letters 12/2015; 644, DOI:10.1016/j.cplett.2015.11.024
11. Felix Herrmann, Burhan Muhsin, Chetan Raj Singh, Sviatoslav Shokhovets, Gerhard Gobsch, Harald Hoppe, Martin Presselt: *Influence of Interface-Doping on Charge Carrier Mobilities and Sub-Bandgap Absorption in Organic Solar Cells*. The Journal of Physical Chemistry C 04/2015; 119(17), DOI:10.1021/acs.jpcc.5b00124
12. Olesia Synooka, Kai-Rudi Eberhardt, Chetan Raj Singh, Felix Herrmann, Gernot Ecke, Bernhard Ecker, Elizabeth von Hauff, Gerhard Gobsch, Harald Hoppe: *Influence of thermal annealing on PCDTBT:PCBM composition profiles*. Advanced Energy Materials 04/2014; 4(5), DOI:10.1002/aenm.201300981

13. Wichard J D Beenken, Felix Herrmann, Martin Presselt, Harald Hoppe, Sviatoslav Shokhovets, Gerhard Gobsch, Erich Runge: *Sub-bandgap absorption in organic solar cells: Experiment and theory*. Physical Chemistry Chemical Physics 08/2013; 15(39)., DOI:10.1039/c3cp42236d
14. Martin Presselt, Felix Herrmann, Harald Hoppe, Sviatoslav Shokhovets, Erich Runge, Gerhard Gobsch: *Influence of Phonon Scattering on Exciton and Charge Diffusion in Polymer-Fullerene Solar Cells*. Advanced Energy Materials 08/2012; 2(8)., DOI:10.1002/aenm.201100793
15. Martin Presselt, Felix Herrmann, Sviatoslav Shokhovets, Harald Hoppe, Erich Runge, Gerhard Gobsch: *Sub-bandgap absorption in polymer-fullerene solar cells studied by temperature-dependent external quantum efficiency and absorption spectroscopy*. Chemical Physics Letters 07/2012; 542:70–73, DOI:10.1016/j.cplett.2012.05.063
16. Felix Herrmann, Sebastian Engmann, Martin Presselt, Harald Hoppe, Sviatoslav Shokhovets, Gerhard Gobsch: *Correlation between near infrared-visible absorption, intrinsic local and global sheet resistance of poly(3,4-ethylenedioxy-thiophene) poly(styrene sulfonate) thin films*. Applied Physics Letters 04/2012; 5(4), DOI:10.1063/1.3697402

Declaration of Originality

Selbstständigkeitserklärung

Ich erkläre, dass ich die vorliegende Arbeit selbstständig und unter Verwendung der angegebenen Hilfsmittel, persönlichen Mitteilungen und Quellen angefertigt habe.

Jena, den

Felix Herrmann-Westendorf